UNIVERSITÀ DEGLI STUDI DI PADOVA

Dipartimento di Ingegneria Industriale

Corso di laurea Magistrale in Ingegneria Dell'Energia

Tesi di laurea Magistrale

A numerical approach to predict the rotating stall inception of an axial low-speed compressor

Relatore

Prof. Giorgio Pavesi

Laureando: Matteo Inglese

Matricola: 1130360

Correlatore esterno

Prof. Antoine Dazin

Anno Accademico 2017/2018

SUMMARY

FIGURE INDEX

1. INTRODUCTION

1.1 GENERAL INTRODUCTION

Turbomachines are devices in which the energy is transferred to/by a continuously flowing fluid by the interaction with one or more blade rows. The rotating blade row (rotor or impeller) changes the overall energy of the fluid moving through it, doing positive or negative work, depending on the machine type. There are two main categories of turbomachines: those which increment the fluid energy absorbing power from an external source such as fans, compressors and pumps; others that subtract energy from a fluid, generating power, such as steam and gas turbines. According to the service required, there is one type of pump/compressor or turbine best suited to provide optimum operational condition depending on the *specific speed number*; this number defines the shape of the machine. Machines in which the flow path through the passage of the rotor is totally or mainly parallel to the axis of rotation, are termed *axial flow machines.* When the passage of the flow is totally or mainly perpendicular to the rotation axis, the machine is termed *radial flow machine.* When both radial and axial velocity component are present they are called *mixed flow turbomachines.*

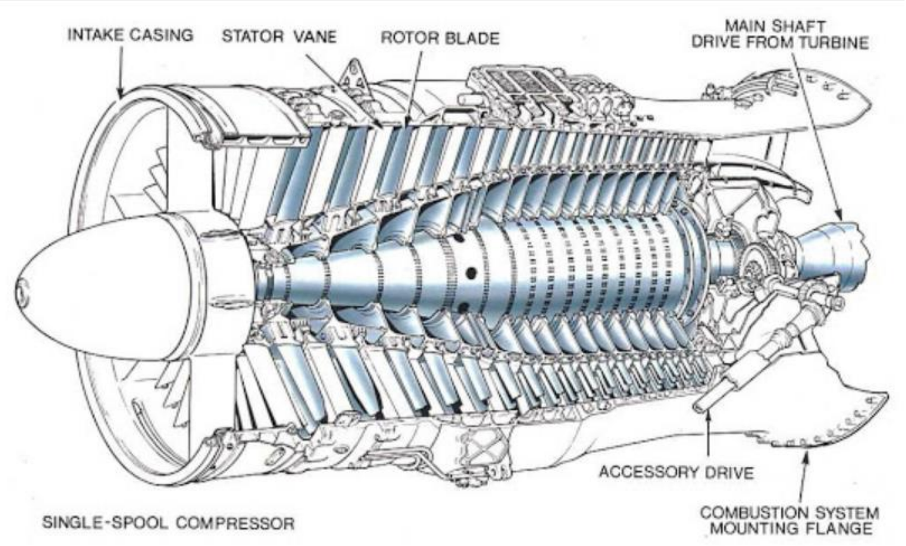

Figure 1-1 A multistage axial compressor

The focus of this work is, as better explained in later chapters, an investigation of some characteristic parameters that, carefully monitored, might be representative and helpful in forecasting the inception of the unsteady phenomenon of the rotating stall in axial compressors. Rotating stall is explained in more detail in section 2.2.9. For this purpose, no brand-new data were collected specifically to pursue the analysis but we make use of the ones collected by Veglio (Veglio M., 2015) in her Ph.D. work.

Axial compressors produce a continuous flow of pressurized gas with high efficiency and large mass flow rate. The pressure rise for each stage must be low in order to attain high efficiency, hence for obtaining high pressure rise, several stages have to be arranged in series. Axial compressors are widely used in large gas turbines such as jet engines (Figure 1.1), ship engines, and small scale power stations. They are also used in industrial applications such as large volume air separation plants, blast furnace air, chemical plants but also in aerospace.

Thus, the research in this field has been very prolific in the last 60 years, due to the large number of important applications, aiming at a deeper comprehension of the physical phenomena occurring in the interaction fluid/rotating machine in order to reach higher efficiency and more reliable design.

1.2 INTRODUCTION TO TURBOMACHINES HANDLING A COMPRESSIBLE FLUID

The main focus of this paragraph is to give a quick overview of the topic in order to have a reference framework. For a more exhaustive dissertation (Dixon l., 2010) is recommended.

The performance parameters Δh_{0s}, η and P for a turbomachine handling a compressible flow, are expressed functionally as:

$$\Delta h_{0s}, \eta, P = f(\mu, N, D, \dot{m}, \rho_{01}, a_{01}, \gamma)$$

Where:

a_{01} is the stagnation speed of the sound at the entry of the machine,

ρ_{01} is the fluid density at the entry of the machine,

Υ is the ratio of specific heats C_p/C_v,

$\dot{m}$ is the mass flow rate,

D is the impeller diameter,

N is the speed of rotation,

μ is the fluid dynamic viscosity,

P is the power supplied by the electric motor

H is the compressor efficiency,

Δh_{0s} is the stagnation enthalpy (sum of the specific enthalpy *h* and the kinetic energy $\frac{1}{2}c^2$).

By the procedure of the dimensional analysis using the four primary dimensions (mass, length, time and temperature), selecting the ρ_{01}, N, D, as a common factor and considering a machine handling a perfect gas, each of these three relationships may be reduced to five dimensionless groups:

$$\frac{p_{02}}{p_{01}}, \eta, \frac{\Delta T_0}{T_{01}} = f\left\{\frac{\dot{m}\sqrt{(RT_{01})}}{D^2 p_{01}}, \frac{ND}{\sqrt{(RT_{01})}}, Re, \gamma\right\}$$

Where:

1. $\frac{ND}{\sqrt{(RT_{01})}}$ is proportional to the *Mach number*, $\mathrm{M} = \frac{C}{a} = \frac{c}{\sqrt{\gamma RT}}$,
2. $\frac{\dot{m}\sqrt{(RT_{01})}}{D^2 p_{01}}$ is proportional to the *flow coefficient*, $\Phi = \frac{c_m}{U}$,
3. $\frac{\Delta T_0}{T_{01}}$ is equal to the *power coefficient* $\hat{P}$ for an adiabatic transformation,
4. $\frac{p_{02}}{p_{01}}$ is proportional to the *energy transfer coefficient (stage loading)*, $\Psi = \frac{\Delta h_0}{U^2}$

Where, *U* is the mean blade speed, c_m is the average meridional velocity.

For a machine of a specific size and handling a single gas it has become customary to delete *γ*, *R*, and *D* from the above equation and similar expressions. If, in addition, the machine operates at high Reynolds numbers *Re* can also be dropped. Under these conditions the performance parameters become:

$$\frac{p_{02}}{p_{01}}, \eta, \frac{\Delta T_0}{T_{01}} = f\left\{\frac{\dot{m}\sqrt{(T_{01})}}{p_{01}}, \frac{N}{\sqrt{(T_{01})}}\right\}$$

Noting that omitting *D* and *R* the independent variables are no longer dimensionless. It is also important to note that he vertical axis is proportional to Ψ and the horizontal one is proportional to Φ. Hence, a typical performance map for a compressor is obtained as shown in Figure 1.2.

The performance map is a graphical representation of the operating relation among the machine parameters. The pressure ratio across the whole machine is plotted as a function of $\dot{m}\sqrt{T_{01}}/p_{01}$ for several fixed values of $N/\sqrt{T_{01}}$ and contours of compressor efficiencies.

Each of the constant speed curves of the compressors terminate at the surge/stall line where, beyond this point, operation is unstable. It can be seen that, at high speed and low-pressure ratios, the constant speed curves become vertical since the Mach number across the minimum section has reached unity and the flow is said to be *chocked*.

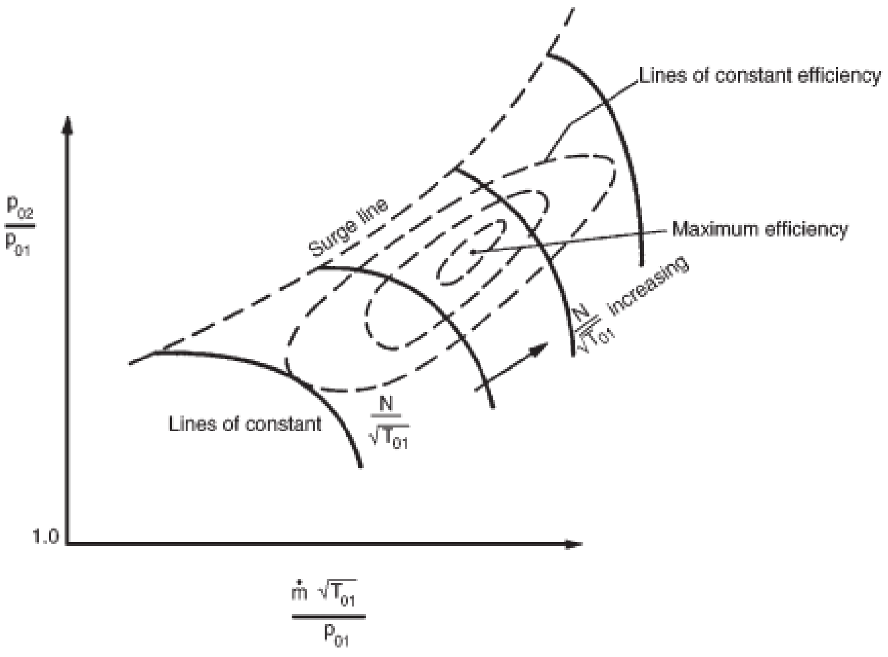

Figure 1-2 Performance characteristic of a compressor

Figure 1.3 illustrates a section of an multistage axial compressor. A compressor stage is defined as rotor blade row followed by a stator blade row. Rotor blades, in black, are fixed to the rotor drum and the stator blades are fixed to the outer casing

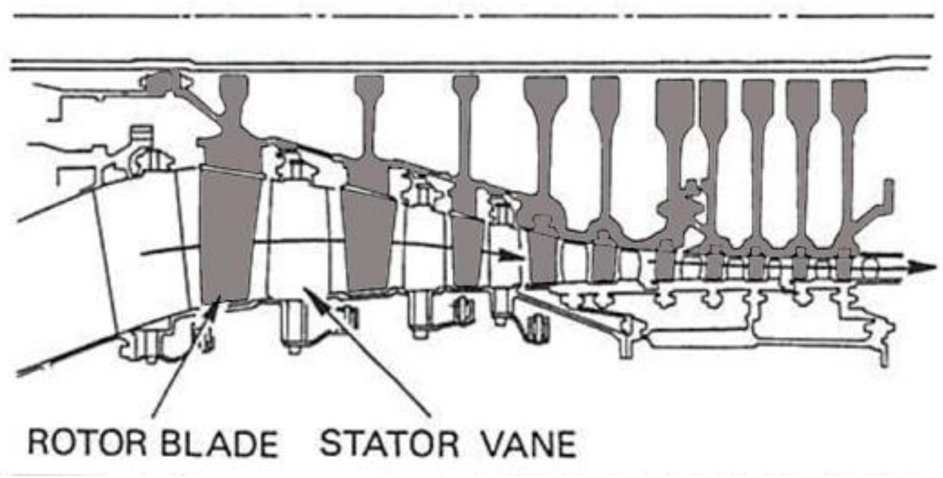

Figure 1-3 Section of a compression system

The velocity diagrams for a stage are given in Figure 1.4. A *normal* compressor stage is one where the absolute velocities and flow directions at stage outlet are the same as at stage inlet. The flow from a previous stage with absolute velocity c_1 and direction α_1 approaches the rotor blade at speed *U*. Subtracting the latter to the former, we obtain the relative velocity w_1 and angle β_1. The exiting flow from the rotor blade, after acquiring the energy given through the shaft, has a new velocity w_2 and direction β_2 and approaches the stator blade with absolute velocity c_2 and angle α_2. The stator blade converts the fluid kinetic energy in static pressure decreasing the velocity c_2 to $c_3 = c_1$ and an angle $\alpha_3 = \alpha_1$

.

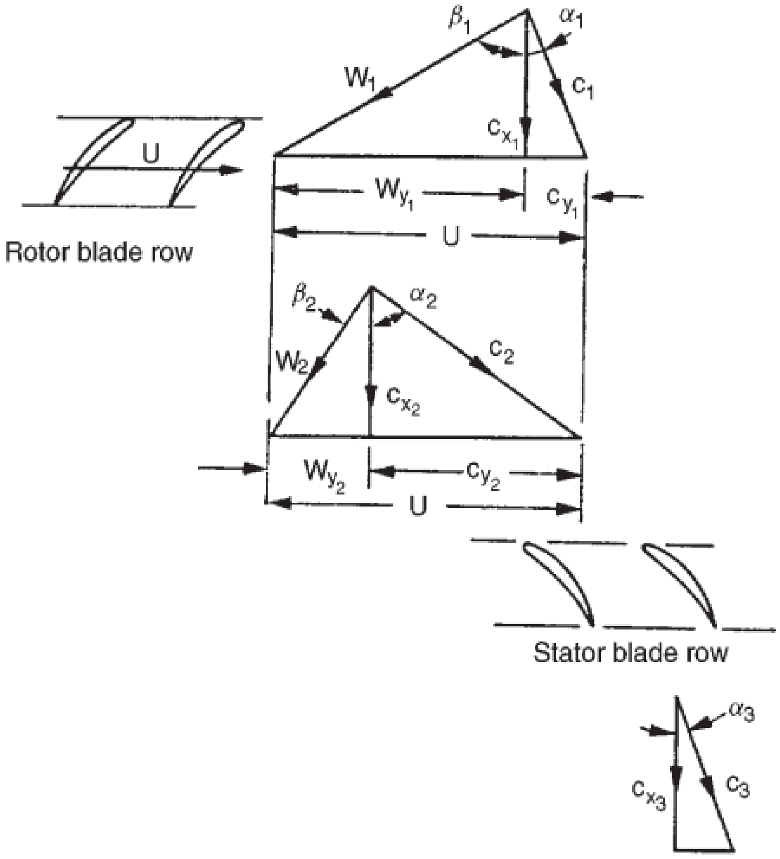

Figure 1-4 Velocity diagram for a compressor stage

Finally Figure 1.5 provides a sketch of the thermodynamic states of each transformation happening in the compressor. The specific work done by the rotor on the fluid, assuming an adiabatic transformation, is:

$\Delta W = h_{02} - h_{01} = U(c_{\theta 2} - c_{\theta 1})$

By the rotalpy conservation, in the rotor reference system we know that $h_{0,rel} = h + 0.5\, w^2$, so in a rotor blade passage:

$$h_1 + 0.5\, w_1^2 = h_2 + 0.5\, w_2^2,$$

while, ignoring the inevitable losses, h_0 remain constant across the stator:

$$h_2 + 0.5\, w_2^2 = h_3 + 0.5\, w_3^2$$

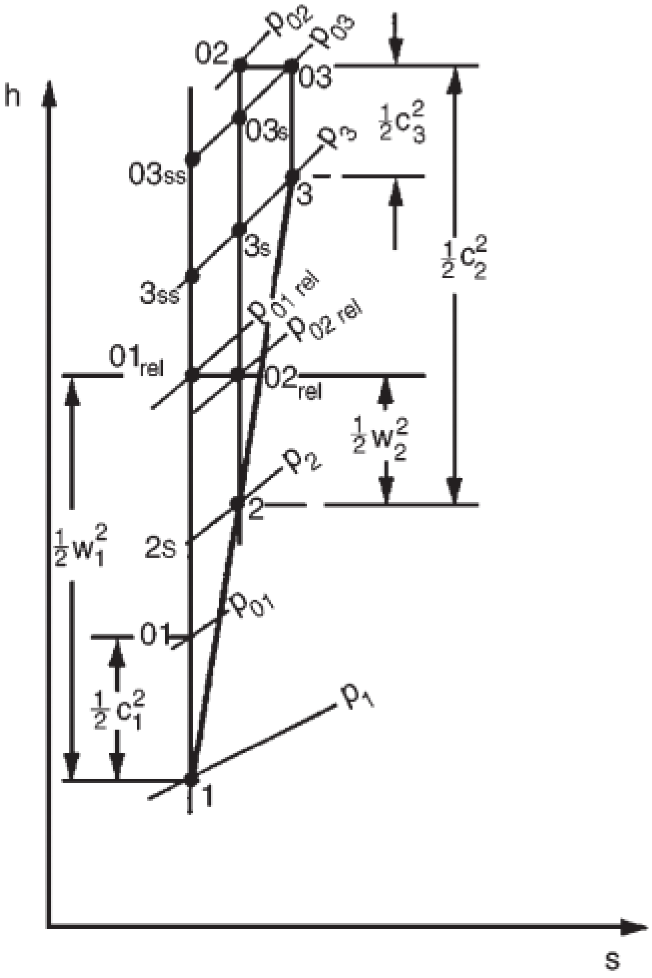

Figure 1-5 Mollier diagram for an axial compressor stage

2. THE MAIN UNSTEADY MECHANISMS

2.1. INTRODUCTION

Nowadays the research is focused on the unsteady flow phenomena for a scientific and economic purpose. The problem, in the turbomachinery field, is dealing with the arise of a series of simultaneous unsteady events that make this subject difficult to treat with a global approach but instead promote the development of a plethora of different kind of research paths. The main goal of this chapter is to give a general overview about the predominant unsteady mechanisms resulting from the interaction among a series of fixed and rotating blades, which are the time and spatial scales of them, what is resulting flow field in spool row and which is the role of those unsteady mechanisms in the energy exchange between fluid and machine.

Before proceeding, a remainder about some definitions is given. The concept of *stationarity* (steadiness) is referred to the variability, during the time, of certain state conditions, the concept of *stability* to their appearance regularity. A phenomenon is considered stationary (steady) when the state variables remain constant during the time, vice versa it's unsteady. If those variations feature a recurring and regular behaviour the phenomenon is called *stable*. Furthermore, if a machine experiences a transitory perturbation but it's able to recover the working equilibrium, it's said to work in stable condition. It seems important to highlight that compressors are generally exposed to stability loss and, despite its name, the surge line delimits the working stable area from that one where all kind of instabilities usually arise.

2.2. GENERAL CONTEXT

The turbomachinery flow is greatly unsteady. Viscosity, turbulence and unsteady mechanisms play an essential role in the energy exchange. The equation of the conservation of total enthalpy h_0:

$$\frac{dh_0}{dt} = \frac{1}{\rho}\frac{\delta P}{\delta t} + div\left[\tau\vec{V} - \vec{q}\right]$$

Considering the adiabatic case (q=0) e the absence of friction (τ=0), only the term $\delta P/\delta t$ provide a source of enthalpy.

Figure 2.1 is a classification of the main unsteady phenomena and their origins proposed by Callot (Callot, 2002). This study is going to focus on the rotating stall, a periodic phenomenon not related to revolution speed.

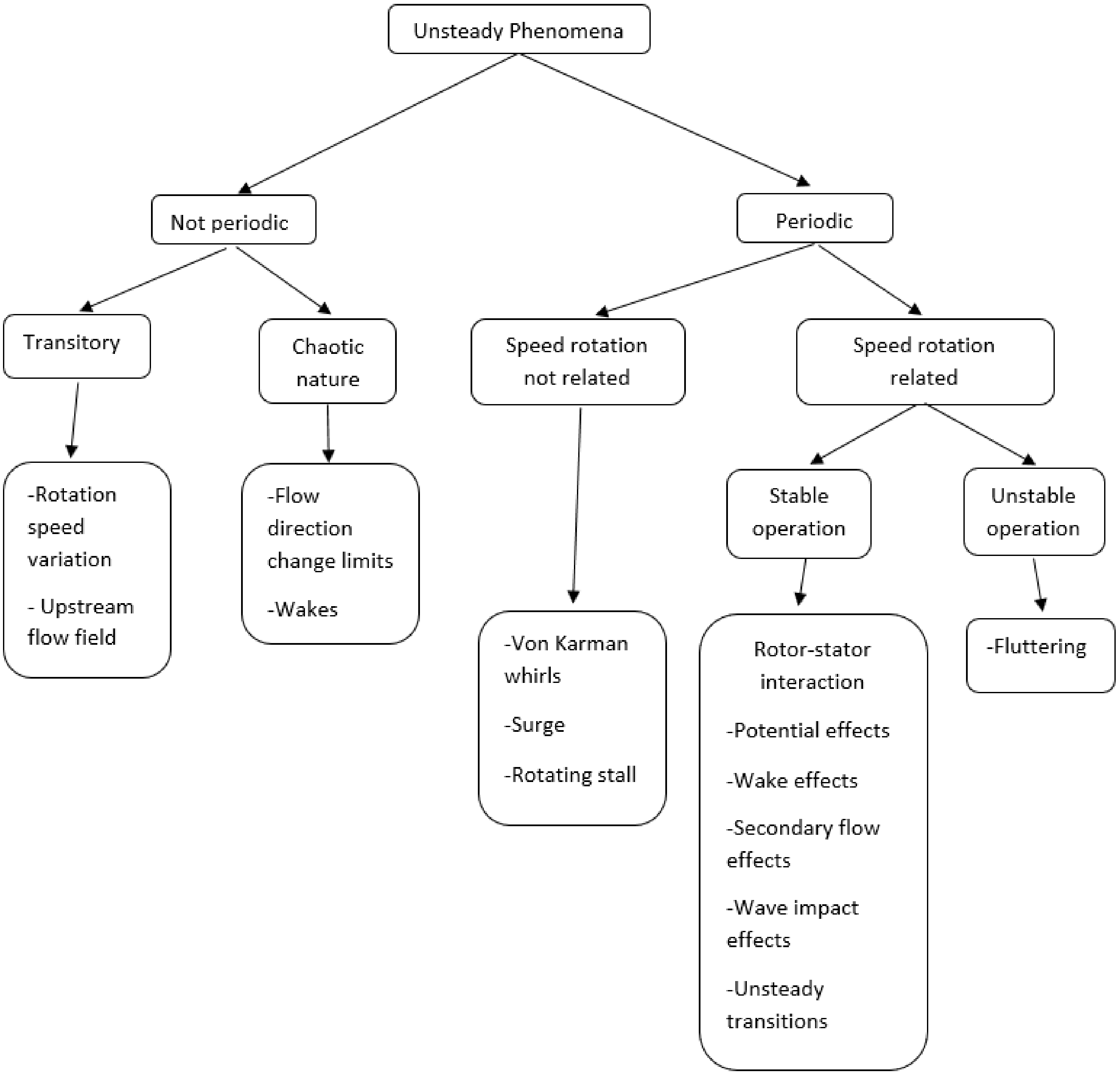

Figure 2-1 Main unsteady phenomena in turbomachinery flow

A quick characterization about the unsteadiness degree of a certain flow can be done using the reduced frequency $\overline{\omega}$. It is a non-dimensional parameter, used in the aerodynamic field, for vibratory events. it's the product between the phenomenon frequency for the characteristic length divided by the flow velocity (velocity carrying the information) or the ration between the convection time t_c and the time linked to the perturbation t_i.

$$\overline{\omega} = \frac{t_c}{t_i}\frac{\omega\, x}{c}$$

As long as $\overline{\omega} \ll 1$, the phenomenon can be considered quasi-steady.

2.2.1. POTENTIAL EFFECTS

The potential effects are generated by the blades movement and they are the equivalent of a pressure force destabilizing the flow stream lines and inducing a quasi-instantaneous variation of the pressure field in the blades surrounding. This periodic impulse propagates both towards upstream and downstream like an acoustic wave.

The results of several research on turbines and compressors, highlight the influence of two geometric parameters: the spools distance and the rotor blades number. (Dring R.P. [et al.], 1982), (Giles M.B., 1988), (Korakianitis T., 1992). The potentials effects can be neglected instead of the wake effect as far as the distance between spools is above the threshold value of 30% of the rotor blade chordand it increases proportionally to the numbers of blades (Oliveira G. L., 1999). Under these circumstances it has been observed that this effect is an order of magnitude lower than the wake interaction.

The intensity of these effects can be estimated through this equation provided by Greitzer (Greitzer E.M., 1985):

$$\left.\frac{\delta}{\rho V^2}\right|_{max} = \frac{\sqrt{1-M^2}}{\sqrt{1-M_x^2}}\, exp\left(-2\pi\,\frac{\sqrt{1-\ M^2}}{\sqrt{1-M_x^2}}\frac{x}{\Delta\theta}\right)$$

where $\Delta\theta = 2\pi/N$ rapresents the blade pitch, M and M_x are respectively the absolute and axial local Mach number and x is the potential source axial distance. For a subsonic flow this effect is negligible if $x/\Delta\theta > 30\%$. Nevertheless, the potential effects are transmitted without softening for a transonic stream ($M \approx 1$) and could affect the flow far away the wave sources. The previous equation shows how the potential effects is stronger in those regions where the speed is higher i.e. over the upper blade surface near the leading edge, for what concerns compressors, and over the upper blade surface near the trailing edge for turbines. However, the potential effects wavesheading upstream, going against the flow direction, play an important role defining the flow angle of attack as shown in figure 2.2.

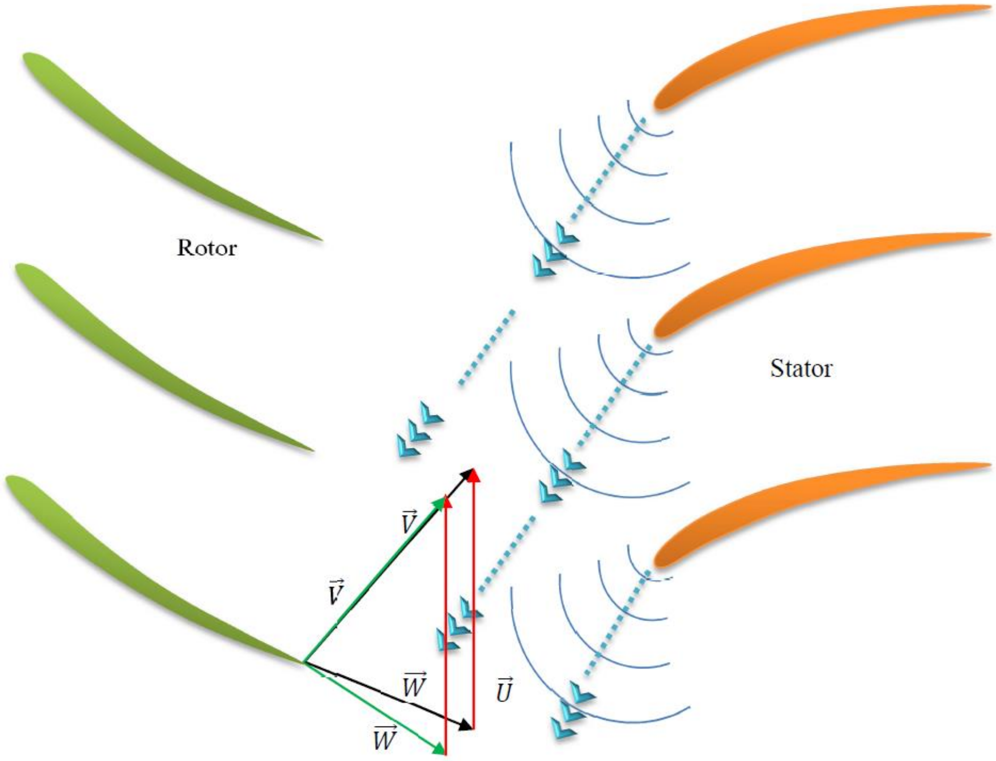

Figure 2-1 Potential effects influence over the flow directions between two successive blades

2.2.2. WAKE EFFECT

It’s called wake effect the resulting action of the main flow driving force practiced on the boundary layer. It is generated nearby the blade walls and then merged at the trailing edge. Unlike the potential effects, wakes generate from the trailing edge only invest downstream region. The wakes shed by rotor 1 are cut and distorted by stator 2. They are formed into wake segments which pass through the stator 2 blade passages and appear at exit between the stator 2 wakes.

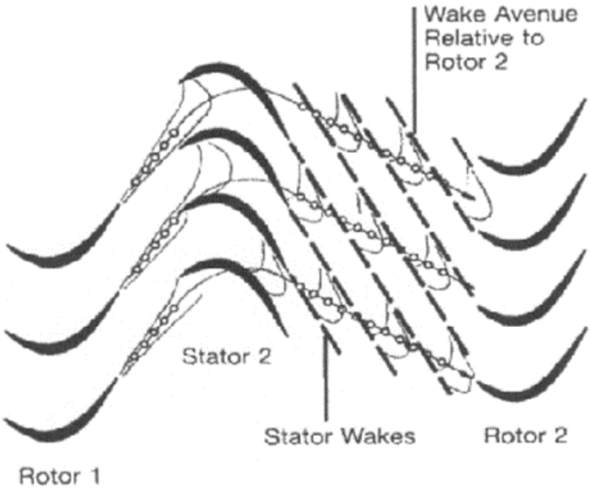

Figure 2-3 Schematic of wake avenues in a multistage LP turbine (Binder, A, Schröder, T, and Hourmouziadis, J, 1989)

The thick broken lines indicate the stator 2 wakes and therefore the direction of the flow in the absolute frame. Regardless of the frame of reference, the wake segments are arranged into “avenues”. It should be noted that the avenue contains discrete wake segments rather than a continuous wake. Because the rotor 1 and rotor 2 blade counts are different, the rotor 1 wake avenues will enter the rotor 2 blade passages at different circumferential locations. Under these circumstances, rotor-rotor interactions can sometimes manifest themselves in unsteady data at a frequency that represents the sum and difference frequencies (i.e. beating) of the two rotor passing frequencies.

Figure (2.4) illustrates the interactions in a 3 stages axial turbine. The step between blades is the same for every spool and the mechanism of partition and transportation is clearly showed. Finally, the interaction among wakes has to be taken in to account in addition to their axial transportation mechanism.

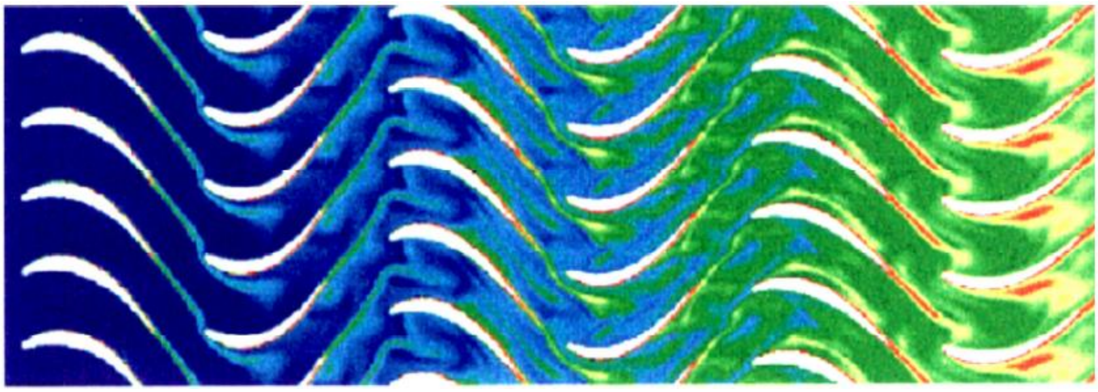

Figure 2-4 Simulation of wake transport in a low-pressure turbine (Arnone, 1999)

Sentker (Sentker A. et Riess W., 2000)proposed an experimental study of a turbulent flow field in a 2 stages axial compressor in subsonic condition where he shows the presence of low speed zones in intra-blades clearances but he wasn't able to identify the contribution of the potential effects and wakes separately. Figure (2.5)

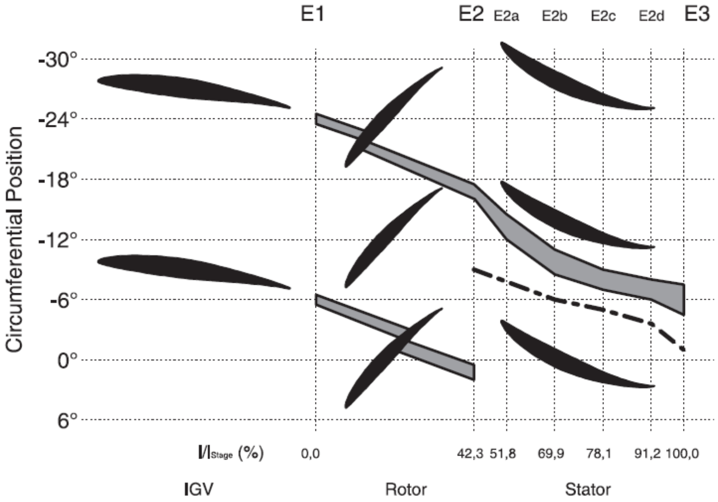

Figure 2-5 IGV wake in first stage (Sentker A. et Riess W., 2000)

The speed deficit characterizing wakes is modelled with a jet, called negative jet, having the same direction of the velocity gradient vector. As shown in figure (2.6), the wake region is seen as moved with a shifting speed $\vec{v}_g$ of the same order of magnitude of the maximum velocity. In a turbine it's important to notice that the speed triangles deformation exiting the rotor contributes to increase the work transferred to the machine thanks to a bigger deceleration of the relative flow so the dissipative nature of the phenomenon is partially counterbalanced by this effect.

The evolution of the wake from its origin to its disappearance is quite complex: it is partially dissipated, it is intermittent and it interacts with blades or other wake portions encountered during the path. The spatial irregularity of velocity field provokes the deformation of the wake shape: it becomes extended in the acceleration zone and contracted in the deceleration one.

The interaction between the wake vorticity and the blade rotation generates the formation of two vortexes that limit the wake expansion zones. Inside wakes, the two vortexes contribute to the mass transport in the same direction as the main flow does, while, according to the mass conservation, it's the opposite outside them. This phenomenon is called *wake jet* and it is responsible for the generation of aspiration points and the wake impact on the blade walls. These points spread out along blade walls following the flow course inside the channels between blades.

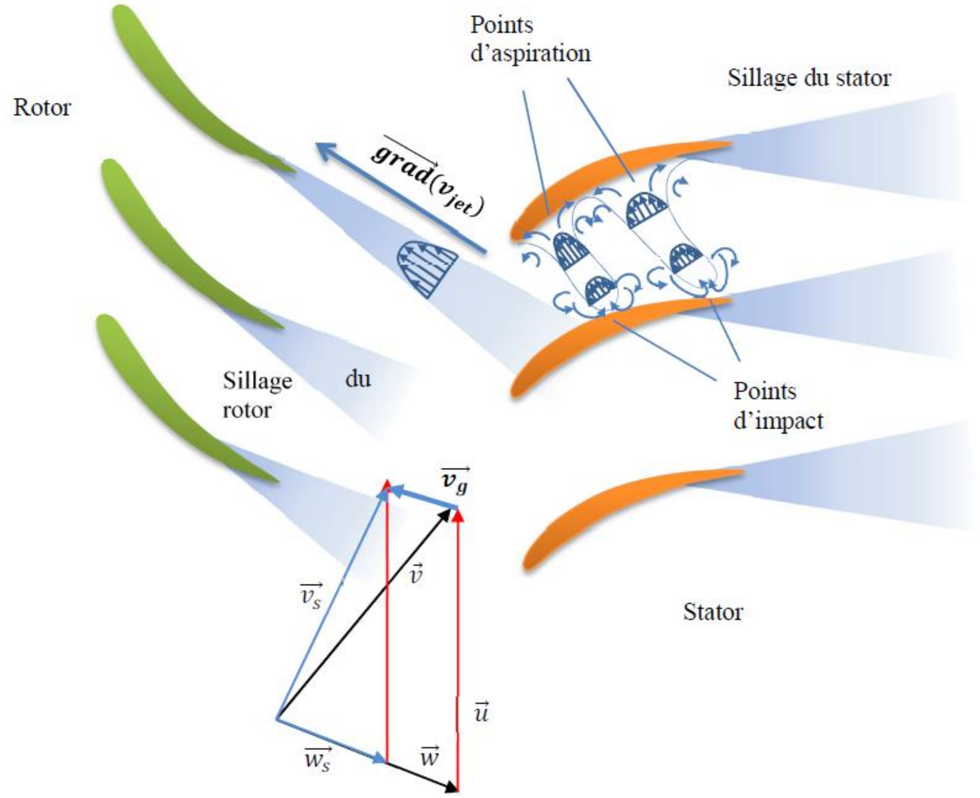

Figure 2-6- Speed triangle modification inside the wake zone

Another aspect that can't be neglected is the interaction with boundary layers whose development is affected in two different ways. The external part of the boundary layer is affected by the temporal oscillation of the physics parameters caused by the unsteadiness of the flow while the internal layer is unsettled by wake parts. It seems that the second mechanism is dominant in turbomachines. The contribution provided by wakes makes the boundary layer unstable and could be the cause for the laminar-turbulent transition. The boundary layer is characterized by this temporal alternation except for fully developed turbulent flow in which its contribution is less important.

2.2.3. SHOCK WAVES

A shock wave is a finite discontinuity in a compressible flow that can be either stationary or moving or moving relatively to the observer's reference point. Its formation is due to the accumulation of a series of small disturbances, weak waves, that can be about compression and expansion. Shock-wave can be normal, oblique or curved with respect to the flow direction. Two different examples will be given to better figure out the phenomenon.

In a first case (Figure 2.7a), a piston has a sudden motion to the right with a finite velocity V which can be approximated as a series of smaller steps ΔV. These small steps of increase velocity will create a series of compression weak waves propagating to the right. The first wave will travel at a speed a_1 related to the temperature T_1 of gas undisturbed but the second wave behind will travel at a speed a_2 greater than a_1 since the gas ahead the second wave has been compressed by the first wave. The same process will happen to the following waves. Once the waves behind will catch the wave ahead they combine in to a stronger wave called shock wave.

In a second case (Figure 2.7b), a gas in a duct is initially stationary and the back pressure p_b start to decrease. It will create a series of expansion waves propagating upstream and causing the gas low velocity to increase. After the flow velocity at the smallest section reaches Mach 1, the expansion waves due to further decrease of the back pressure cannot propagate upstream beyond the throat because the flow will carry the waves back downstream. The flow downstream the throat becomes supersonic and the expansion waves can propagate upstream only in the subsonic flow region, not the supersonic one. This cause the expansion wave to be accumulated between these two regions to form a shock wave.

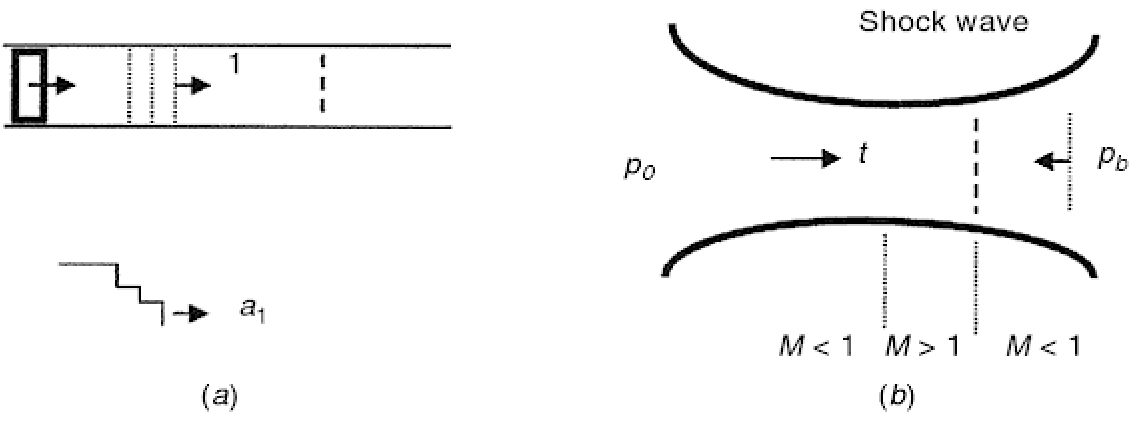

Figure 2-7 Formation of a normal shock wave (Peng, 2007)

Several studies show that a shock wave, oscillating in time, originated from a perturbation, produces heat and entropy. If the propagation direction of this perturbation is different compared to the shock wave one then the latter is out of synchronism in space and generates vorticity. The shock waves system developed in a stage gap of a turbine/compressor is generally very complex in terms of structure and geometry. They exit from the blade trailing edge and interact with the next blade upper surface. Under the spool rotation effect, they spread throughout the blade row generating reflected waves that move back the flow stream interacting with the upstream blade row and generating other reflections. This mechanism is reduced quickly and after two or three reflections is generally soften.

An important mechanism of this kind of interaction is the retrograde sweeping (BALAYAGE) due to the interaction between the shock waves and the boundary layer (Figure 2.8). The boundary layer is periodically detached from the blade wall causing vorticity and local variation of the heat flow.

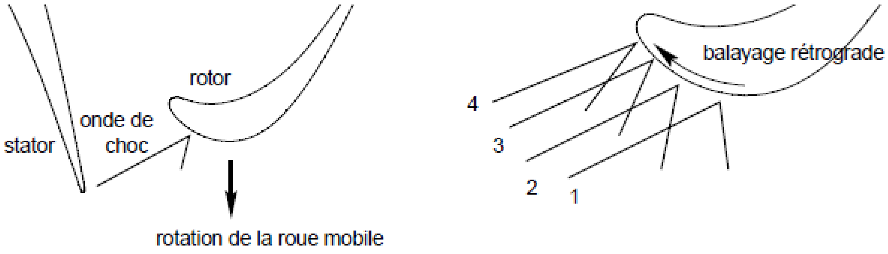

Figure 2-8 Retrograde sweeping due to shock waves interaction

2.2.4. CALMING EFFECT

The *calming* principle is based on the study of the boundary layer condition near wall. A boundary layer development along a certain shape begins with a laminar regime, starting from the point where the speed is null, and evolves into a turbulent regime passing through a transition. There are several possible transitions. The *natural transition* corresponds to the natural wave development of Tollmien-Schlichting and, as the Reynold number increases, there is also an increase of instabilities in the boundary layer. The *by-pass* transition happens when the flow outside the boundary layer has a high turbulence level and transmits his chaotic nature to the internal layer. The *transition for separation* happens when the boundary layer is detached under the effect of too much high opposing gradient of pression or caused by an external perturbation. The flow can either reattach itself or remain detached generating high losses.

The flow disruption in a turbomachine can produce a periodic regime transition. Turbulent spots inside the boundary layer arise around the blade receiving the instable flow and make the transition start. In first analysis the turbulent spots trigger under the flow influence adjacent the blade wall but they rapidly spread through the whole boundary layer thickness. The turbulent spots are followed by "relaxed" zones representing the area between turbulent and laminar regions. These zones can be classified by their speed scale: $0.3U_{flow}$ for the laminar areas, $0.5U_{flow}$ for the calmed ones and $0.9U_{flow}$ for turbulent spots. In order to clearly represent this mechanism of different speeds it can be sketched in a space-time diagram: a horizontal line is an infinite speed whilst a vertical one is null speed i.e. a stationary phenomenon (figure 2.9).

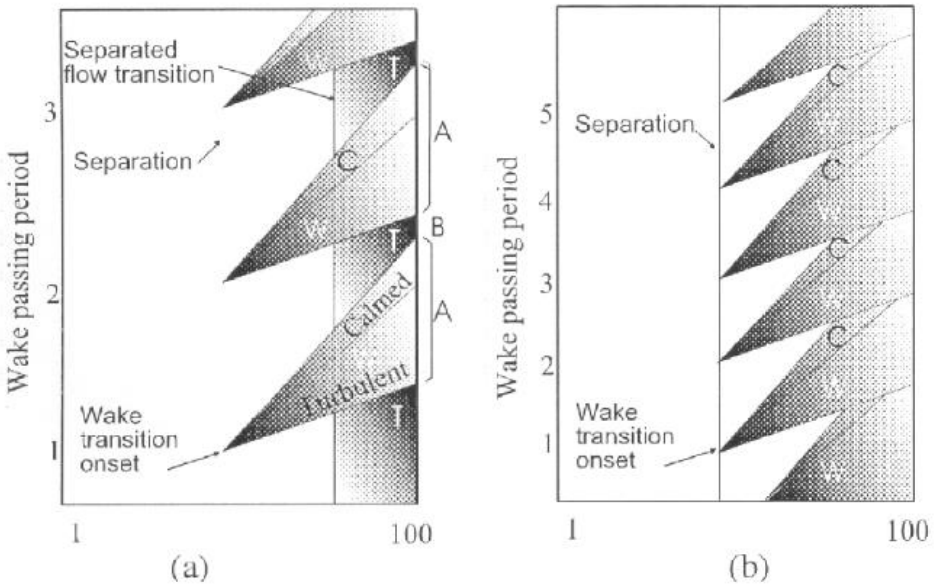

Figure 2-9 Space-Time diagram of the "calming" effect (Hodson P. et al., 2000)

In figure 2.9a it can be seen that, if the flow perturbation has a low frequency, the calmed zoned will absorb enough energy from turbulent spots and the laminar area detachment will always appear but it is delayed. If the frequency increases (figure 2.9b), the calming effect is always present until a second wake passage and the laminar layer will be replaced by a boundary layer more resistant against high pressure gradients.

2.2.5. CLOCKING AND AXIAL GAP EFFECT

As seen in a previous paragraph, the flow fields in turbomachines is unsteady and this is mainly due to the relative motion between rotor and stator airfoils. This relative motion leads to viscous and inviscid (potential) interactions between the blade rows. Small axial-gap definitely enhances this kind of interaction. Wake interaction is the main contribution of the unsteady vortical effect during blades interaction: the vortical and entropic wakes shed by one or more upstream rows interact with the downstream airfoils and other wakes. The distribution of the potential flows and wakes in the flow passage depend on the relative positions of blade rows in axial and circumferential direction, so variations in the relative axial positions (axial gap) and circumferential positions (clocking effect) of stators or rotors can change these distributions, leading to different compressor efficiency.

Investigations (Eulitz F., 1996), (Hongyan Huang, 2004) on airfoils clocking (indexing) have been performed and results show that, generally speaking, the average-time stage efficiency is a function of the airfoil clocking positions. The highest efficiency occurred when the upstream rotor/stator wake impinged on the leading edge of the downstream rotor/stator. The lowest efficiency corresponding to the upstream rotor/stator wake convected through the middle of the downstream rotor/stator passage. (Figure 2.10)

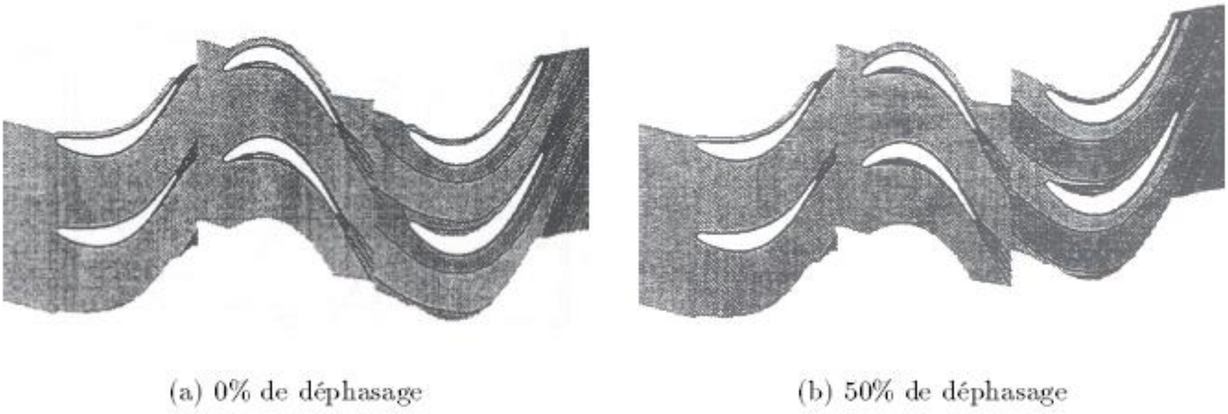
(a) 0% de déphasage

(b) 50% de déphasage

Figure 2-10 Clocking effect between two stators in a turbine mid stage (Eulitz F., 1996)

Moreover, some investigations (Smith, L H., 1966) in a low speed axial compressor highlight performance improvement due to the reduction of axial spacing between the adjacent blade rows, and he presented for the first time the effects of the recovery of wake decay to explain the experiment result. A wake is chopped by a downstream blade row and a segment of mass of the wake is tracked. Smith considered the case of a compressor stator wake being chopped by a rotor. The stream of dye is chopped by the rotor and the dye segments are rotated and stretched in the rotor passage. Smith postulated that this stretching process would lead to a reduction of the wake deficit as follows. If the fluid is considered 2D, incompressible, and inviscid, the vorticity of each fluid particle is constant by Kelvin's theorem. The wake segment is stretched in the downstream blade passages shown in Figure 2.11, but the circulation around the contour C is constant as the contour length increases. When the constant value of circulation is combined with mass conservation, one finds that the velocity difference between the wake and free stream decreases inversely to the wake length. Thus, as the wake is stretched the wake deficit is attenuated. The process is called wake recovery and is defined as the attenuation (or amplification) of the wake velocity profile by processes other than viscous dissipation occurring inside a blade row.

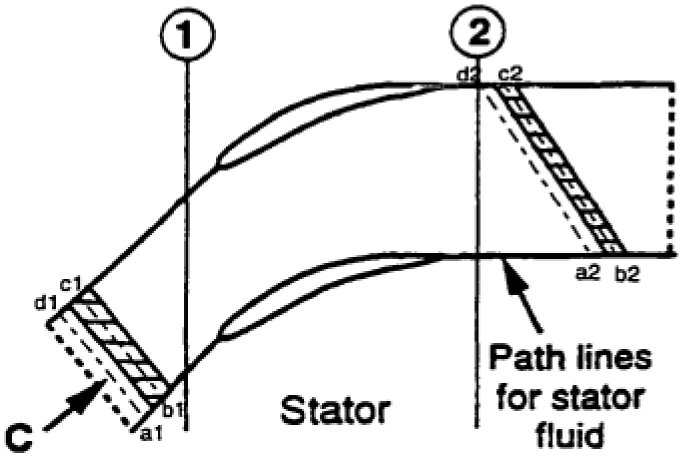

Figure 2-11 kinematics of rotor wake in stator passage

The recovery process that causing a change in the efficiency with a change in axial gap was explained in detail by Van de Wall et al. (Van de Wall, A G, Kadambi, J R, Adamczyk, 2000).In their opinion, the closer the spacing between blade rows, the higher the efficiency obtained in a subsonic compressor. While, the wider the spacing between blade rows, the higher the efficiency obtained in a subsonic turbine.

2.2.6. TIP LEAKAGE

Side flows are inherent to turbomachinery as they result from the presence of technological clearances between the fixed and rotating parts of machinery. Among different types of side flows are leakage flows over the rotor and stator blade tips of unshrouded blades, labyrinth flows over shrouded rotor blades and through stator root seals, windage flows at the rotor disc and discharge flows through the rotor disc discharge holes. A sample diagram of distribution of flow is presented in Figure 2.12. Leakage streams bypass the blade-to -blade passage and do not yield work to the rotor. Therefore, they are sources of power loss in turbines.

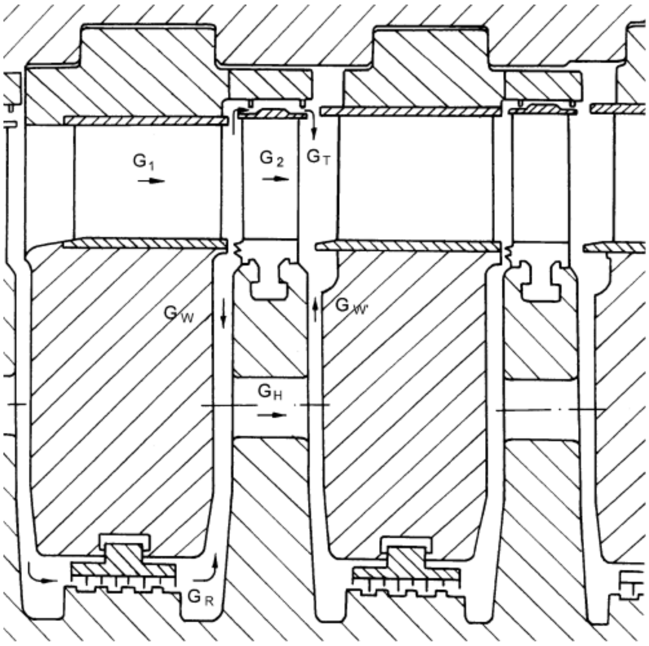

Figure 2-12 - Impulse turbine geometry; G1, G2 – mass flow rates of the main flow in the blade-to -blade passage of the stator and rotor, GT , GR – flow rates of leakages at the rotor blade tip and stator root, GW , GW0 – windage flow rates at the rotor disc, GH – flow rate at the rotor disc discharge holes

This paragraph is focused on the main form of leakage flow i.e. the tip leakage over the rotating rotor blade. The tip leakage is characterised by parameters different than those of the main stream. Particularly important is the difference between the magnitudes and directions of the leakage flow and main stream velocities, which gives rise to mixing losses on the re-entry of the leakage stream to the blade-to -blade passage. It is also important to note that the mechanism of formation of the tip leakage over unshrouded free-tip blades is different than that of leakage over shrouded blades. Only the former will be considered in this brief overview.

Figure 2.13 illustrates the mechanism of formation of the tip leakage in the gap over unshrouded rotor blades and its further development in the blade-to -blade passage. The driving force for this type of leakage is the pressure difference that is formed over the blade tip between the pressure and suction surface of the blade. Due to a usually significant pressure gradient, the leakage stream is largely accelerated in the tip gap. At the entrance to the tip gap, the tip leakage typically separates from the sharp edge of the blade tip and it is contracted into a narrow stream between the separation region and endwall. Here, the leakage stream becomes turbulent and mixes with the shear layer separating it from the stagnation area. Downstream of the gap the leakage faces the adverse pressure gradient in the channel and separates from the endwall forming a vortex structure that is convected downstream merging with the main stream in the blade-to -blade passage. The tip leakage follows the pressure gradient along the tip gap, so its direction on the re-entry to the blade-clearance passage forms an oblique angle with the main stream direction.

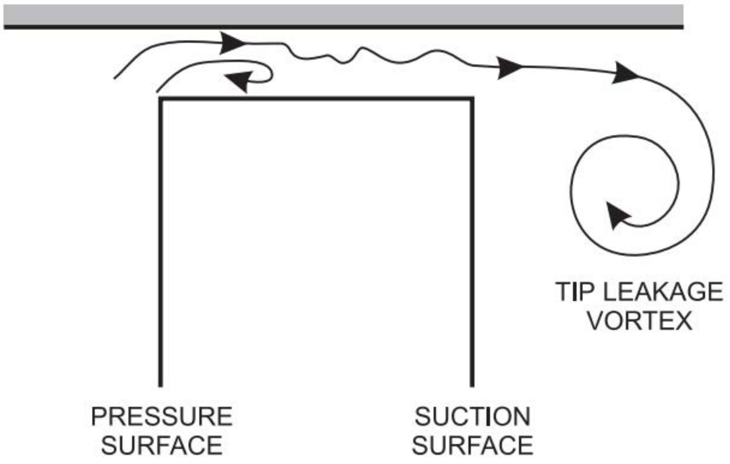

Figure 2-13 - Scheme of the tip leakage over rotor blades

The flow at the tip endwall approaching the tip region above the leading edge of the blade is divided into two streams aiming towards low pressure regions above the suction surfaces of the neighbouring blades – a main stream of the tip leakage flow going through the tip gap over the blade and a stream of cross-flow going across the blade-to -blade passage [12]. The tip leakage flow leaving the tip gap separates from the endwall under conditions of adverse pressure gradient and forms the tip leakage vortex. The cross-flow blocked by the development of the tip leakage vortex also separates from the endwall and rolls up into a passage vortex. The stream dividing line between the tip leakage and cross-passage flow lies at the pressure side of the blade tip. The described situation is illustrated in Figure 2.14.

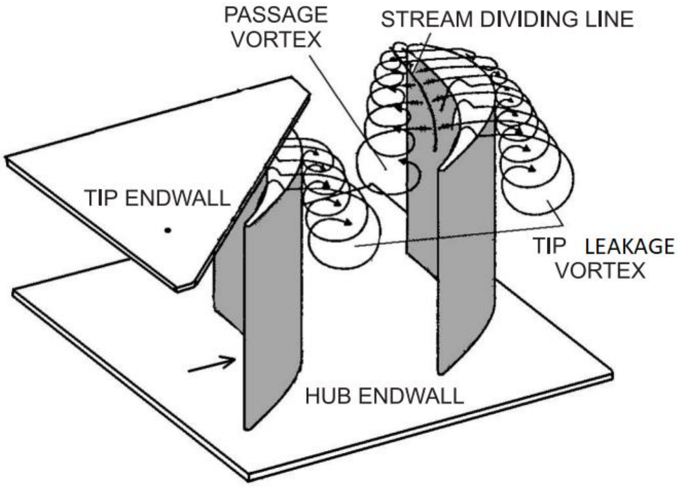

Figure 2-14 Tip leakage vortex and passage vortex at the tip endwall

The tip leakage vortex and passage vortex are characterised by the opposite sense of rotation. The dominant structure is the tip leakage vortex. The relations between the circulation and size of the two structures depend on many factors including the tip gap size, flow turning angle, blade load and incidence angle. For a typical low-load rotor cascades for the nominal inflow and typical tip gap size ranging between 1–3%, the circulation of the tip leakage vortex is several times larger than that of the passage vortex.

The tip leakage vortex is also responsible for another phenomenon called *blockage*. (Yasunori Sakuma et al., 2014), studying the effect of a grooved case in a transonic flow compressor, defined the blockage region as a surface in which the mass flow passing through is smaller than a certain critical value (Figure 2.15). This is to say that the tip leakage vortex, impacting the following blade wall, obstructs partially the main flow passage enhancing the possibility for the inception of the rotating stall.

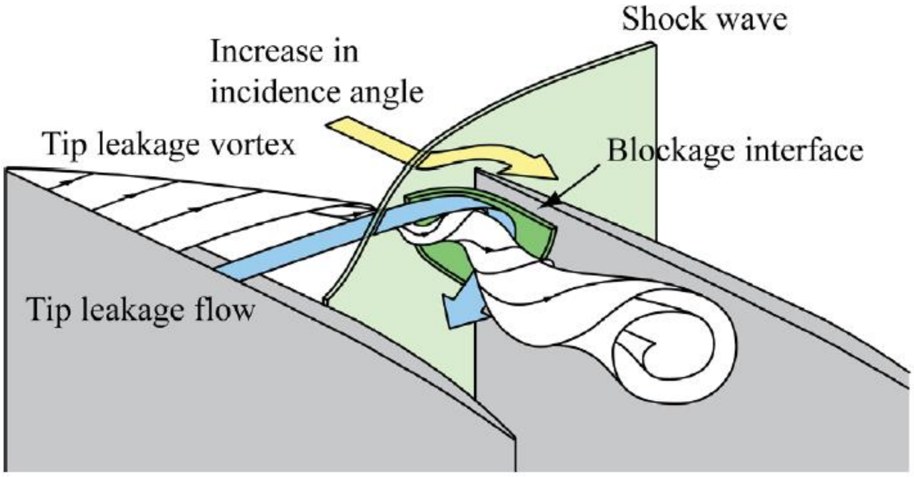

Figure 2-15 Schematic of near tip flow field

The tip leakage region is characterised by a high level of flow turbulence. Production of turbulent kinetic energy and its dissipation is a significant source of flow losses. The results of detailed measurements presented in (Moore J G, 1996)indicate the turbulence intensity of 30% (with respect to the inlet velocity) in the region of separation of the tip leakage flow from the endwall, in the tip leakage vortex and passage vortex as well as in the region of high stress resulting from interaction of the two vortex structures. The turbulence intensity of the leakage stream in the tip gap exceeds locally 26% (with respect to the outlet velocity).

2.2.7. FLUTTER

Blade flutter is the self-excited vibration of blades due to the interaction of structural-dynamic and aerodynamic forces. Flutter is a problem for turbomachinery because of the possible phase differences between the blades when they are vibrating. If the blades are identical, the aeroelastic modes (coupled structural and aerodynamic system) are patterns of blade vibration with a constant phase angle between adjacent blades. Each aeroelastic mode has a different inter-blade phase angle. The inter-blade phase angle affects the phase between the local unsteady flow and local blade motion which in turn affects the unsteady aerodynamic work done on the blades. Adverse phase angles can lead to positive work being performed on the blades which results in flutter.

In a linear system, 'flutter point' is the point at which the structure is undergoing simple harmonic motion, zero net damping, and so any further decrease in net damping will result in a selfoscillation and eventual failure. 'Net damping' can be understood as the sum of the structure's natural positive damping, and the negative damping of the aerodynamic force.

For nonlinear systems, flutter is usually interpreted as a limit cycle oscillation (LCO), and methods from the study of dynamical systems can be used to determine the speed at which flutter will occur.

2.2.8. SURGE

A noticeable feature of any compressor performance map such as Figure 2.16, is the surge line. This line denotes the limits to stable operation. It can be reached by reducing the mass flow, with a throttle valve, whilst the rotational speed is maintained constant. When a compressor goes into surge the effects are usually quite dramatic. Generally, an increase in noise level is experienced, indicative of pulsating air flow and of mechanical vibration. Surge is a one-dimensional instability where a low frequency pressure wave, usually from 2 to 50 Hz with a great amplitude, propagates in the axial direction and is able to modify main flow stream.

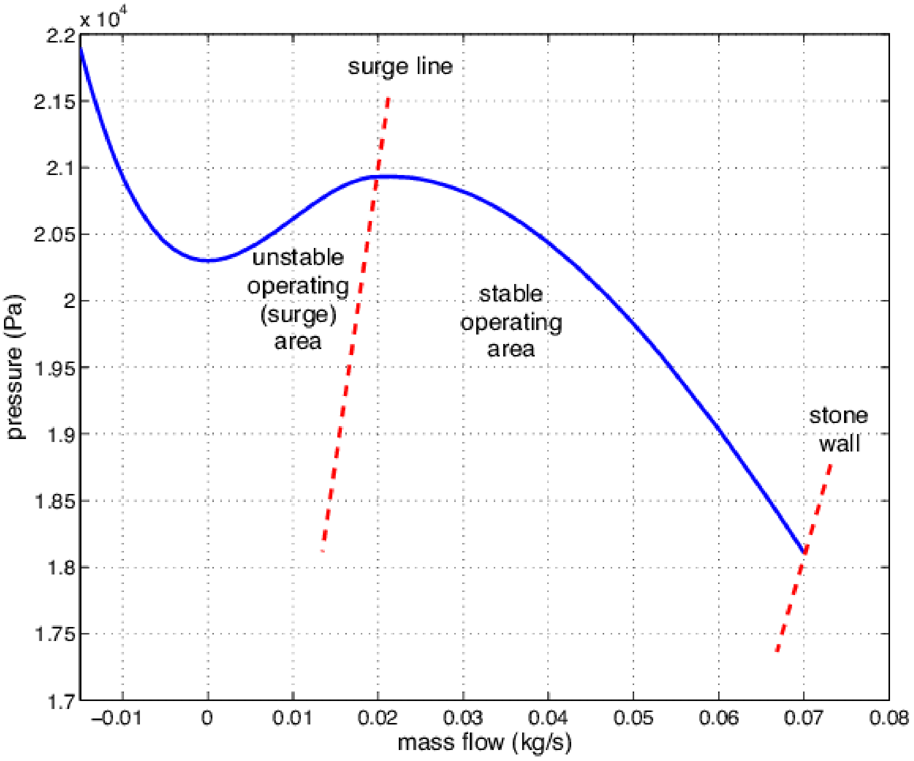

Figure 2-16 Compressor map with a surge line

In figure 2.17 an illustrative scheme is proposed: the stable operational field is characterized by the overlap of the machine and system lines; the separation occurs near point A where we have the inception of the unstable phase triggered by the first rotating stall cells. From point A to B the performance falls so dramatically that the energetic level of the system remains higher than the machine level (A→B, phase ruled by the system inertia). Vice versa the opposite happens from point B to A (B→A, phase dominated by the machine). The huge system inertia prevents the two outer points to be stable operational points, this is why the machine needs a flow increment in order to exit from the hysteresis loop.

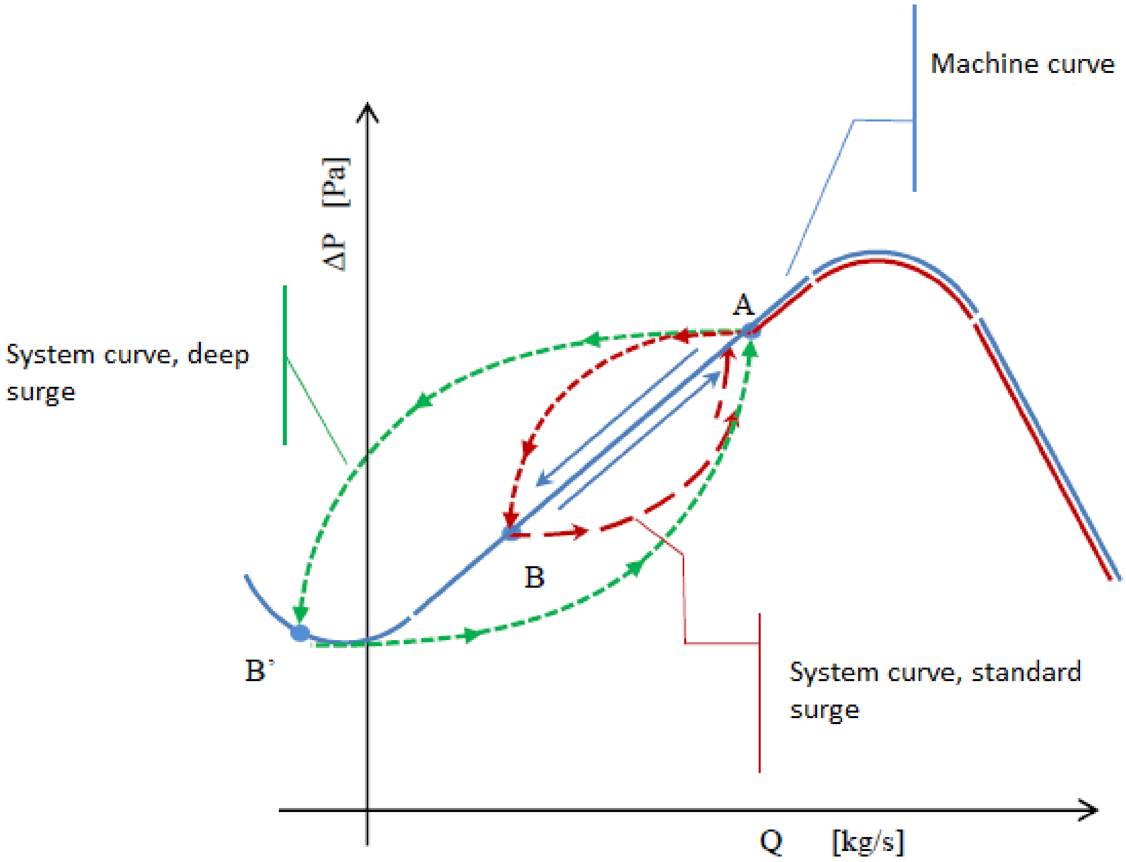

Figure2-17 Surge cycle in a compressor (Veglio M., 2015)

There are many different variants of this phenomenon depending on the size of the machine. In some cases the surge is moderate and remain within the positive flow field; this is commonly seen in machines characterized by a lower pressure ratio. Bigger machines are distinguished by a deeper type of surge where the flow fluctuations are so high that negative values can be reached. Finally, Stein (Stein A., 2000) introduced a modified phenomenon, called modified surge, characterized by the persistence of rotating stall cells with during the flow surge fluctuations

2.2.9. ROTATING STALL

Rotating stall is the main focus of this work. Thus, a more thorough explanation of the phenomenon is going to be presented coupled with the achievements obtained in the past years; it represent one of most serious problem areas in turbomachinery aerodynamics, constraining the operating range of an axial compressor being something to be avoided at all costs. Unlike surge, it remains delimited in the machine area where the circumferential flow pattern is disturbed.

Stall is a term used in aerodynamic to indicate the *lift* loss of an airfoil or, equally, the flow detachment along the airfoil wall. The phenomenon is manifested through one or more *stall cells* of reduced, or stalled, flow that propagate around the compressor annulus at a fraction of the rotor speed. The term *cell* indicates a behaviour happening in a portion of the whole compressor whilst the term *rotating* is referred to its movement in the compressor annulus. Rotating stall leads to reduction of the pressure rise of the compressor, and in the compressor map this corresponds to the compressor operating on the so called in-stall characteristic. In addition, there is also the problem of vibrations in the blades as stall cells rotate at a fraction of the speed, as explained below. Moreover, if a natural frequency of the blades coincides with the stall cell frequencies passage, it is likely to have a mechanical failure due to fatigue.

The basic explanation of the rotating stall mechanism can be summarized in Figure 2.18: considering 3 blades in sequence A, B and C in a row of axial compressor blades operating at high angle of attack and supposing that there is a little non-uniformity in the inlet flow such that a locally higher angle of attack is produced on the blade B which is enough to stall it. The flow now separates from the suction surface of the blade producing a flow blockage between the stalled blade B and the following one C. This blockage causes a diversion of the inlet flow away from the stalled blade towards the following (C) and the previous blades (A), resulting in an increase angle of attack on C, causing it to stall, and helping A in regaining a better attach angle. In this way the stall cell propagates along the blade row. In the impeller reference system, the stall cell seems to move in opposite direction compared to the rotation, thus, in an absolute reference system, it moves at a lower speed than rotor.

In elementary terms, stall is a disturbance of the flow in the tangential direction, while surge is a disturbance in the axial direction. During stall, the average flow rate passing through the compressor is steady while, during surge, the flow rate will pulse. Both of these phenomena occur at the same instability point of the performance map, but the length and volume -system inertia- of the compressor system determines which instability will be dominant. Greitzer developed (Greitzer E., Surge and Rotating Stall in Axial compressors - Part I: Theoretical compression System Model, 1976) a model representing the dynamic behaviour of the system and the B parameter: a non-dimensional grouping of system variables which indicates whether a particular configuration will stall or surge.

$$B = \frac{U}{2a}\sqrt{\frac{V}{AL}} \rightarrow \frac{Pressure\ force}{Inertial\ force}$$

The ration shows that if inertial forces are dominant, the compressor will only experience rotating stall, but if pressure forces are the strongest, after a brief period of rotating stall, the flow in the compressor duct is force to decelerate and reverse.

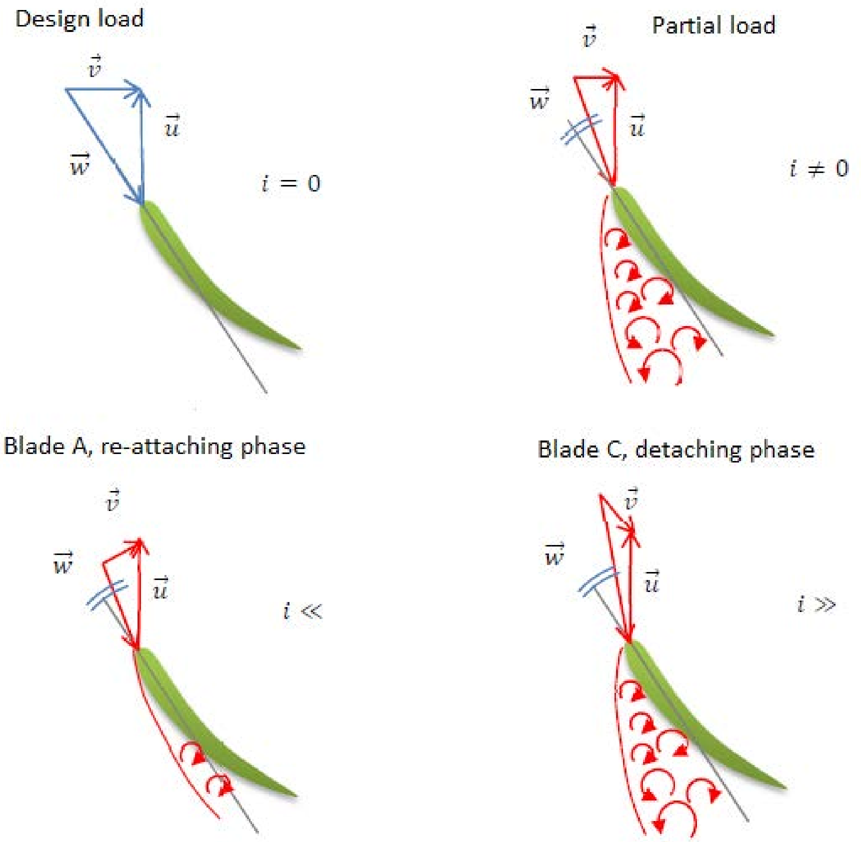

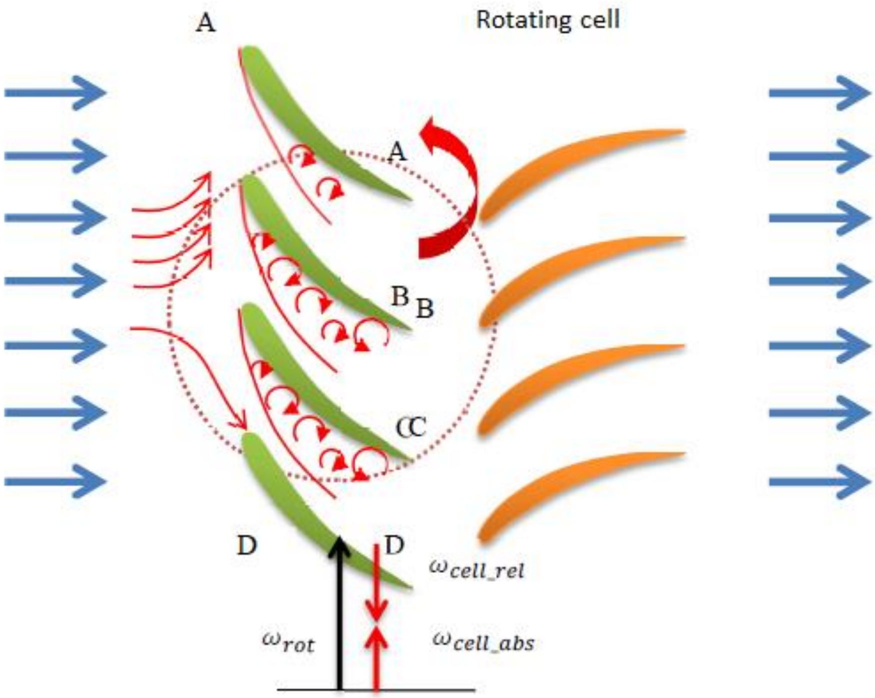

Figure 2 -18 Physical mechanism for inception of rotating stall (Veglio M., 2015)

Rotating stall is an instability arising at partial loads in both centrifugal and axial compressors, although there is little theory about centrifugal compressors and its importance is still a matter of debate. In fact, many centrifugal compressors and low-pressure rise axial machines do not exhibit a discontinuous pressure characteristic at the stability limit as shown in Figure 2.19.

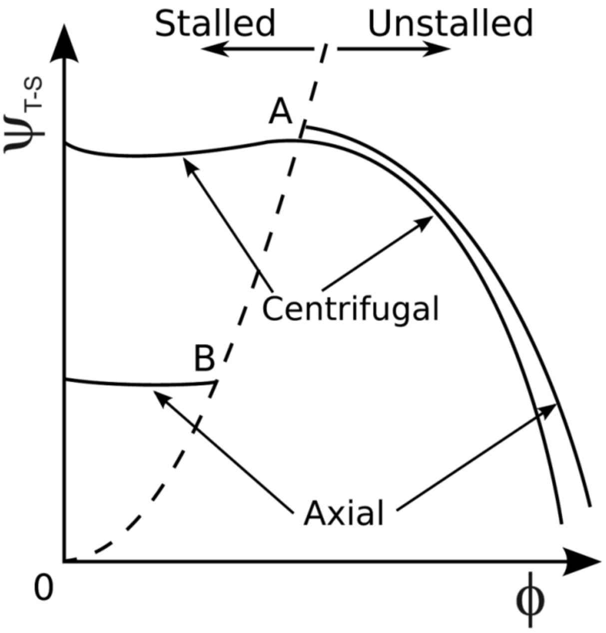

Figure 2-19 Centrifugal and axial compressor characteristics illustrating the difference in pressure level after stall has occurred (Day I., 2016)

STUDIES ON ROTATING STALL FEATURES AND PERFOMANCES

Rotating stall is an unsteady phenomenon in continuous evolution. It doesn't exist a single type of rotating stall instead different kind of it can be observed, even for the same machine, varying the flow rate. Cells number, extension and movement are not constant from their inception to the final development just before surge appearance.

It is common to distinguish between at least two types of rotating stall as showed in Figure 2.19: full-span and part-span. In full-span, the complete height of the annulus is stalled with a maximum of two cells rotating simultaneously at maximum at 60% of the machine rotation speed. In part-span, a limited region of the blade passage is stalled with the presence of several cells (even more than 10), faster than the previous case, rotating at least at 40% of the machine rotation speed. Full-span stall is most likely to happen in high hub/tip ratio axial compressor while part-span stall is more relevant to high speed multistage compressors.

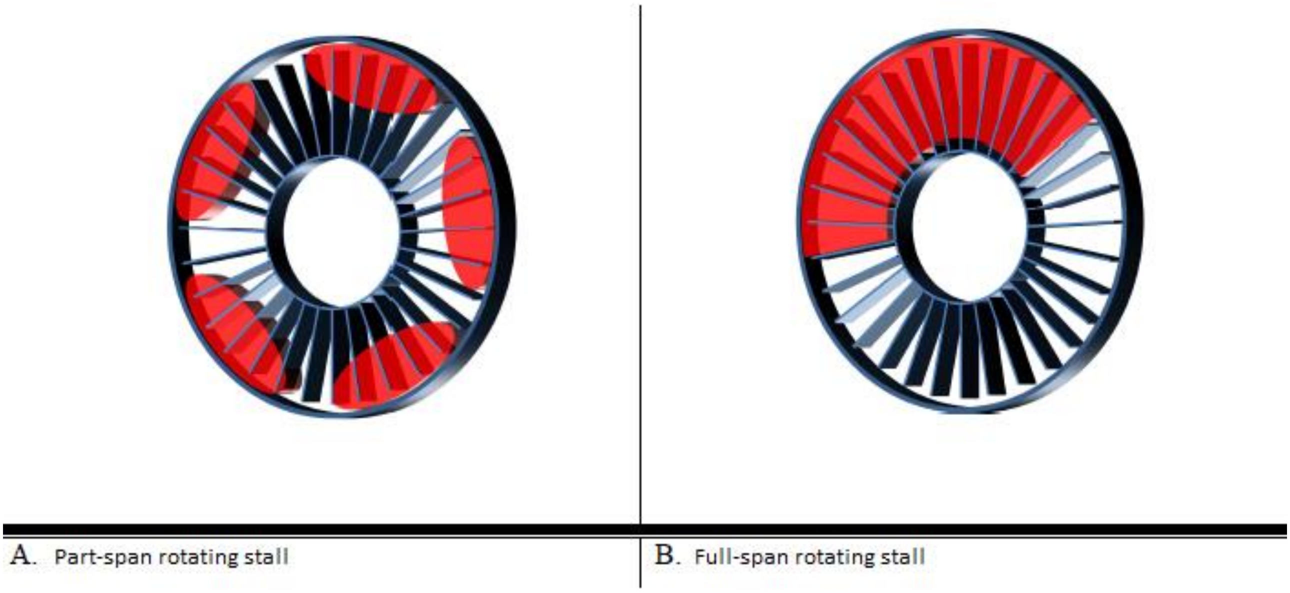

Figure 2-20 Different rotating stall configuration (Veglio M., 2015)

In 1973, Mckenzie proposed a model (Figure 2.21) in which the stalled and unstalled sectors of the annulus work separately in points C and D respectively. The former has no net flow and the latter full flow of the stable characteristic. The stalled sector of the annulus is given by $(D - B)/(D - C)$. In this model points B, C and D have the same static pressure as they were two compressors working in parallel between the two pressure values. It is important to notice that this points position is empirically fixed at 0.15N, where N is the number of stages.

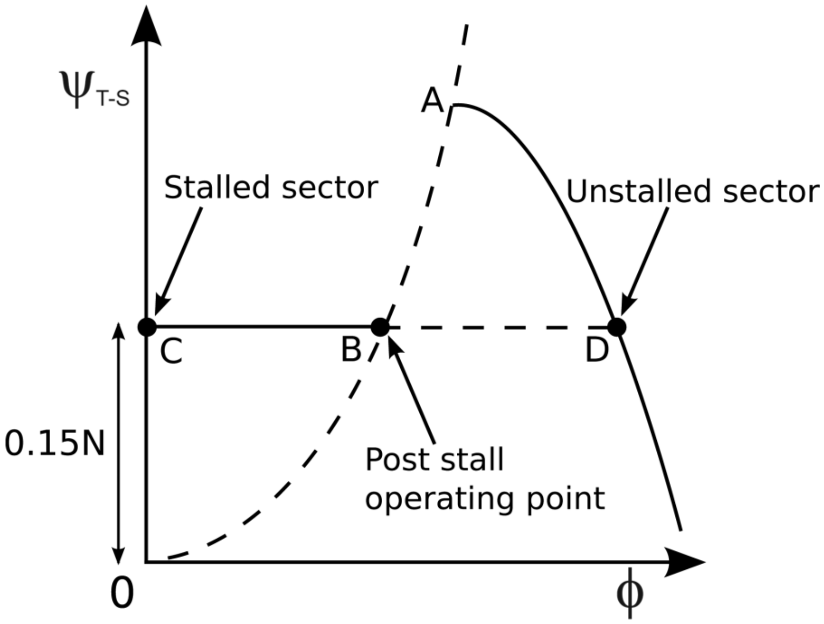

Figure 2-21 Parallel compressor model proposed by Mckenzie

In 1978 (Day I. G. E., 1978) Mckenzie's idea was extended by Day, Greitzer and Cumpsty who observed that the part-span cells seldom occupy more than 30% of the annulus and full-span cells seldom occupy less than 30%. Thus, depending on the characteristic map in stable operation, it is possible to estimate the type of cell formation by the pressure drop when the compressor stall for the first time. Figure 2.22 shows two compressors stalling at the same throttle setting for simplicity. It can be noticed that the pressure drop of compressor "Chic 2" is much more consistent than "Chic 1". The differences in the peak pressure levels of the two characteristics have direct implication for the type of stall cells which will form.

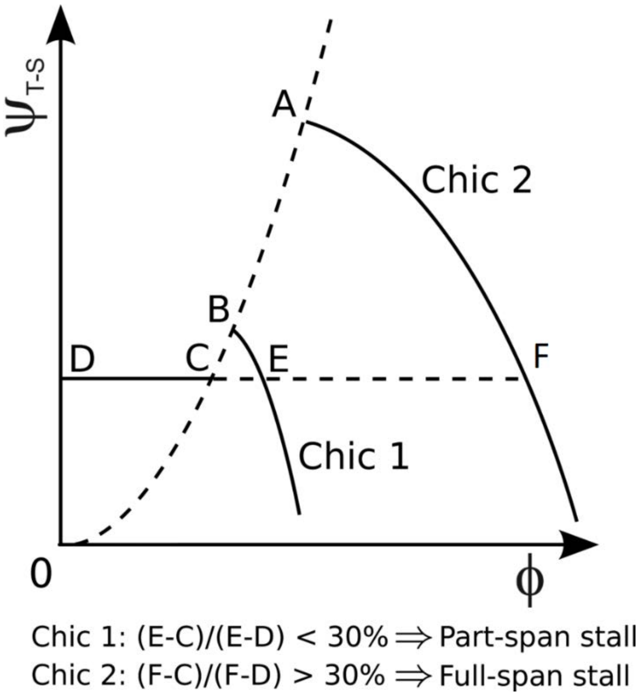

Figure 2-22 Example proposed by Day, Greitzer and Cumpsty

Day and Cumptsy (Day. I. J., 1978) used fast response instrumentation to obtain detailed measurements in a multistage compressor:

1. The average axial velocity in the stalled sector is near zero and in the unstalled section is above the design value. This corroborates the hypothesis of the parallel compressor model and certificated its reliability in estimating stall cell size and type.
2. The flow inside a large cell is very energetic and the tangential velocity upstream rotor is greater than wheel speed.

3. In u multistage compressor the stall cell extends axially through blade rows avoiding the stall cell. Figure 2.23.
4. The flow in a stall cell is highly three-dimensional due to high tangential forces.

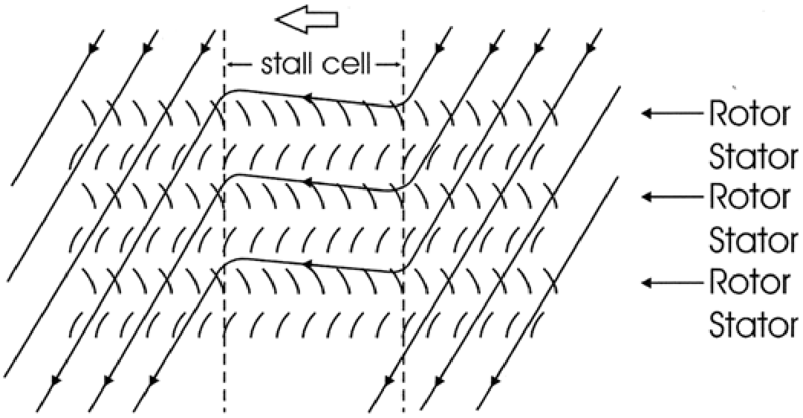

Figure 2-23 Stall extending radially through a multistage compressor

Day also identified five parameters affecting the type of cells generated: *Mach number* at design point, *stage number*, *speed rotation*, *hub/tip ratio*, *rotor blades/stator blades ratio.* A great *aspect ratio* promotes the inception of a single bigger cell while a low speed rotation promotes a bigger number of small cells

As we can see, stall development is strongly related to the geometric parameters of the machine. Machines with small *aspect ratio* and/or a wide blade tip gap between rotor and stator present the so called *progressive stall* type. Progressive stall has a gradual reduction in total pressure ratio after initiation of stall; as the flow rate decrease, the critical point is reached with the arising of several small cells that naturally reorganize themselves in smaller number of greater dimension as the flow rate decrease. This behaviour can be seen as a sequence of successive stable points. It is importance to notice that the machine works with a high risk of falling into surge.

Abrupt stall has a sharp discontinuity in the pressure ratio characteristic. Several small part cells convert into a bigger size full span one without any gradual progression. The machine quickly abandons its stable curve and starts operating with discontinuity at smaller ΔP. This behaviour is characteristic in machines with high aspect ratio and high pressure ratio.

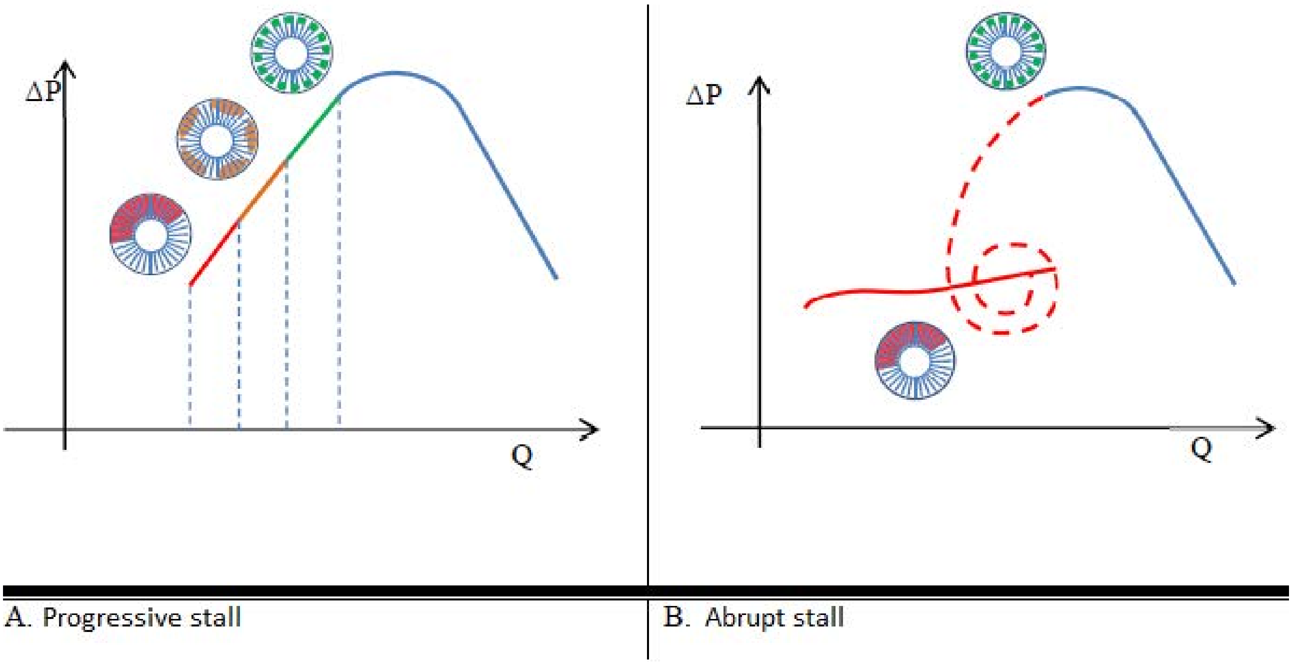

Figure 2-24 Transition from a stable operation point to rotating stall (Veglio M., 2015)

Some of the recent researchers have termed progressive and abrupt stall as modal and spike type of stall as it is going to be shown later in this work.

Another consequence of rotating abrupt stall is the hysteresis occurring when trying to clear the stall by using the throttle as shown in Figure 2.24. Initially the compressor is operating stably (B-C), then a disturbance drives the equilibrium over the surge line resulting in rotating stall (C-D). By opening the throttle, a higher opening than initially is required before the operating point is back on the stable compressor characteristic (F-H). There are several degrees of the severity of this hysteresis depending on the so called skewness of the compressors characteristic. Experimental evidence suggests that this problem gets worse as compressor pressure ratio increase.

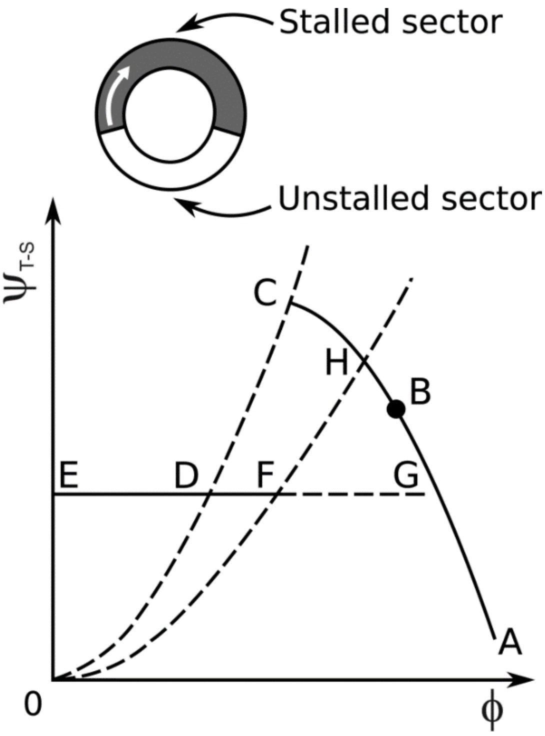

Figure 2-25 Typical fixed speed performance characteristic for an axial flow compressor

ROTATING STALL PRECURSORS

The background of the activity regarding the stall precursors lies in the theoretical works of Moore, Greitzer and Hynes in which velocity perturbations were predicted to precede the onset of rotating stall. The investigation carried out in the '90s allowed to discovered two different types of precursors:

- The first one was experimentally demonstrated by McDougall (McDougall N., 1990) whose experiment highlighted the presence of low amplitude long length scale disturbances called *"modes"* which rotates at less than 50% of the rotor speed.
- The other ones were observed by Day (Day I., 1993) in the rotor tip region, which were not of the long length-scale modal type but appear without warning, circumferentially small and localized. These disturbances were called *"spikes"* and rotates at about 70% of the rotor speed.

Figure 2.26 gives an example of the two types.

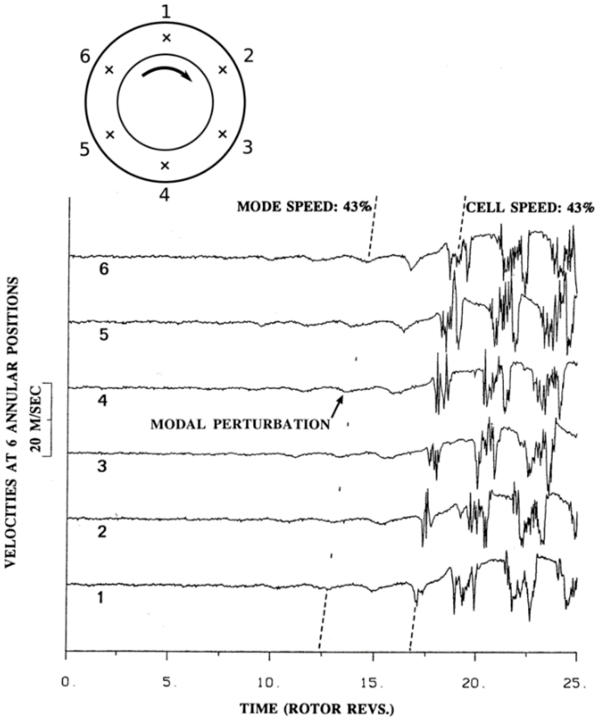

Figure 2-26a – Hot wire measurement around circumference showing modal activity before stall (Day I., 1993)

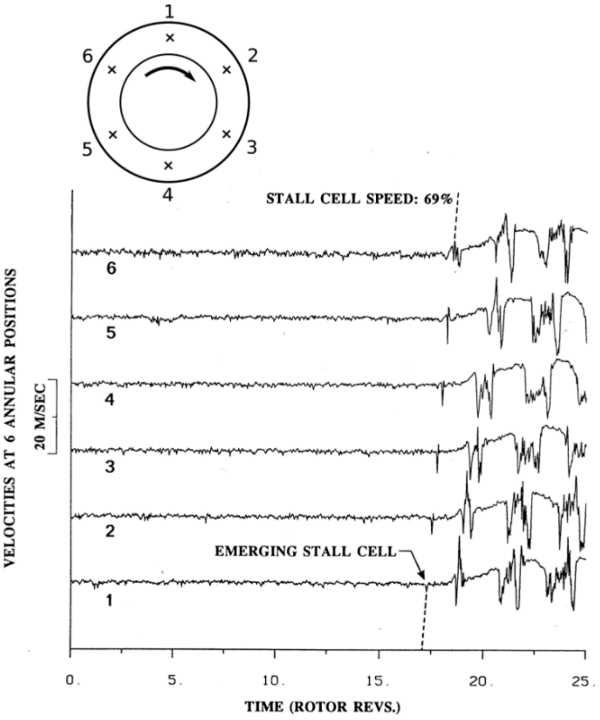

Figure 2-26b – Hot wire measurement around circumference of compressor showing spike-type stall inception (Day I., 1993)

Another achievement was obtained by Camp and Day (Camp T., 1998). Investigating why some compressors stall at the peak of the total to static pressure rise characteristic, as they should according to linear theory, while others stall before the peak is reached. They found that modes will only develop when the slope of the characteristic is zero or positive, while spikes often occur before this point is reached as showed in Figure 2.27.

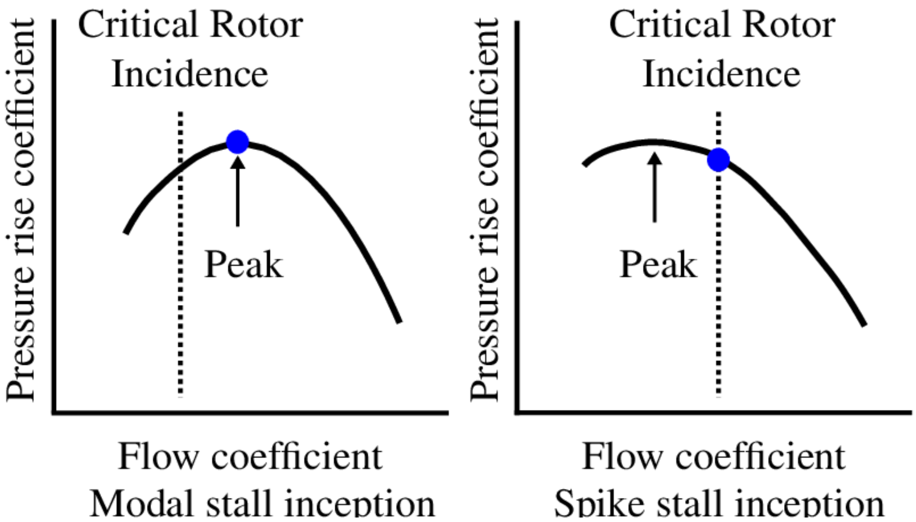

Figure 2-27 Left: modal stall inception criterion, right: spike inception criterion

Vo (Vo H., 2001) (Vo H. T. C., 2008) ,starting from the experimental measurements of Day, showing that spikes are not only circumferentially localized, but are confined to the tip region, leading to the possible association of their origin with the tip clearance flow, published its computational works.

He called flow solution limit is “the lowest flow coefficient for which a steady solution exists” . Flow solution limit occurs when the interface between the incoming flow and tip clearance flow lines up with the rotor leading edge plane.

Figure 2.28 shows the pattern if the interface between the tip clearance flow and the incoming main flow where the position of this interface results from the balance between momentum main flow and the momentum tip clearance flow. As the main flow decreases, the blade loading, which drives the tip clearance flow, increase. The computations carried out by Vo show that when the solution limit is reached the incoming/tip clearance interface is aligned with the rotor leading edge plane at the blade tip

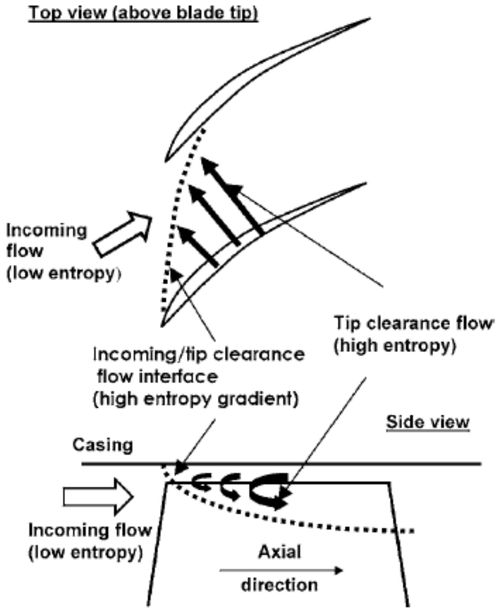

Figure 2-28 Sketch of incoming/tip clearance flow interface

He found two conditions happen in the transient beyond the flow solution limit:

- One feature of the transient is the spillage of tip clearance flow to the adjacent blade passage ahead of the rotor leading edge and below the blade tip radius.
- A second feature seen at flow coefficient below the flow solution limit is that fluid originating from the tip clearance moves into the blade passage at the trailing edge. The trajectory of this fluid is such that there is impingement on the pressure surface. This reversal fluid from the adjacent blade passage has been called tip clearance backflow.

Figure 2.29 illustrates the role of leading edge spillage in setting the flow solution limit. The left sketch depicts the tip clearance flow trajectory for a situation in which spillage has not occurred, and the right sketch when there is leading edge spillage. With the incoming/tip clearance flow interface inside the passage the tip clearance fluid, as well as any backflow, either convects downstream or leaks through the adjacent tip clearance. However, leading-edge spillage below the blade tip means that the tip clearance fluid has an additional path by which it can move upstream, especially when displaced by the backflow.

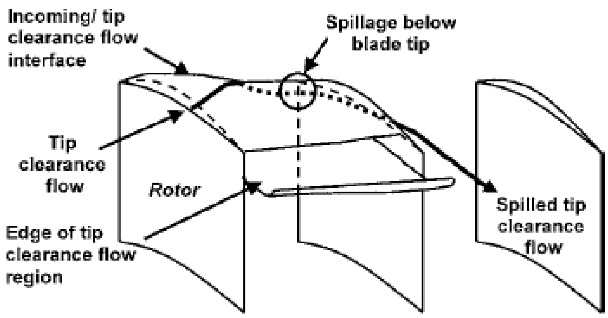

Figure 2-29a – Leading-edge tip clearance flow spillage below blade tip

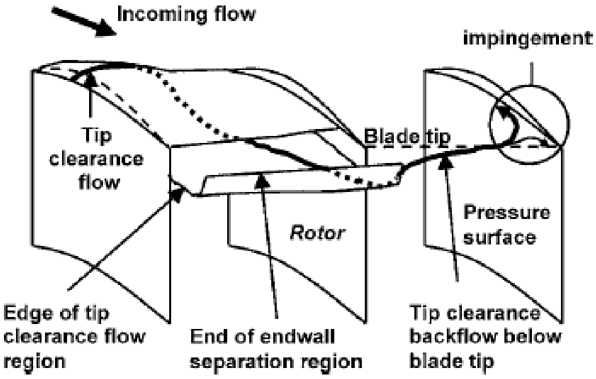

Figure 2-29b – Backflow of tip clearance fluid below the blade tip

These results were corroborated by the experimental measurements of Deppe (Deppe A., 2005) who used cranked pressure probes installed upstream and downstream of the rotor (Figure 2.30) in order to determine the stall inception process and its motion relative to the rotor right from the beginning.

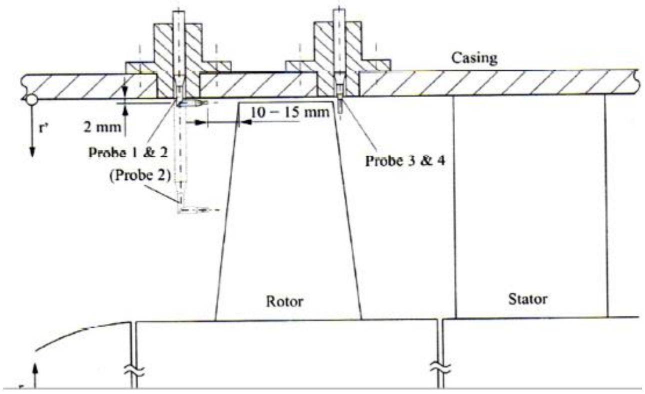

Figure 2-30a – Probe arrangement (radial)

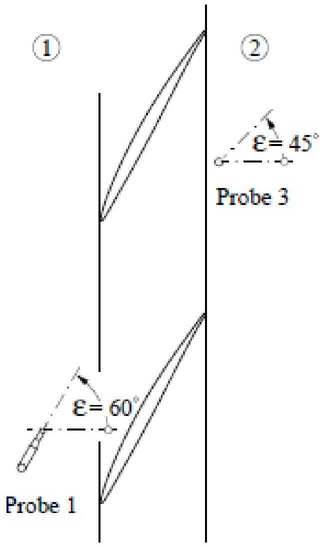

Figure 2-30b – Probe arrangement (circumferential)

He also found that the negative slope for the total-to-static pressure characteristics at the last stable operating points indicates spike-type stall inception. The disturbance was detected by the probe close to the casing wall. After the initial spike, the disturbance grows in circumferential as well as radial direction until, after less than 10 rotor revolutions, again a steady state fully developed stall cell phenomenon is reached.

In order to have an insight into the tip clearance flow field they sketched maps, in pressure coefficient, for casing wall pressure distribution near stall $\widetilde{c_p}$ and the corresponding pressure standard deviation $\tilde{c}_{p,rms}$. The minimum pressure point is located on the casing wall next to the profile suction blade side (line (a)) indicating the existence of a tip clearance vortex. The grey band area is associated to high value of pressure fluctuations indicates the vortex trajectory. In Figure 2.31 represents the final interaction between the incoming flow and the backward directed tip clearance flow, where the clearance vortex has moved upstream due to the decrease of the incoming flow rate.

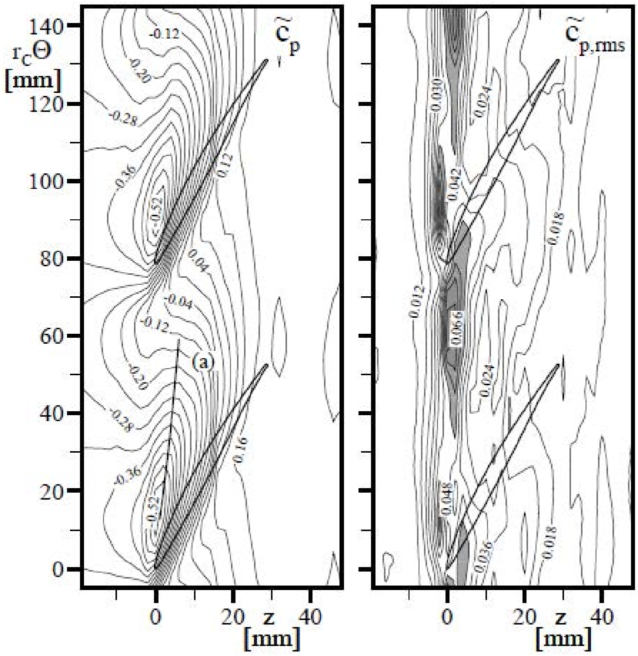

Figure 2-31 Casing pressure distribution

According to Vo, an additional condition for spike-type stall inception must be fulfilled simultaneously with the unsteady spillage of tip clearance flow ahead of the rotor blade leading edge. This condition is the appearance of an unsteady backflow at rotor outlet close to the casing wall. Figure 2.32 shows pressure traces obtained from two probes indicating that the conditions required were met: the pressure signals indicates that backflow occurs near the trailing edge and spill forward near the leading edge of the same blade.

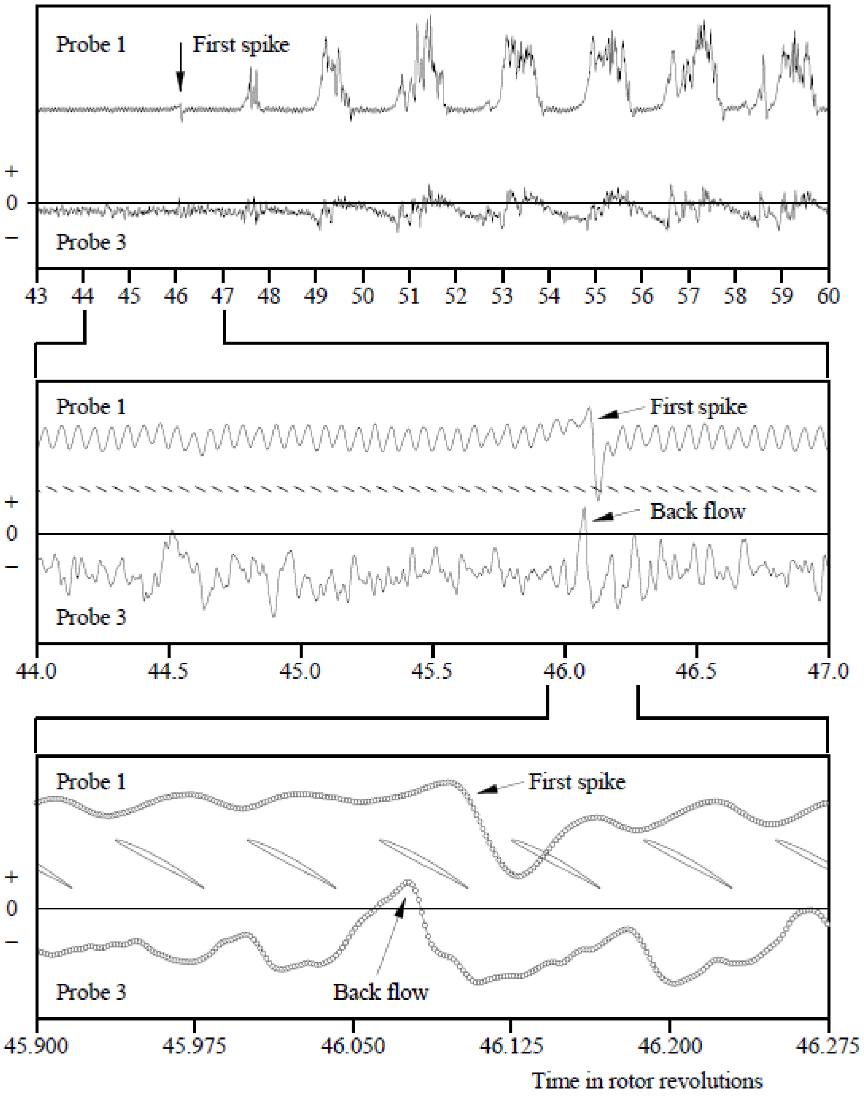

Figure 2-32 Pressure distribution up- and downstream of the rotor

Pullan, Young, Day, Greitzer and Spakovszky (Pullan G., 2015) proposed a huge work supporting the vortex behaviour of the spike as a possible cause for the peak and subsequent pressure drop. The idea of this mechanism was initially suggested by Inoue (Inoue M., 2000). They asserted that tip clearance flow is not necessary condition for spike formation because there are at least two sets of experiments showing the contrary: spike happening in a tip shrouded axial compressor and in centrifugal vaned diffuser.

Their proposed model is shown in Figure 2.33. Main flow high incidence results in a separation from the leading edge in the outer part of the blade. The vortex shed forms a vortex tube that spans from blade to casing convecting as indicated by the arrows. Spike propagates when a new vortex is formed by the separation of the subsequent blade and.

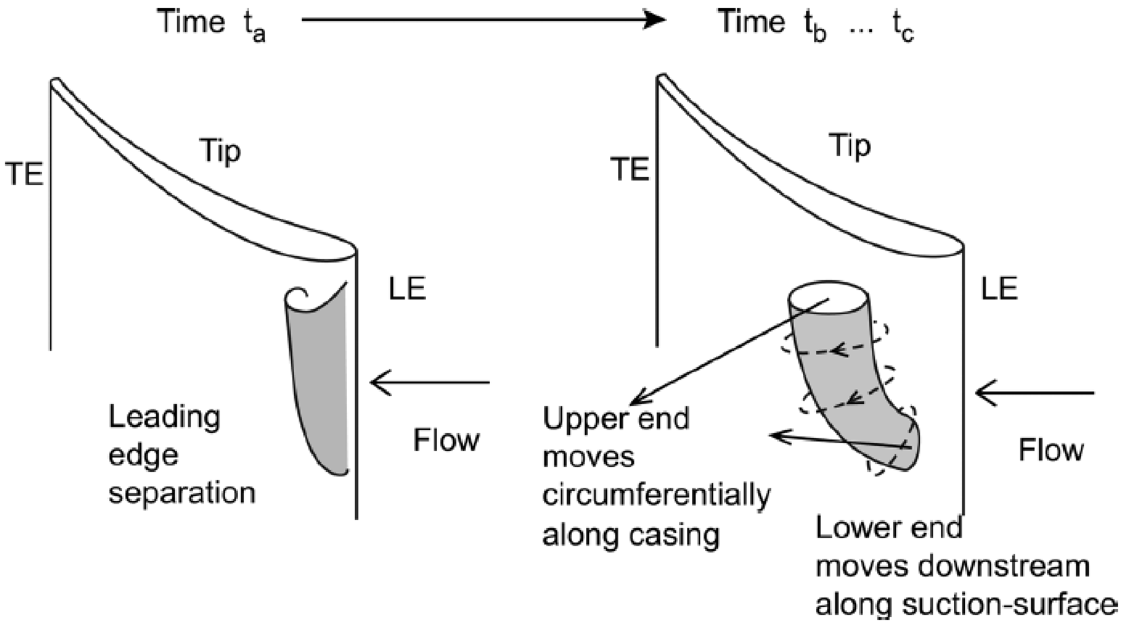

Figure 2-33The vortical structure and propagation of the spike

A stationary sensor would then first encounter the potential field of the blockage caused by the leading edge separation, i.e. the pressure rise, and then a sharp pressure drop as the vortex tube crosses the transducer causing the typical up-down waveform of the spike as shown in Figure 2.34.

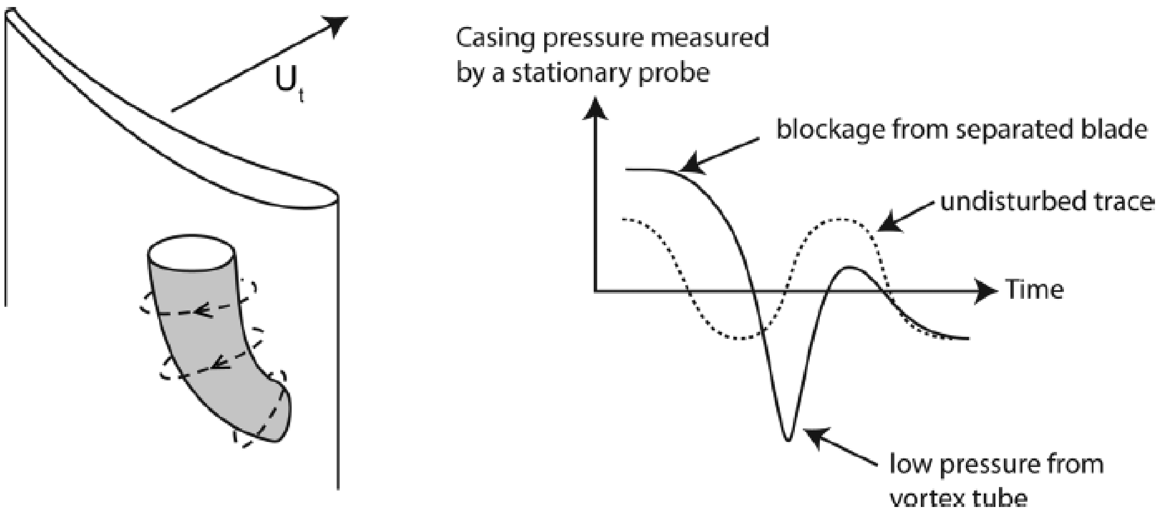

Figure 2-34 connection between spike structure and casing pressure trace

They showed three different numerical simulation with increasing complexity (2D, 3D with zero tip clearance, 3D with tip clearance) in order to isolate the origins, structure and propagation mechanism of spike-type disturbances from other phenomena happening in the machine. Finally, they compared these results with experimental measurements on a Cambridge low speed compressor showing the high level of agreement. (Figure 2.35).

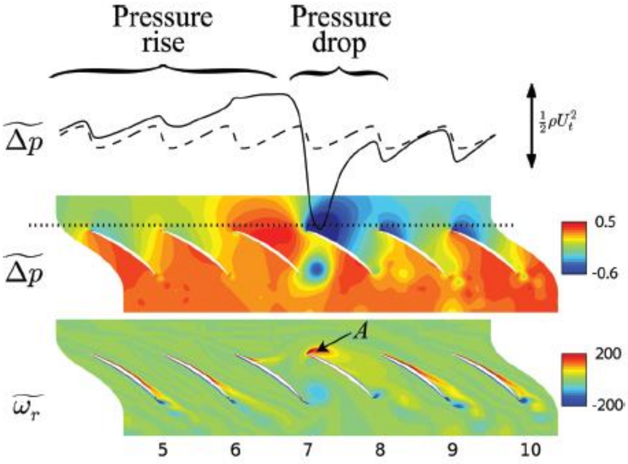

Figure 2-35a - Spike cause by leading edge separation in 2D tip profile cascade.

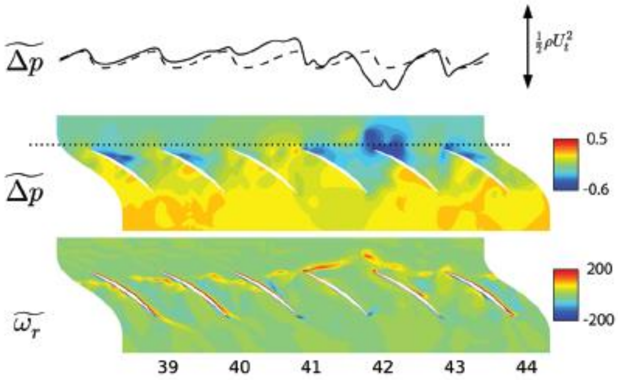

Figure 2-35b - 3D Spike formation in a rotor with clearance, 95% span.

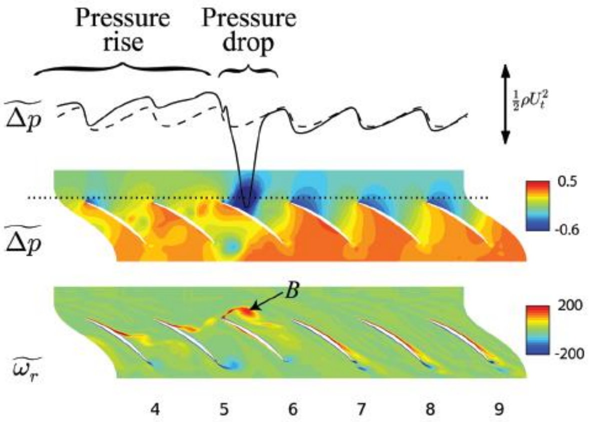

Figure 2-35c - Spike cause by leading edge separation in a zero clearance rotor, 95% span.

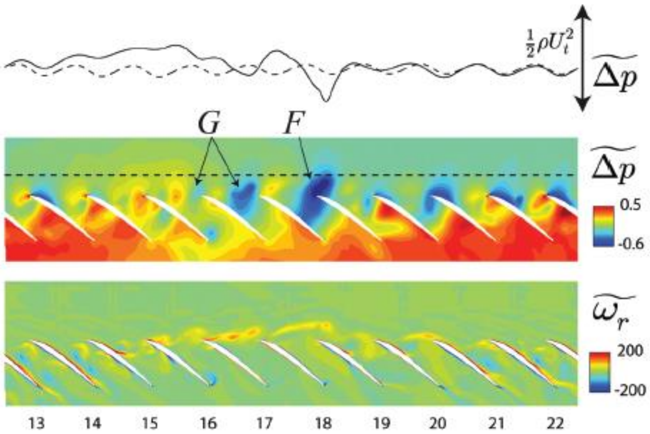

Figure 2-35d Spike cause by leading edge separation in the Cambridge compressor.

A conclusion to the chapter a summary of the dominant features which characterize the stalling process of an axial compressor proposed by Day (Day I., 2016) is reported below with the help of Figure 2.25:

- In a compressor of similar stage loading and flow rate to an aero-engine (ϕ =0.4 and θ=0.6), stall is always accompanied by a sudden loss of pressure rise. From C to D.
- The flow rate at which stall occurs, more-or-less, coincides with the peak of the total-to-static pressure rise characteristic, i.e., point C. (Note that the "stall margin" of a compressor is represented by the operating range between the design point, B, and the stall point, C.)
- The discharge throttle setting at which compressor will unstall is always greater than that at which it first stalled. This gives rise to a hysteresis loop: C, D, F and H. The size of this loop increases with the design pressure rise and flow rate of the compressor.
- The flow in a stalled compressor will always divide into clearly define sectors of stalled and unstalled flow.
- A stall cell always rotates in the same direction as the rotor blades, but a slower speed.
- Highly loaded blades of low aspect ratio usually give rise to a single full-span cell. Long blades usually produce multiple part-span cell near the casing.
- When stall occur, the flow breakdown process nearly always begins in the vicinity of the rotor tips.
- Stall inception may be initiated by long-scale disturbances (modes; measured in terms of circumferential length) or by short length-scale disturbances (spikes; measured in terms of blade pitches). Between these two "pure" forms of stall inception there is a whole range of flow breakdown patterns which are neither of one type nor the other.
- Part-span cells rotate faster than full-span ones and, in general, the smaller the disturbance he quicker it will rotate.
- Pre-stall disturbance, i.e. disturbances occurring at flow rates greater than the stall point, are sometimes observed in the form of radial vortices oscillations of the tip clearance flow. These disturbances are usually referred as rotating instabilities and are most likely to be observed when tip clearances are large.

The top points of this list are always true while, as we move down, we find flow features which occur with less certainty and at the end there is the discussed area of pre-stall activity. It's importance to note that the uncertainty surrounding the stall behaviour of a new compressor disappear once it has been stalled for the first time. A compressor which is stalled repeatedly will stall at the same flow coefficient each time as the number and the speed of the cells and while the stall inception patterns will only differ in minor detail.

3. TEST RIG AND MEASUREMENT TECHNIQUES

As anticipated in the introduction, the data utilized in the analysis are the ones collected by Veglio (Veglio M., 2015). For a more detailed explanation of how the measurement were perfomed, her work is downloadable for free online. The test rig AX-200, shown in Figure 3.1, was used to acquire data. It is located in Lille in the turbomachinery laboratory of the ENSAM university. It's composed of a single stage axial compressor CME2, alternative electric motor, speed regulator, micro-filter and a mechanical reducer.

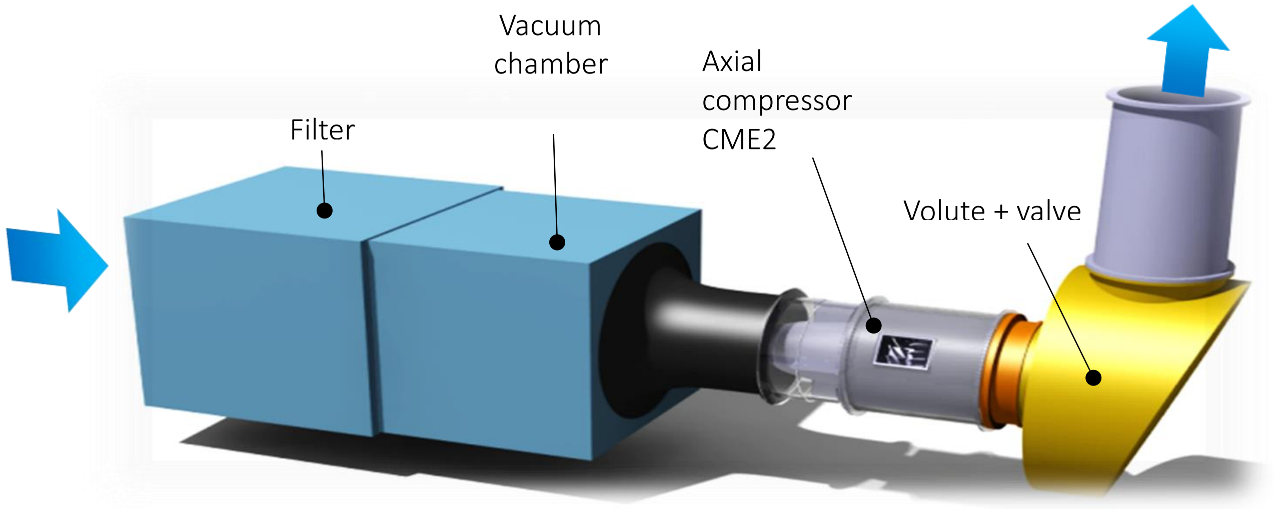

Figure 3-1 Test rig AX-200 and axial compressor CME2

Electric motor	
Brand	ABB
Model	HXR 315L 2B E
Nominal power	200 kW
Supply voltage	380V
Supply frequency	50Hz
Nominal speed	3000 rpm

Speed regulator	
Brand	ABB
Model	SAMISTAR 250F380
Nominal power	200 kW
Supply voltage	380 V
Electrical current	380 A

Mechanical reducer	
Brand	CMD-Unité Messian
Model	HOH 0.9
Supply power	200 kW
Maximum speed	7034.48 rpm
Minimum speed	3000 rpm

Table 3.1 – Features of the electric motor, speed regulator and the mechanical reducer

The electric motor is connected to the compressor shaft with a mechanical reducer of 2.345 ratio.

The upstream air is micro-filtered with a SOFILTRA POELMAN filter before being conveyed in a plenum chamber, connected to the compressor sunction by a convergent, in order to have a flow as uniform as possible.

The flow rate is regulated downstream of the circuit, reducing the outlet section of the volute, by means of a throttling valve motorised with a LEROY SOMER system of 0.25 kW nominal power (motor MFA63M, reducer VR60 HG).

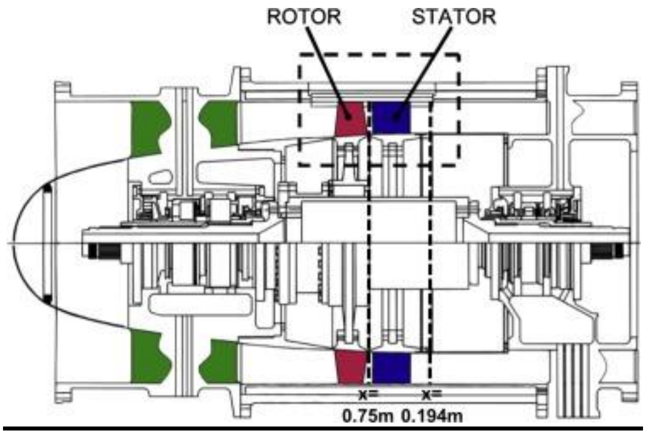

Figure 3-2 Longitudinal section of the compressor CME2

A longitudinal section of the compressor CME2 is shown in Figure 3.2. The compression stage is composed of 30 blades for the rotor and 40 blades for the stator. Their respective specifications are showed in Table 3.2 and Table 3.3.

	Chord [mm]	Thickness [mm]	Pitch angle [°]	End angle [°]
Hub	84	7,9	33,5	41,5
Mid height	84	5,6	46	23
Case	84	2,8	54	20

Table 3.2 – Geometric data of the rotor blades

	Chord [mm]	Thickness [mm]	Pitch angle [°]	End angle [°]
Hub	77	6,2	17,5	46,5
Mid height	77	6,2	15	41,5
Case	77	6,2	12,5	36

Table 3.3 – Geometric data of the stator blades

The rotor blade height decreases along the mean camber line, due to the divergent shape of the hub, from a radius of 207 mm to 214 mm, in order to maintain the tip clearance constant and equal to 0.5 mm; then the hub radius value remains unvaried, as the stator blade height, until the end stage. No flow guide device is installed in the sunction side to control the flow path, hence, the fluid has not any pre-forced rotation speed while is important to highlight a possible perturbation due to the presence of a cross structure, ahead the hub, for sturdiness reason.

Table 3.AA shows the design inlet condition, p=101325 Pa; T= 15 °C

Speed rotation	6330 rpm
Mass flow rate	10.5 Kg/s
Total to total pressure ratio	1.15
Rotor tip speed	181 m/s
Tip Mach number	0.56
Tip Reynold number	$1.06*10^6$
Rotor inlet axial speed	82 m/s

Table 3.4 – Design point inlet condition values of the compressor

As it can be seen in Figure 3.1, an opening is carved in the casing, starting just upstream the stator blade row, in order to install a custom plate replacement with several holes fitted for holding the pressure probes. Figure 3.3, Figure 3.4. There are 7 holes displaced in 14 rows circumferentially spaced every 2 degrees and axially spaced every 6 mm for a total of 98 slots. This equipment allows to cover the stator case area with a very dense matrix of possible observation points.

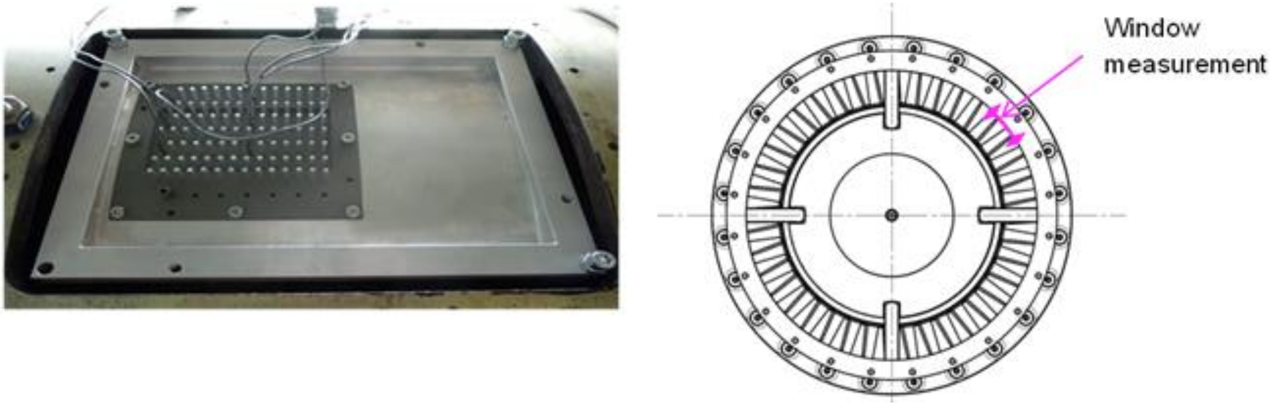

Figure 3-3 Supporting probes aluminium structure and its circumferential position in the casing

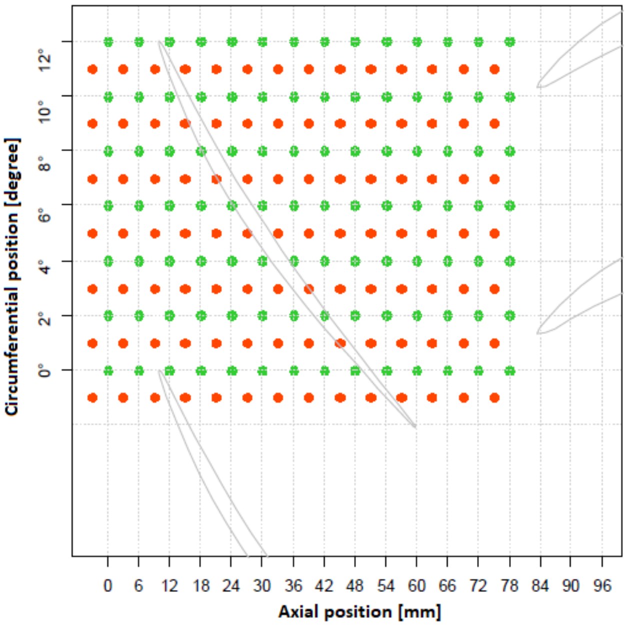

Figure 3-4 Matrix arrangement for the measurement tools

Finally, the pressure probes utilized were ENDEVCO 8507C-1 (-2) together with an amplifier DC ENDEVCO 136. Features of the devices are shown in Table 3.5.

Pressure Transducers Features

ENDEVCO 8507C-1/2	
Technology	Piezo-resistive
Pressure range	0-6700 Pa
Sensitivity	0.029 mV/Pa
Resonance frequency	55000 Hz
Number	25

Table 3.5 – Pressure probe featur

4. STABLE CONDITION: REFERENCE PRESSURE-WAVE

4.1 INTRODUCTION

The purpose of this introduction is to give primarily information about the machine performance, usage and data collected and utilized. Figure 4.1 provides a rough illustration of the performance curve of the compressor at 3200 rpm, expressed using the static pressure increment between stage inlet and outlet sections. The nominal rotation speed is 6330 rpm but it was reduced to 3200 rpm in order to increase the probes sampling relative acquisition rate compared to frequency phenomena occurring in the air flow. It can be noticed that there are two marked points of the curve:

- Qn design flow rate
- Qc critical flow rate for the rotating stall inception

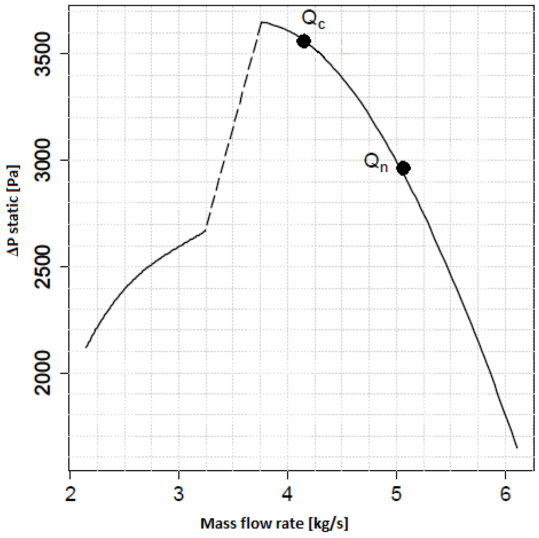

Figure 4-1 Machine performances in the investigated operational points

To compare the velocity triangles at the two different rotation speed, Veglio (Veglio M., 2015) analysed Reynolds and the Mach numbers. Two different Reynold numbers, referred to the blade tip, were taken in to account for each speed: $Re_{U1} = \frac{R_2 U_1}{\nu}$ is calculated using the external radius R_2 with a corresponding speed U_1; $Re_{W1} = \frac{c\,W_1}{\nu}$, which is more representative of the flow state around blades, is calculated using the blade chord c and the relative speed W_1 entering the blade array.

	6330 rpm			3200 rpm		
	Speed	Length	Re	Speed	Length	Re
Re_{U1}	U_1 = 182 m/s	275 mm	$3.4 * 10^6$	U_1 = 94 m/s	275mm	$1.7 * 10^6$
Re_{W1}	W_1 = 200 m/s	84 mm	$1.1 * 10^6$	W_1 = 100 m/s	84 mm	$5.6 * 10^5$

Table 4.1 – Speed, length and Reynolds numbers associated to the rotation speed ω_{rot} = 6330 rpm and ω_{rot} = 3200 rpm

All Reynolds numbers are approximately 10^6 of magnitude order thus their variation is probably unaffected and could be neglected.

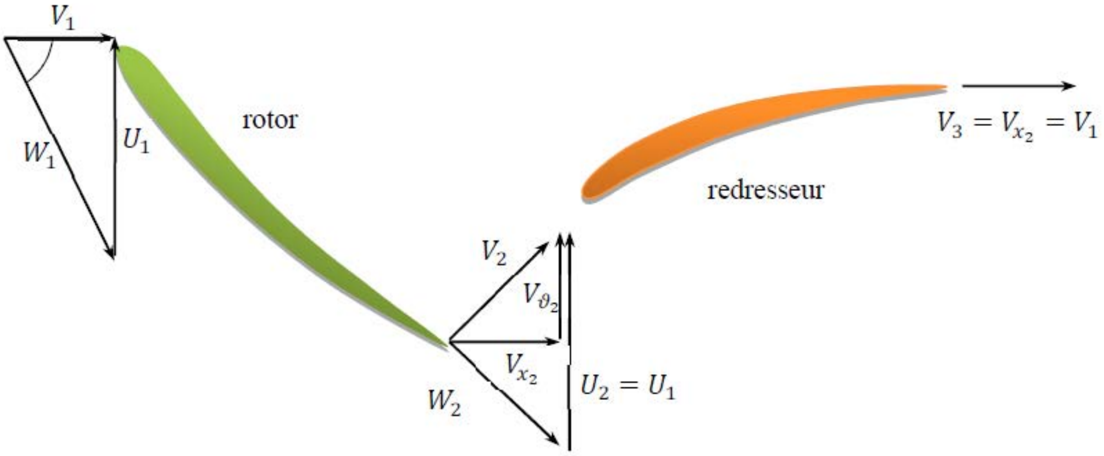

Figure 4-2 Velocity triangles in a compression stage at design condition

To investigate the compressible effect, different Mach numbers, still referred to the blade tip where the velocities are the greatest, are showed in Table 4.2. It can be seen that all Mach numbers at 3200 rpm have a value smaller than 0.3 hence the compressible effects are neglected whilst it cannot be done the same for 6330 case. These differences were considered in any case moderate.

	6330 rpm		3200 rpm	
	Speed	Mach	Speed	Mach
V_1	82	0.25	41	0.12
W_1	200	0.6	100	0.3
U_1	182	0.55	92	0.28
V_1	117	0.35	61	0.19
W_1	128	0.39	60	0.2

Table 4.2 – Speed and Mach numbers associated to the rotation speed ω_{rot} = 6330 rpm and ω_{rot} = 3200 rpm

Finally, in order to have the compressor working in condition as close as possible between the two rotation speeds, and find the correct position for Qn and Qc at slow speed, the values of the 2 flow rates are calculated using the non-dimensional flow number:

$$\delta = \frac{q_m}{\omega_{rot} R^3}$$

Table 4.3 contains all the flow rate values.

	Qn [Kg/s]	Qc [Kg/s]
6300 rpm	10.5	8.75
3200 rpm	5.3	4.33

Table 4.3 – Similitude criterion adopted between the mass flow rates at the rotation speed ω_{rot} = 6330 rpm and ω_{rot} = 3200 rpm

It’s important to remind that these values are defined for standard temperature and pressure values measured in the vacuum chamber situated upstream the compressor. These values are:

$$p_{01} = 101325\, Pa \qquad T_{01} = 288\, K$$

If the upstream air conditions are not the standard ones, as always happens, the working parameters are adjusted using the reduced values:

Reduced speed = $\frac{\omega_{rot}}{\sqrt{T_{01}}}$

Reduced flow rate = $\frac{q_m\sqrt{T_{01}}}{p_{01}}$

In this chapter the methodology adopted to perform the analysis is explained. Referring to Figure 4.1, the data available to perform the task were:

- A series of data collected at the **design point** (Qn) for each possible probe position.
  Sampling frequency: 35000 Hz
  Sampling time: 60 s

- A series of data collected at the **last stable point for the rotating stall inception** (Qc) for each possible probe position.
  Sampling frequency: 35000 Hz
  Sampling time: 60 s

- A series of data collected starting from the last stable point Qc, decreasing the mass flow rate at constant speed until the rotating stall inception.
  Sampling frequency: 50000 Hz
  Sampling time: 10 s

- A series of data collected starting from a condition of rotating stall fully developed, increasing the mass flow rate at constant speed until the design point condition.
  Sampling frequency: 100000 Hz
  Sampling time: 30 s

It's important to highlight that the first 2 acquisitions have a total of 35000 Hz * 60 s = 2100000 points acquired while the third one has 50000 Hz *10 s = 500000 points.

The goal of this work is to possibly find an easy, reliable and cheap method able to give information about the time lapse preceding the stall inception. After several attempts we came up with the following procedure. For each possible axial location, a frequency analysis in of the compressor pressure waves in design condition was performed. Then the main frequencies obtained were used to build a first reference function to be convolved with the previous data in order to attain an accurate mean pressure wave function. After some iteration, this reference function will be utilized in unsteady condition to identify some parameters forecasting the stall inception.

4.2 FREQUENCY ANALYSIS

As explained in the previous paragraph, the first step taken is to perform a spectral analysis in order to find the most important frequency and their energy level. Figure 4.3 shows the pressure locations interested. As it can be observed, the total axial space is investigated from approximately 12 mm before the leading edge to 18 mm beyond the trailing edge.

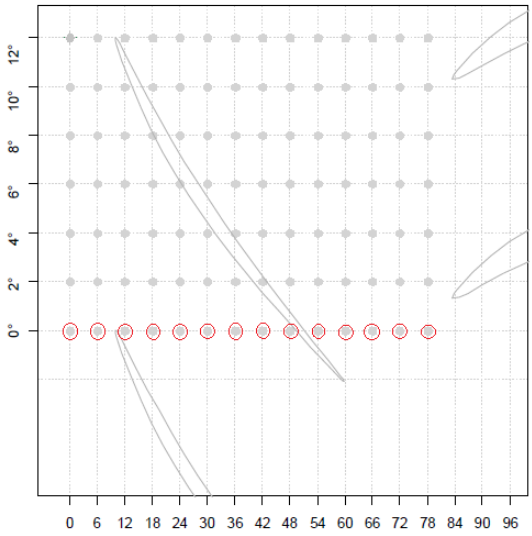

Figure 4-3 Probes disposition for the pressure signal acquisition

The frequency analysis is carried out by using the version of the Fourier Transform adapted for a series of discrete values called Fast Fourier Transform (FFT). This kind of tool gives general information about the presence of periodic phenomena and their amplitude as well. Figure 4.4 to 4.19 are composed of two sketches, one for each axial position as described before. The left image is a 100 points sample of the pressure probe signal during the time. It is shown, just for reference, to see how the shape of the pressure wave of each location looks like. The signal is treated removing the mean value of the whole sample: this operation is necessary to remove the energy associated to the 0 frequency. The right image, instead, is the frequency spectrum associated. It's important to underline that the analysis was not performed in the most rigorous way because high precision wasn't required. To minimize the leakage problem no filter was applied but only a careful choice of the window treated. This is possible thanks to the dense rate acquisition that allows to pick an almost complete signal, multiple of 2π, to be analysed.

The most important achievement of the spectral analysis is the unambiguous determination of the blade frequency passage which slightly oscillates around 1610 Hz. This lead the consideration that blade passage period is:

$$T_{blade} = \frac{1}{f} = \frac{1}{1610} = 6.21 * 10^{-4} \text{ seconds}$$

This value multiplied by the acquisition frequency leads to the other precious information, employed a lot in the algorithm scripts, that every blade passage is discretized by an average of 21.73 points.

4.2.1 DESIGN POINT FLOW RATE Qn

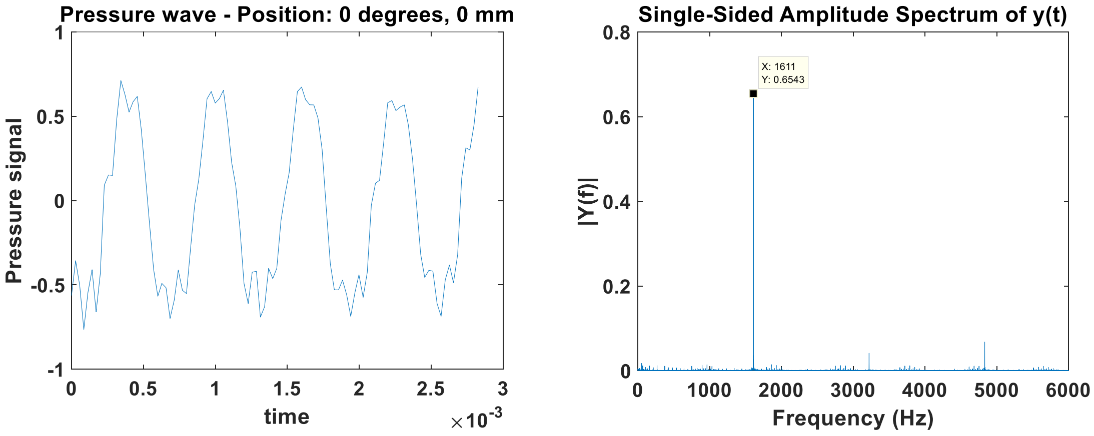

Figure 4-4 Pressure signal and Fourier transform, nominal flow rate, slot 0°-0mm

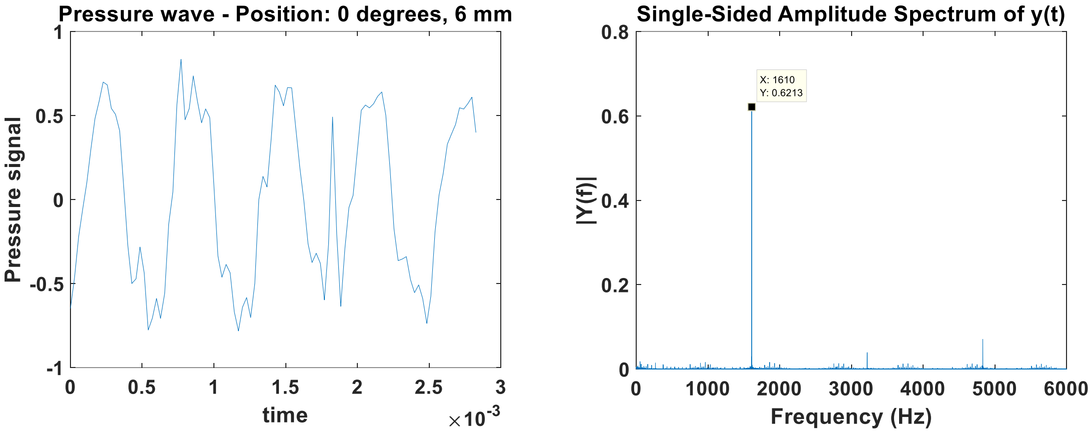

Figure 4-5 Pressure signal and Fourier transform, nominal flow rate, slot 0°-6mm

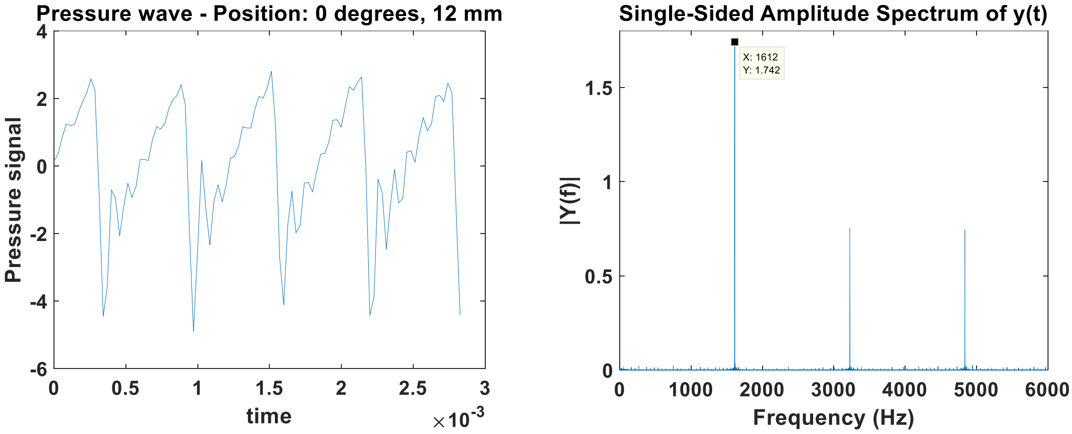

Figure 4-6 Pressure signal and Fourier transform, nominal flow rate, slot 0°-12mm

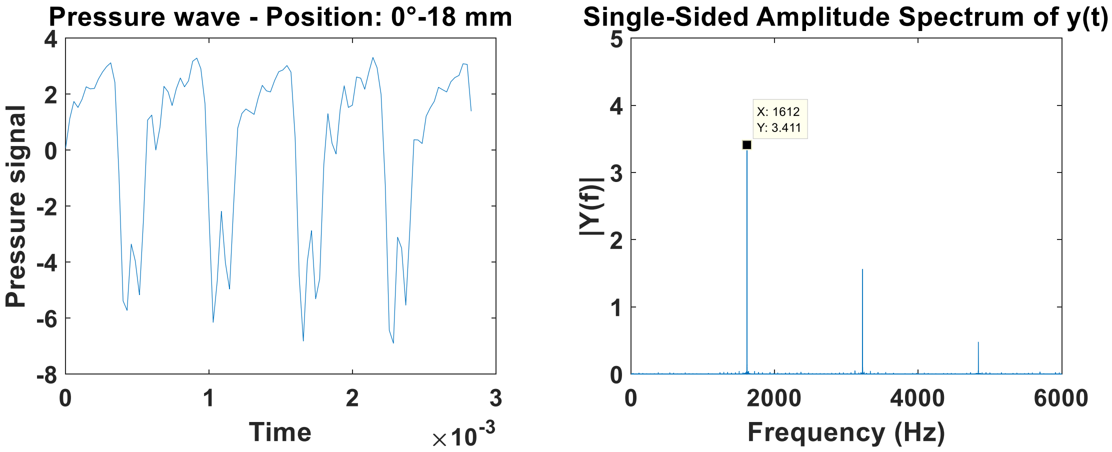

Figure 4-7 Pressure signal and Fourier transform, nominal flow rate, slot 0°-18mm

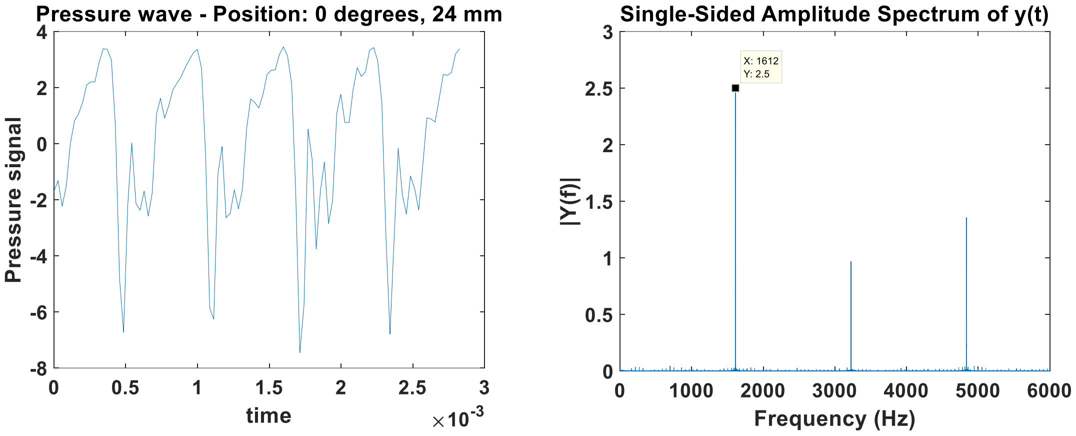

Figure 4-8 Pressure signal and Fourier transform, nominal flow rate, slot 0°-24mm

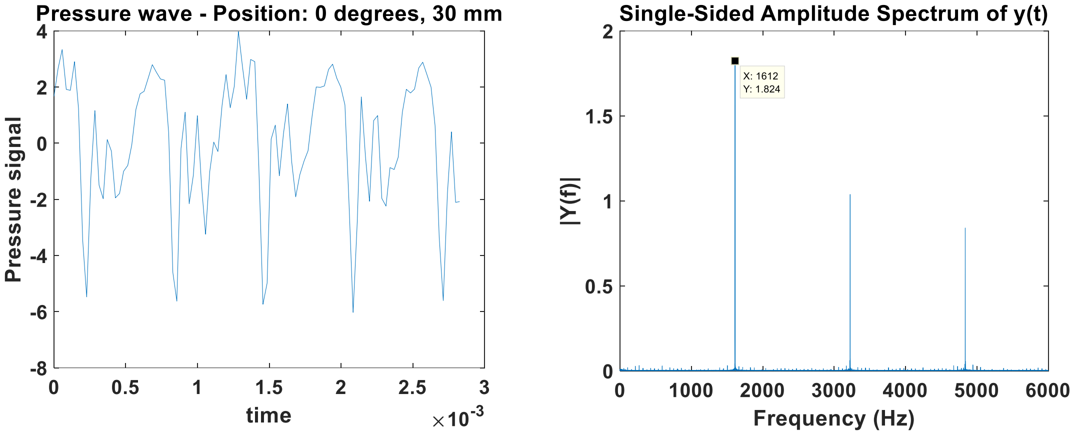

Figure 4-9 Pressure signal and Fourier transform, nominal flow rate, slot 0°-30mm

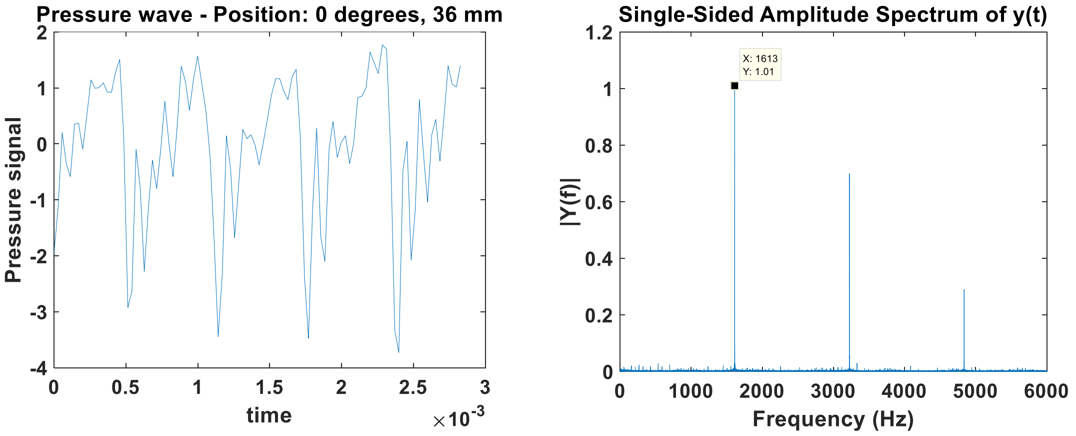

Figure 4-10Pressure signal and Fourier transform, nominal flow rate, slot 0°-36mm

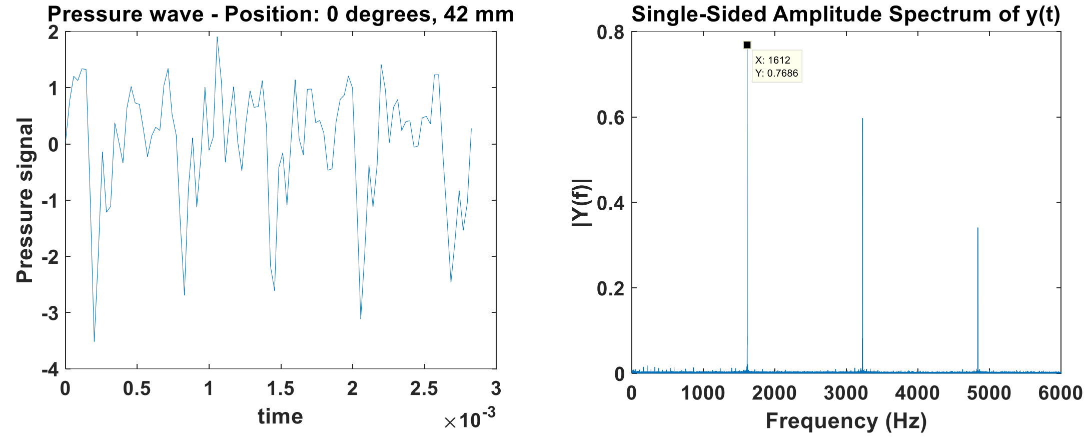

Figure 4-11 Pressure signal and Fourier transform, nominal flow rate, slot 0°-42mm

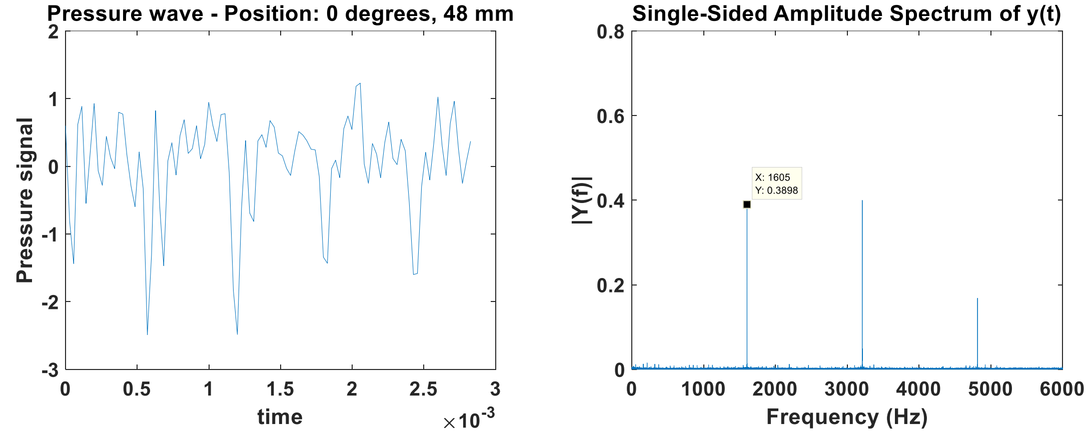

Figure 4-12 Pressure signal and Fourier transform, nominal flow rate, slot 0°-48mm

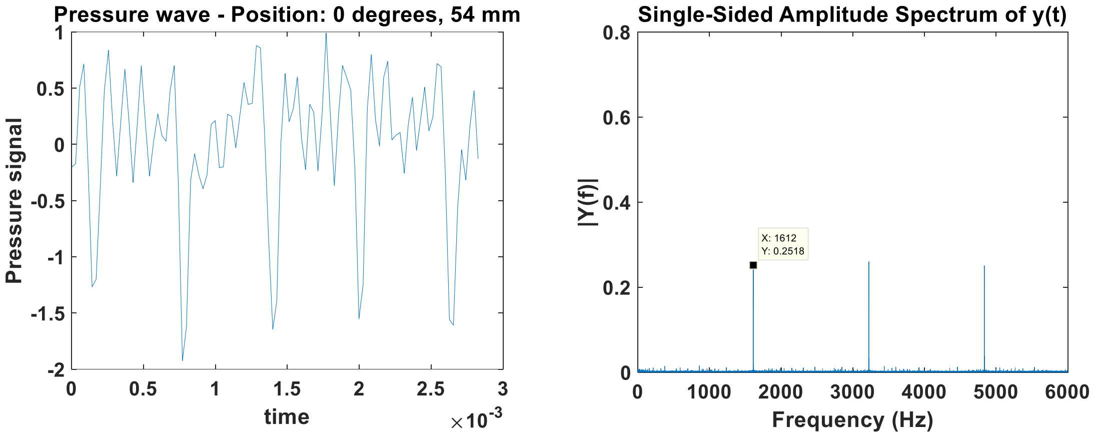

Figure 4-13 Pressure signal and Fourier transform, nominal flow rate, slot 0°-54mm

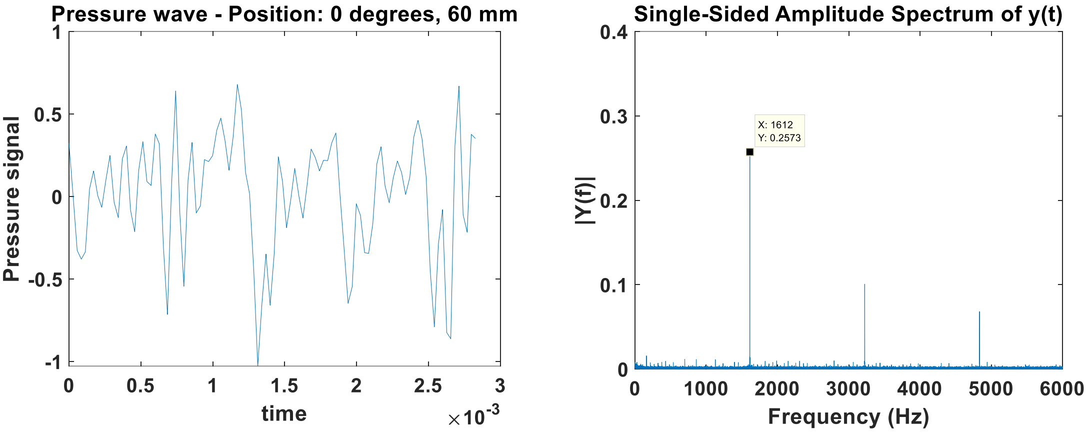

Figure 4-14 Pressure signal and Fourier transform, nominal flow rate, slot 0°-60mm

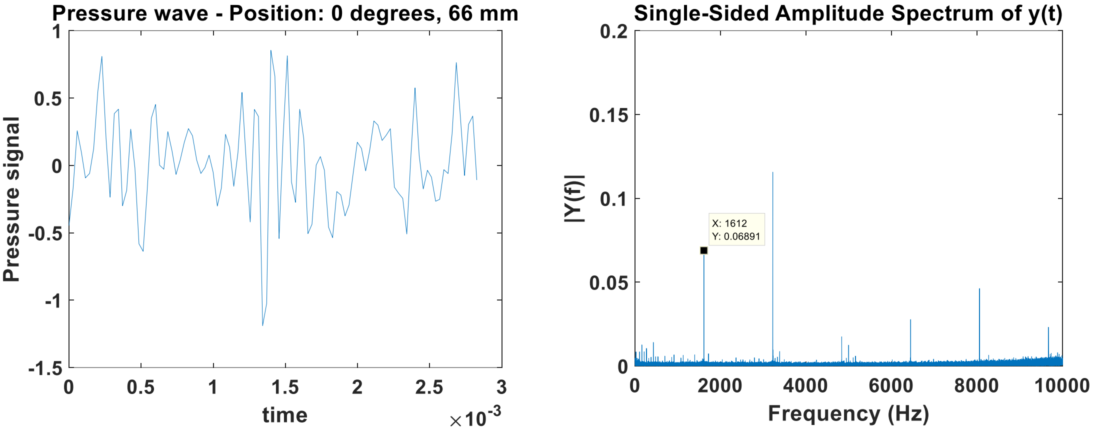

Figure 4-15 Pressure signal and Fourier transform, nominal flow rate, slot 0°-66mm

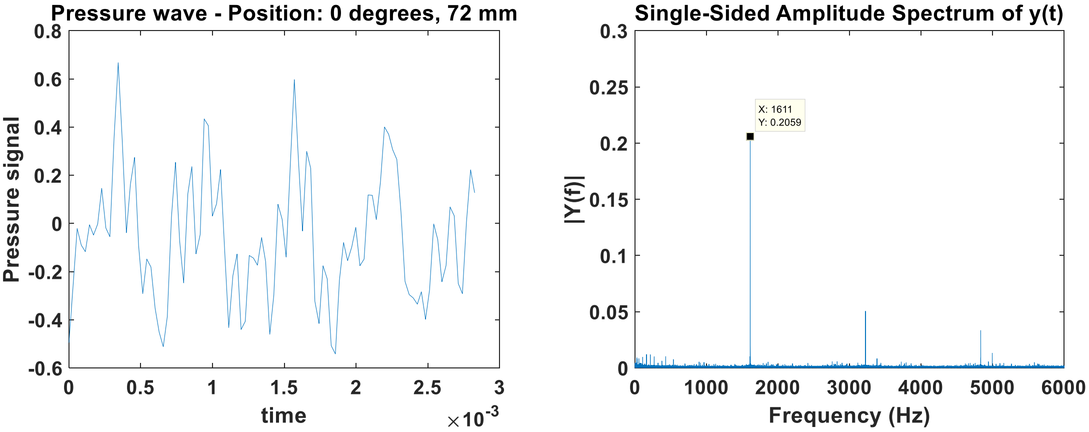

Figure 4-16 Pressure signal and Fourier transform, nominal flow rate, slot 0°-72mm

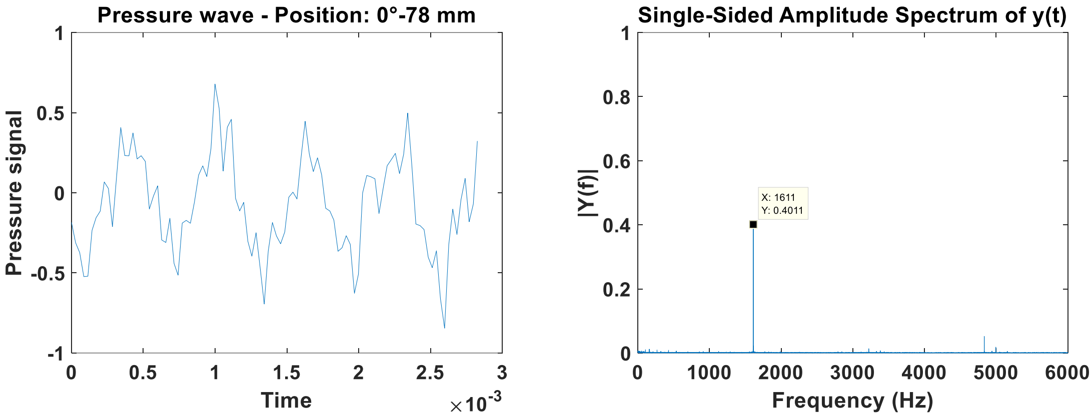

Figure 4-17 Pressure signal and Fourier transform, nominal flow rate, slot 0°-78mm

Having to deal with a huge amount of data, it’s interesting to describe the energy transfer behaviour during a blade passage to focus the efforts and limit the investigation field. Figure 4.20 depicts the average pressure level rise along the inter-blades channel together with the pressure fluctuation embodied by the standard deviation (In Figure 4.20 error bars represent only 25% of the true value for scale size difficulties). The image shows how the energy is transferred to the fluid along the blade chord passing from -1300 Pa at the inlet section to 1700 Pa at the outlet one before the stator leading edge. The pressure rise distribution is not homogeneous but I can be divided in three sectors with different behaviour. The central sector covers approximately 60% of the chord axial projection and it’s where the 80% of the total pressure rise is achieved. The leading part contributes for a 5% while the trailing part for 15%. At the same time standard deviation is the greatest in the central sector, with a maximum for the axial position at 18 mm, while it’s the lowest in the first and last sector. The only dissimilar behaviour is observed at the axial position of 12 mm where the fluctuation is very despite its position in the first sector. This is due to the presence of the of the blade tip leakage starting approximately in this position.

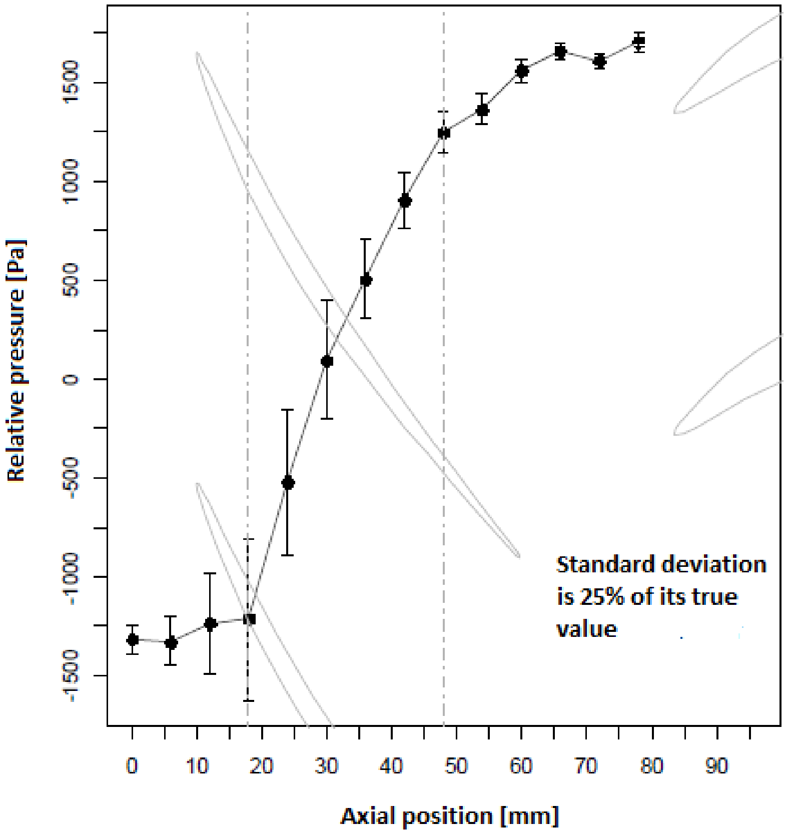

Standard deviation is 25% of its true value

Figure 4-18 Axial profile of the mean pressure in the clearance between two blades, nominal flow rate

4.2.2 CRITICAL FLOW RATE Qc

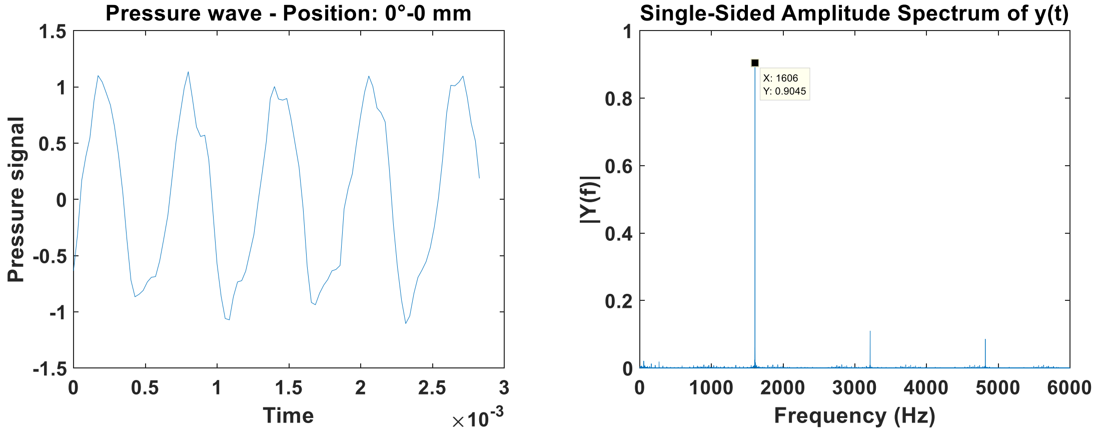

Figure 4-19 Pressure signal and Fourier transform, critical flow rate, slot 0°-0mm

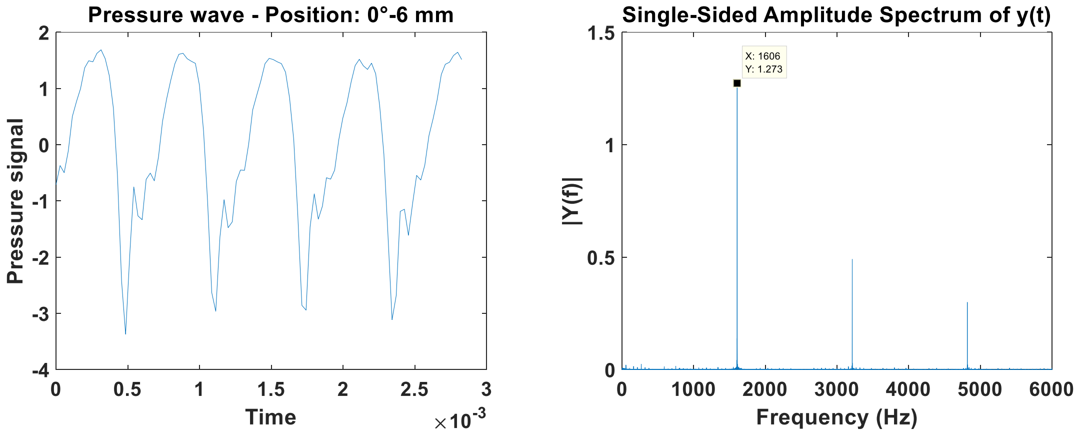

Figure 4-20 Pressure signal and Fourier transform, critical flow rate, slot 0°-6mm

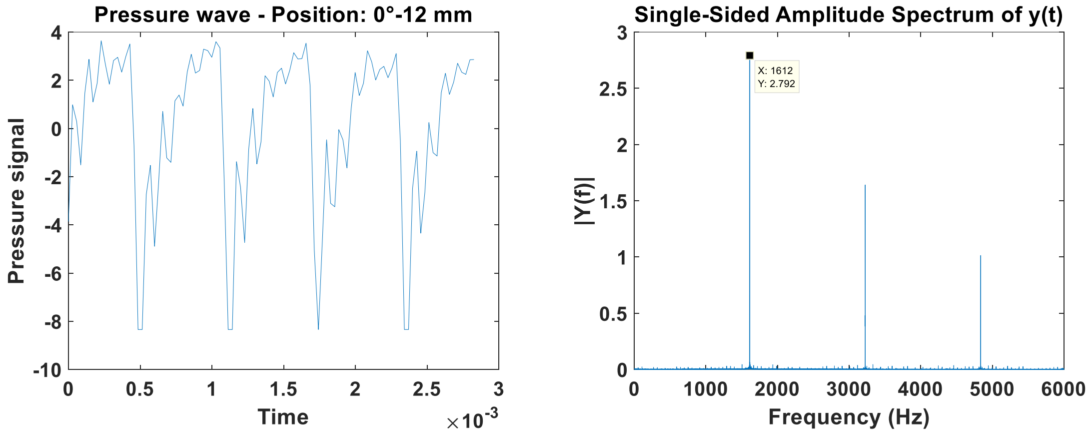

Figure 4-21 Pressure signal and Fourier transform, critical flow rate, slot 0°-12mm

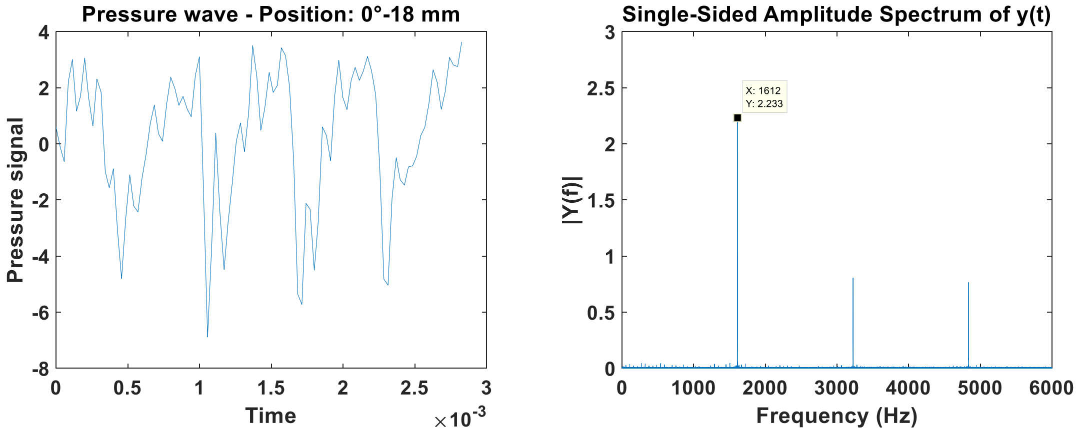

Figure 4-22 Pressure signal and Fourier transform, critical flow rate, slot 0°-18mm

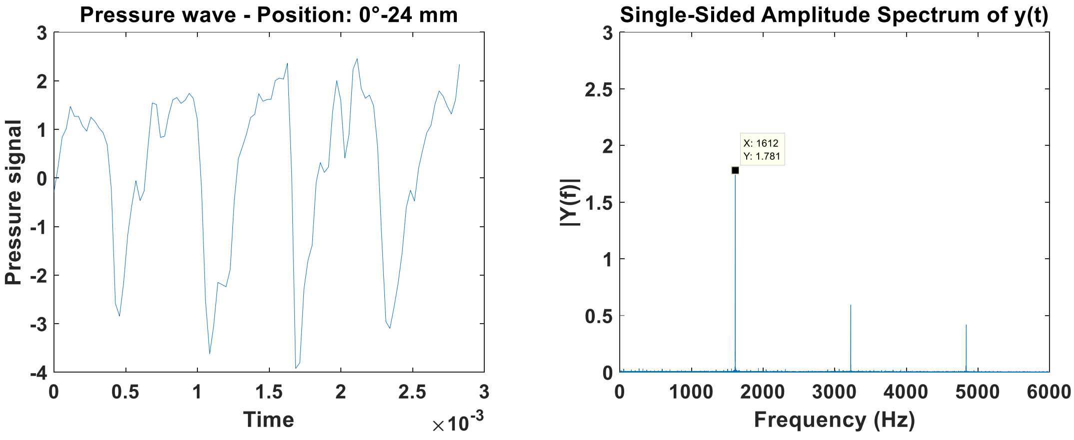

Figure 4-23 Pressure signal and Fourier transform, critical flow rate, slot 0°-24mm

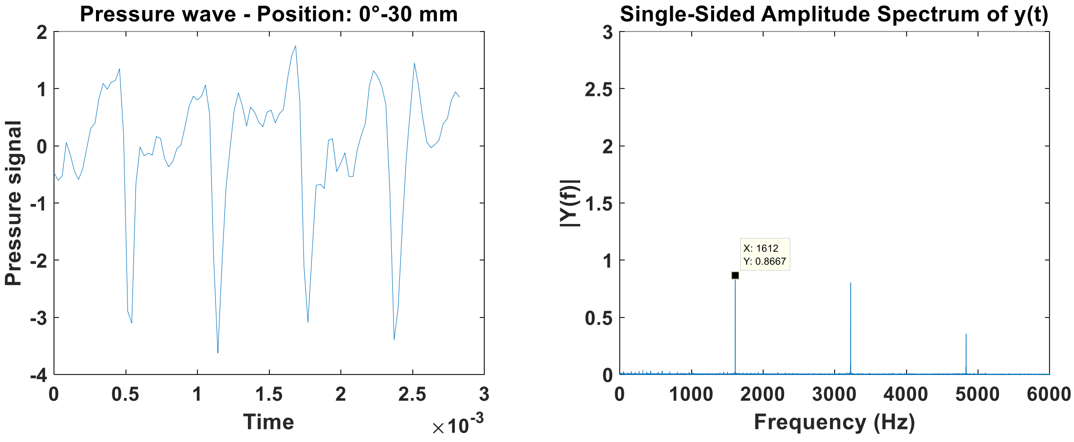

Figure 4-24 Pressure signal and Fourier transform, critical flow rate, slot 0°-30mm

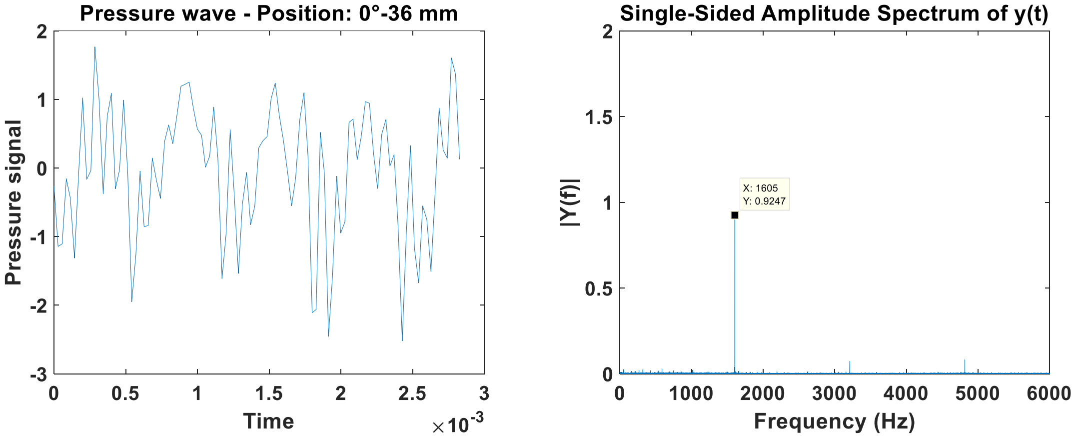

Figure 4-25 Pressure signal and Fourier transform, critical flow rate, slot 0°-36mm

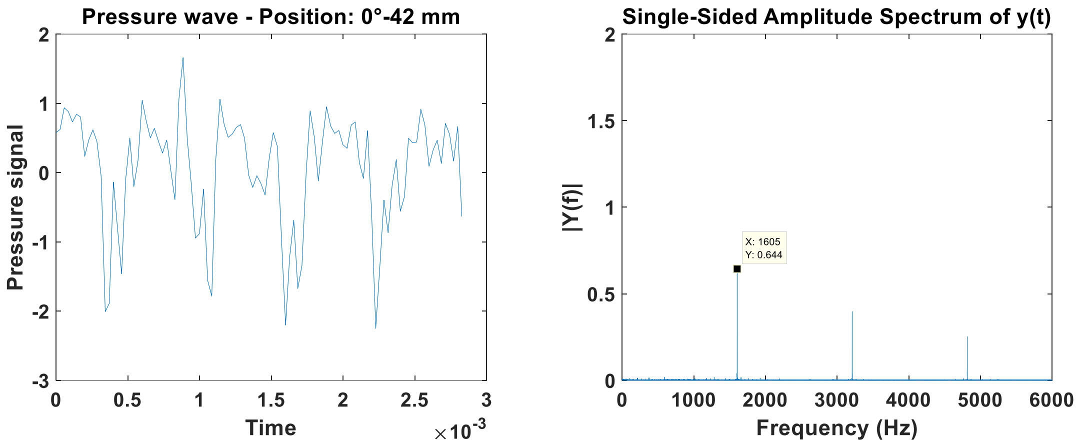

Figure 4-26 Pressure signal and Fourier transform, critical flow rate, slot 0°-42mm

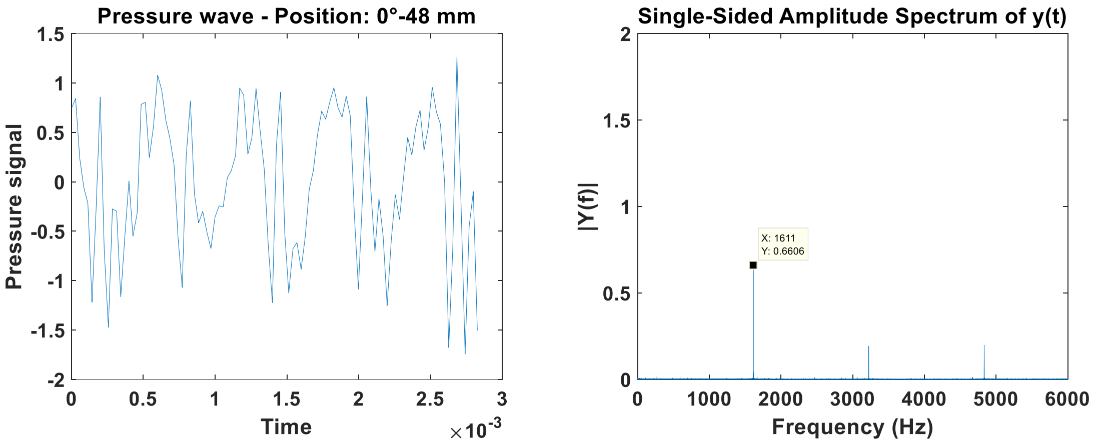

Figure 4-27 Pressure signal and Fourier transform, critical flow rate, slot 0°-48mm

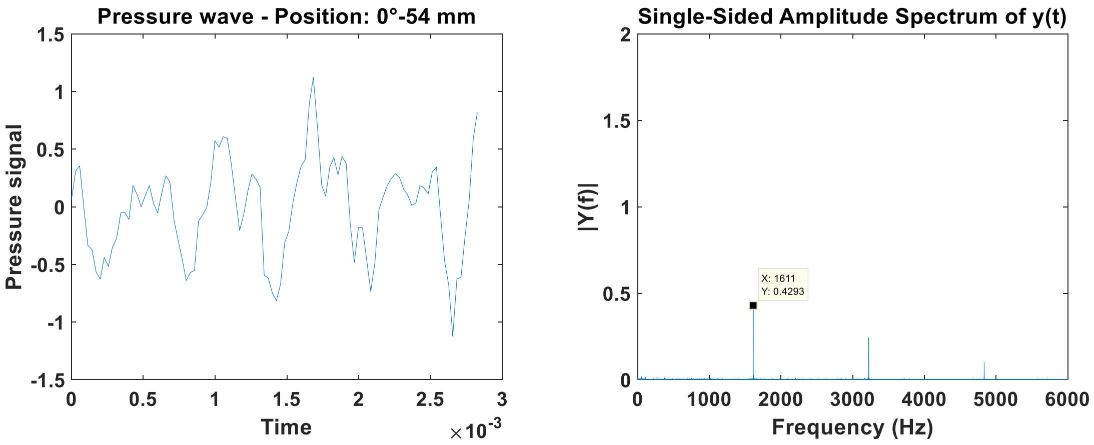

Figure 4-28 Pressure signal and Fourier transform, critical flow rate, slot 0°-54mm

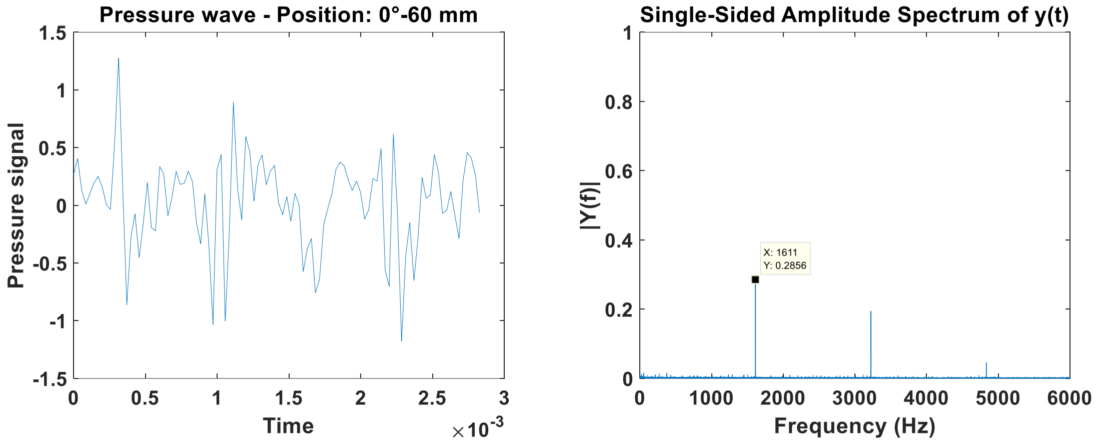

Figure 4-29 Pressure signal and Fourier transform, critical flow rate, slot 0°-60mm

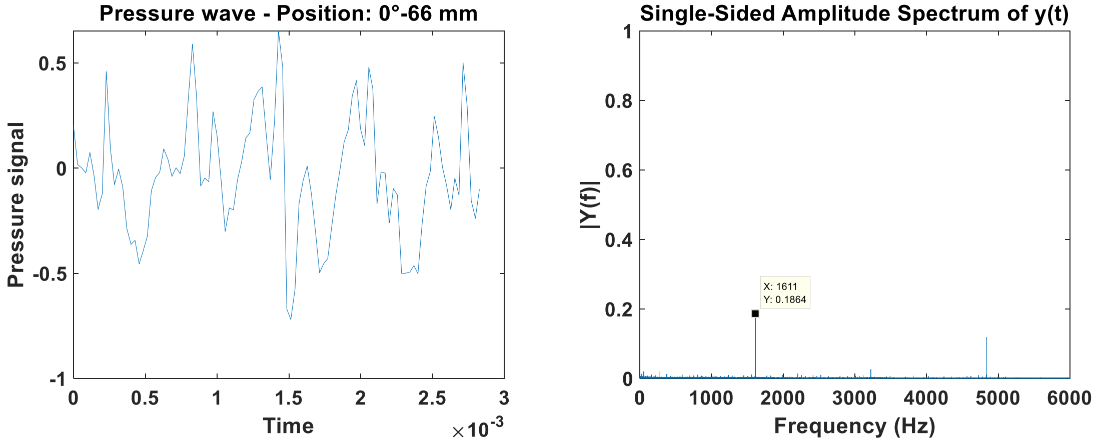

Figure 4-30 Pressure signal and Fourier transform, critical flow rate, slot 0°-66mm

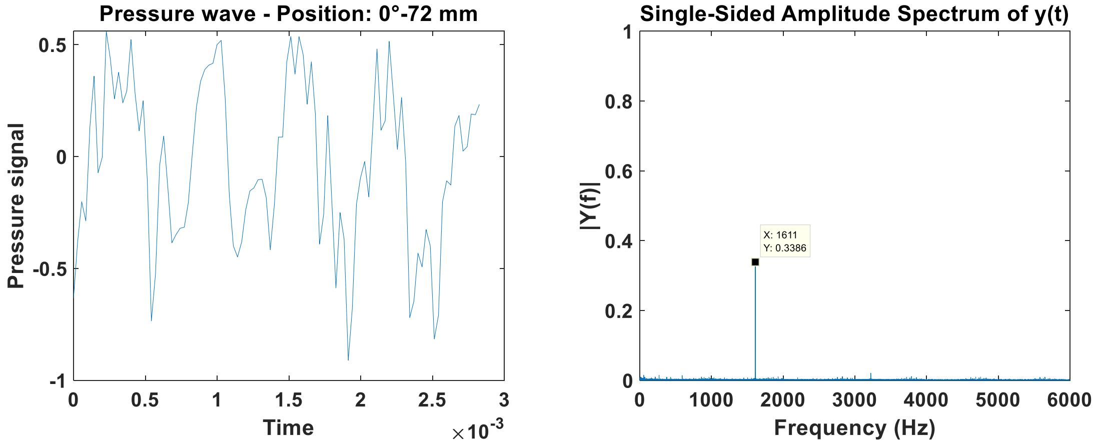

Figure 4-31 Pressure signal and Fourier transform, critical flow rate, slot 0°-72mm

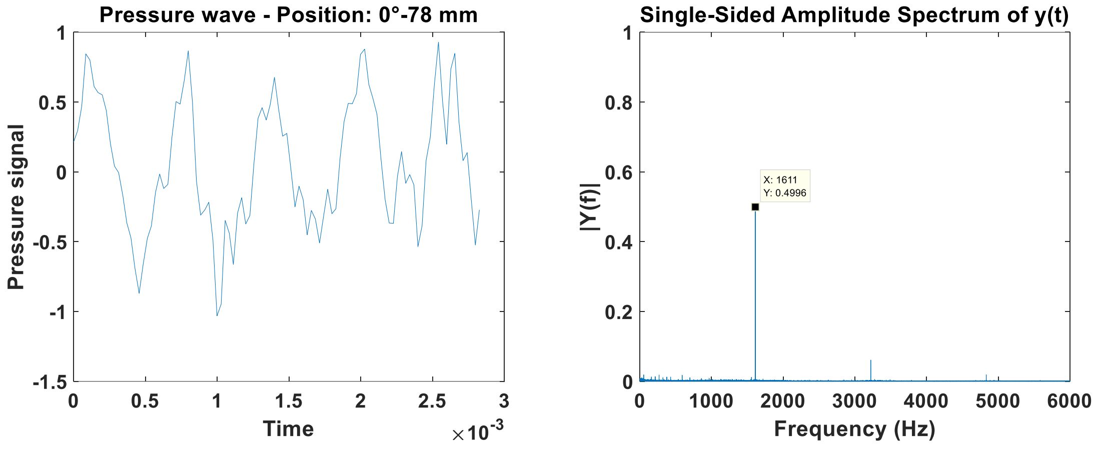

Figure 4-32 Pressure signal and Fourier transform, critical flow rate, slot 0°-78mm

Figure 4.20 depicts the average pressure level rise along the inter-blades channel together with the pressure fluctuation embodied by the standard deviation (In Figure 4.20 error bars represent only 25% of the true value for scale size difficulties). The image shows how the energy is transferred to the fluid along the blade chord passing from -700 Pa at the inlet section to 2500 Pa at the outlet one before the stator leading edge. As for the nominal flow rate, pressure rise distribution is not homogeneous but it can be divided in three sectors with different behaviour with the same energy additions.

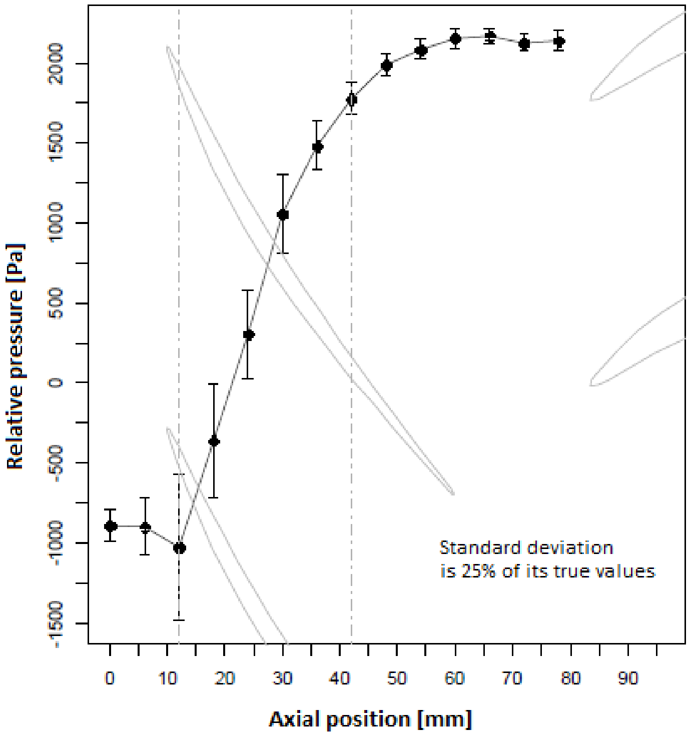

Figure 4-33 Axial profile of the mean pressure in the clearance between two blades, critical flow rate

4.3 REFERENCE FUNCTION CONSTRUCTION

The purpose of this paragraph is to give an outline of the procedure used to build a reference function. With the term “reference function” is indicated the construction of the average pressure evolution produced by a blade passage i.e. a time frame of $6.21 * 10^{-4}$ seconds. Moreover, this approach permits to have a more detailed density of pressure values as the measurements had been collected at higher frequency. Finally, for each average time-pressure signal pair of values obtained, the standard deviation is calculated in order to quantify the fluctuation.

The procedure consists of the following steps:

1. FIRST PERIODIC FUNCTION SELECTION

   Making use of the information given by the FFT, a first attempt function is built. For example: probe positioned in the slot 0 degrees – 0 mm (Figure 4.4) is characterized by a main frequency of 1606 Hz and an energy content of about 0.9045, a second frequency of 3213 with an energy content of 0.11 and a third frequency of 4819 with an energy content of 0.086 which give information about the periodic pulsation and amplitude. The extrapolated function could be:

   ```
   First_attemp_function =
   0.9045*cos(2*pi*1606*t_ref+pi)+0.11*cos(2*pi*3213*t_ref+pi/3)+0.086*cos(2*pi*4819*t_ref-pi/2);
   ```

   Where *f* is 1606 Hz and *time* is a vector that discretizes time in equally spaced step from 0 to $6.21 * 10^{-4}$ seconds. Figure 4.34 shows an overlap between measured values and this first periodic function. As it can be seen, the match is very accurate.

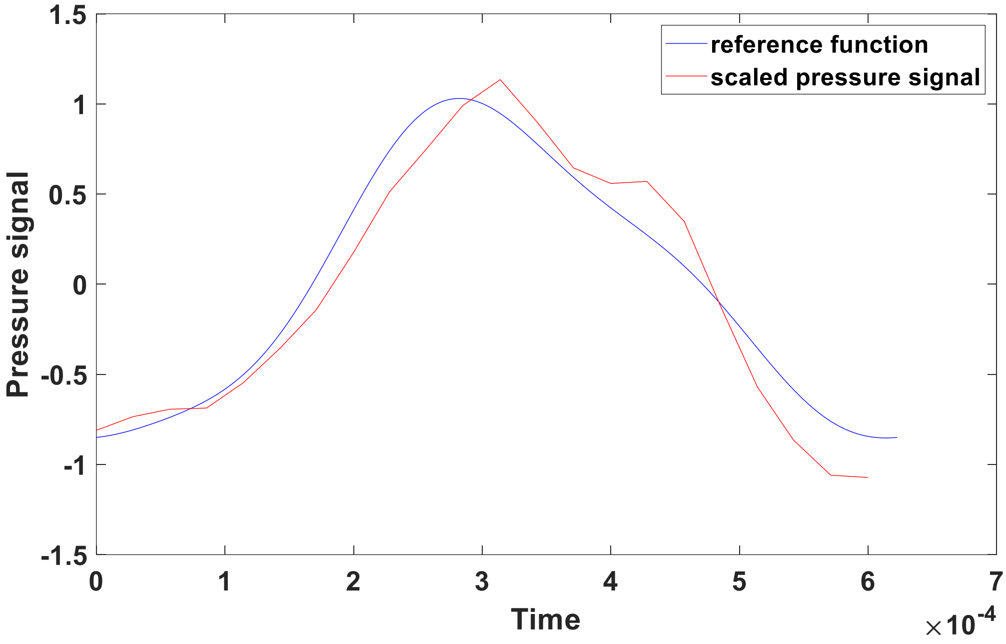

Figure 4-34 Reference function and scaled pressure signal overlap

2. LINEAR INTERPOLATION

Figure 4.35 shows how the collected data and the chosen first reference function both experience a linear interpolation increasing the resolution by more than 10 times passing from about 22 points per time period to 220.

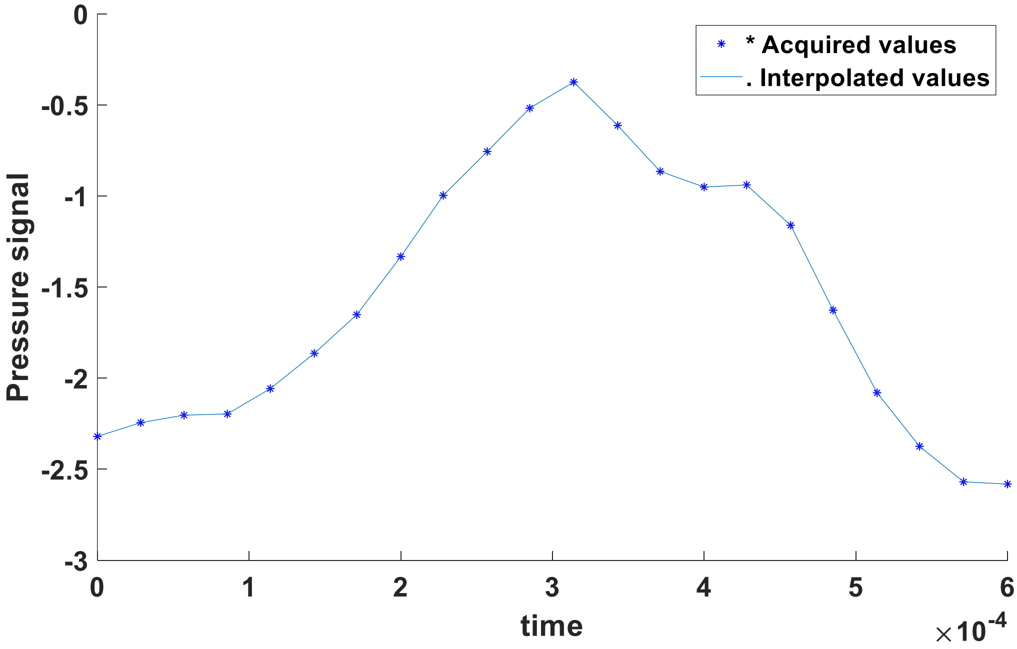

Figure 4-34 Linear interpolation of a pressure signal

3. MOVING AVERAGE FILTER

   In order to have a smother and realistic curve a moving average filter is applied to all interpolated points. This filter has to be set to a certain value (3 in our case) and it calculates, for each point of interested, the average value among the selected point, the previous 3 and the following 3. Figure 4.35 shows the results.

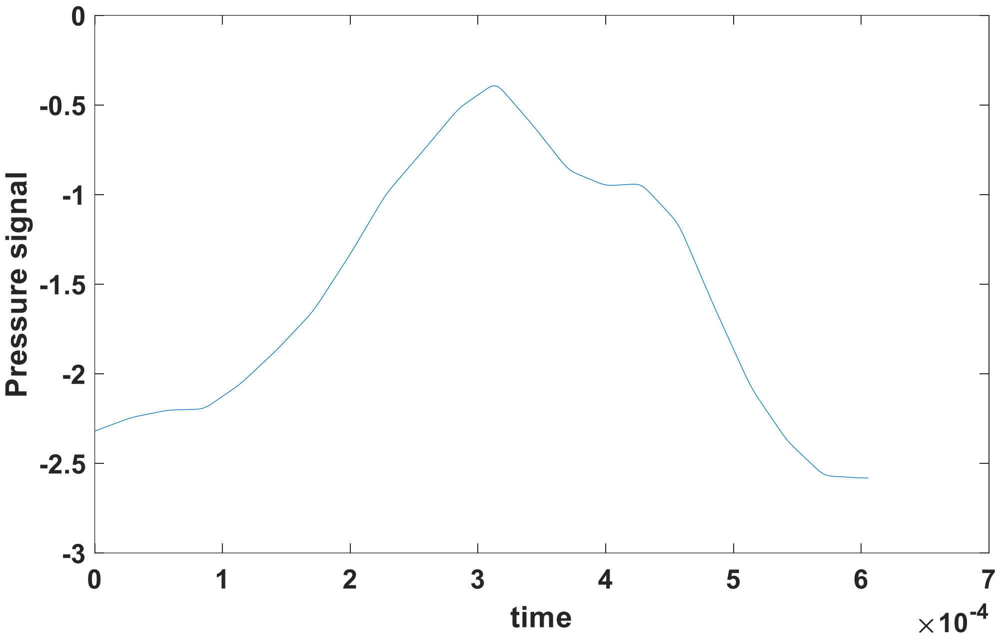

Figure 4-35 Smooth filter applied on a pressure signal

4. CONVOLUTION

   Convolution is a mathematical operation on two function that creates a third one. It is similar to cross-correlation and, for discrete real valued function, they only differ in time reversal in one of the functions. It is defined as the integral of the product of the two functions after one is reversed and shifted.:

$$(f * g)(t) \overset{\text{def}}{=} \int_{-\infty}^{\infty} f(\tau)\, g(t-\tau)d\tau = \int_{-\infty}^{\infty} f(t-\tau)g\,(\tau)d\tau$$

For complex-valued functions *f*, *g*, the discrete convolution of *f* and *g* is given by:

$$(f * g)[n] = \sum_{m=-\infty}^{\infty} f[m]\, g[n-m] = \sum_{m=-\infty}^{\infty} f[n-m]\, g[m]$$

Thus, convolution of two vectors, u and v, represents the area of overlap under the points as v slides across u. Algebraically, convolution is the same operation as multiplying polynomials whose coefficients are the elements of u and v.

Let m = length(u) and n = length(v), then w is the vector of length m+n-1 whose kth element is:

$$w(k) = \sum_{j} u(j)\, v(k-j+1)$$

The sum is over all the values of j that lead to legal subscripts for u(j) and v(k-j+1), specifically j = max (1, k+1-n): 1: min (k, m).

When m = n, this gives:

w(1) = u(1)*v(1)
w(2) = u(1)*v(2)+u(2)*v(1)
w(3) = u(1)*v(3)+u(2)*v(2)+u(3)*v(1)
...
w(n) = u(1)*v(n)+u(2)*v(n-1)+ ... +u(n)*v(1)
...
w(2*n-1) = u(n)*v(n)

In our specific case, vector m is a portion of the total collected pressure signal of about $6.21*10^{-4}$ seconds, i.e. 220 points after the linear interpolation, while vector m is the first attempt function created also discretized in the same number of points. Visually it can be seen in Figure 4.36. The first attempt function slide, point by point, from right to left in a selected windows time frame of the pressure signal. At each step, each corresponding point of the former is multiplied by the corresponding ones of the latter giving the value of the w(kth) element. Vector w is then a measure of the area in common of the two curves during each step of the convolution.

The goal of this operation is to reassign a new time value to each pair of points pressure signal/time of the acquired data. The new time values are the ones of the first attempt function that was created using the blade passage as time frame i.e. from 0 to 6.21*10^{-4} with 220 steps equally spaced. The logic behind this procedure is that the best way to rescale time is to assign values that occur when the overlap between the two curves is maximum.

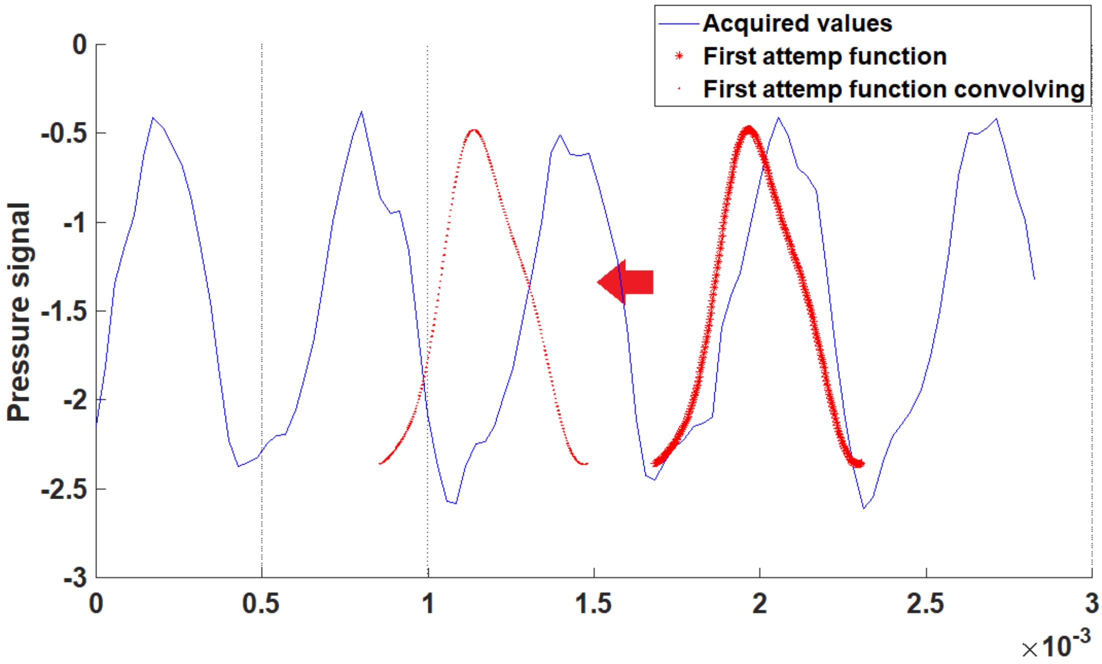

Figure 4-36 Convolution between the first attempt function and the signal pressure

Once the calculation of w is done, we have information about the evolution of the magnitude of area in common the two curves as well as the index number of each one. The length of vector w, as previously described, is equal to m+n-1 = 439. Investigating the index belonging to the maximum convolution value, 3 possible cases can happen:

- The index of maximum value k is 220: in this case the two curves have the maximum overlapped area when the first attempt function is just completely entered in the selected time frame of the pressure signal curve. In this case, and only in this one, each time value of the pressure signal function can be reassigned with the first attempt function time with the same index. The pressure wave is perfectly centred in the window analysed.

- The index of the maximum value k is > 220: in this case the two curves have the maximum overlapped area in the left-half of the windows analysed. Without going in detail of how to reassign time values, it’s important to understand that the left part of the pressure signal curve (the one in correspondence of the first attempt function sliding toward left in the time window) have their time correspondence right, one by one, while the right part of the pressure signal has to be recalculated as a function of k.

- The index of the maximum value k is < 220: in this case the two curves have the maximum overlapped area in the right-half of the windows analysed. Like the previous case, the left part of the pressure signal has to be recalculated as a function of k.

Figure 4.37 illustrates the new pressure signal vector with its 2100000 points rescaled and the first attempt function as well.

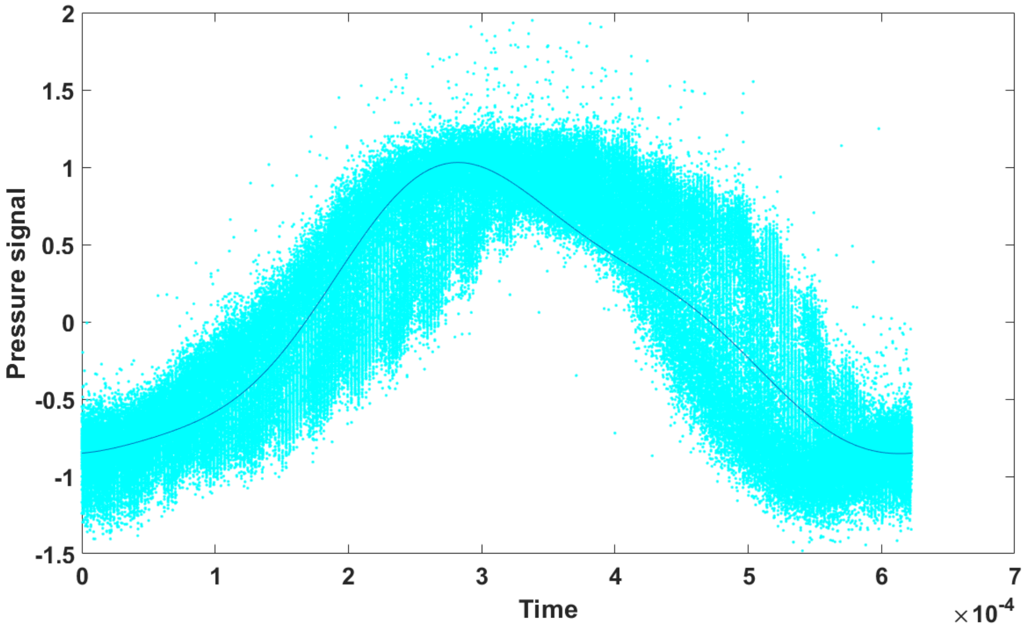

Figure 4-37 Signal pressure point reassigned and overlapped

The final step to obtain a reference function is to divide the blade passage time lapse in parts. For each one, the mean of the pressure values within that part and the standard deviation are calculated. Standard deviation is a measure of the fluctuation but it can also be a warning in case of error in the convolution. We chose to divide the time window in 88 parts to increase the frequency acquisition four times. Figure 4.38 shows the result.

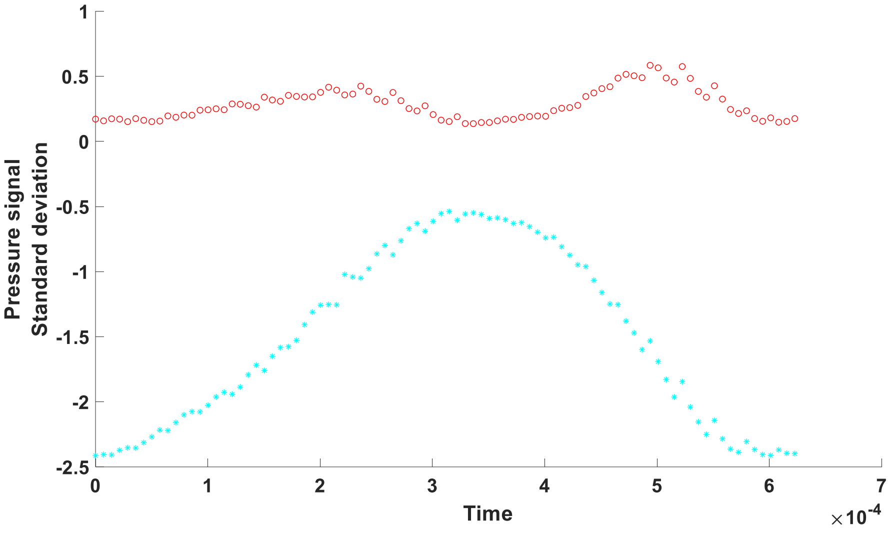

Figure 4-38 First reference function and standard deviation obtained after the first iteration

5. ITERATION

With the new more accurate reference function at disposal we iterate step number 4 several times using this new function obtained in order to increase the result reliability and precision. Figure 4.39 shows the result. As it can be seen, the discrete function is more continuous and cohesive in both pressure values and standard deviation.

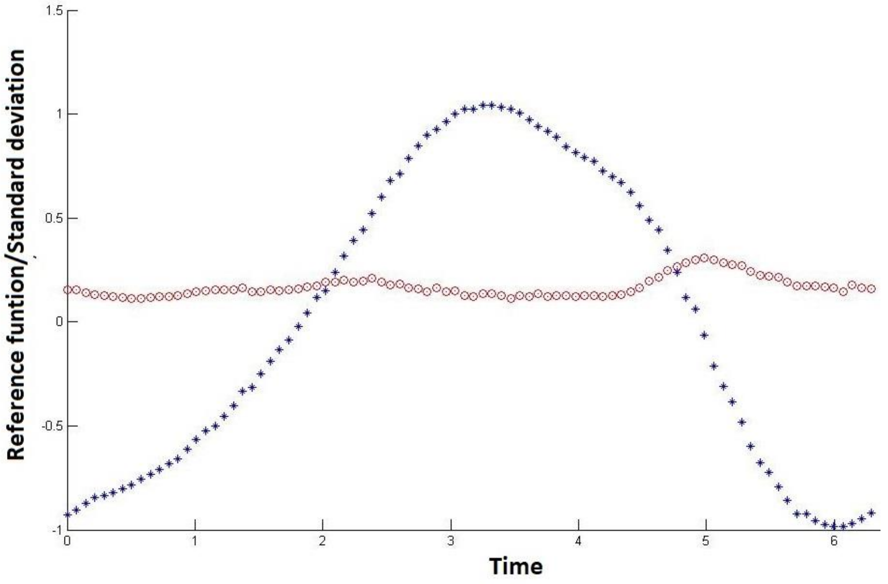

Figure 4-39 Reference function and standard deviation obtained after several iteration

The procedure was performed for all the data acquired in Qn and Qc condition in each slot position. However, dealing with a huge amount of information, we had to pick which ones to carry on in the last analysis. After some inspecting trials performed, the selected reference function chosen are these ones in figure 4.40. Two of them, 0°-3 mm and 0°-6 mm, are representative of the upstream flow, 0°-12 mm is representative of the leading edge, 0°-36 mm is the mid-chord position 0°-60 is the trailing edge and finally 0° -72 is representative of downstream region.

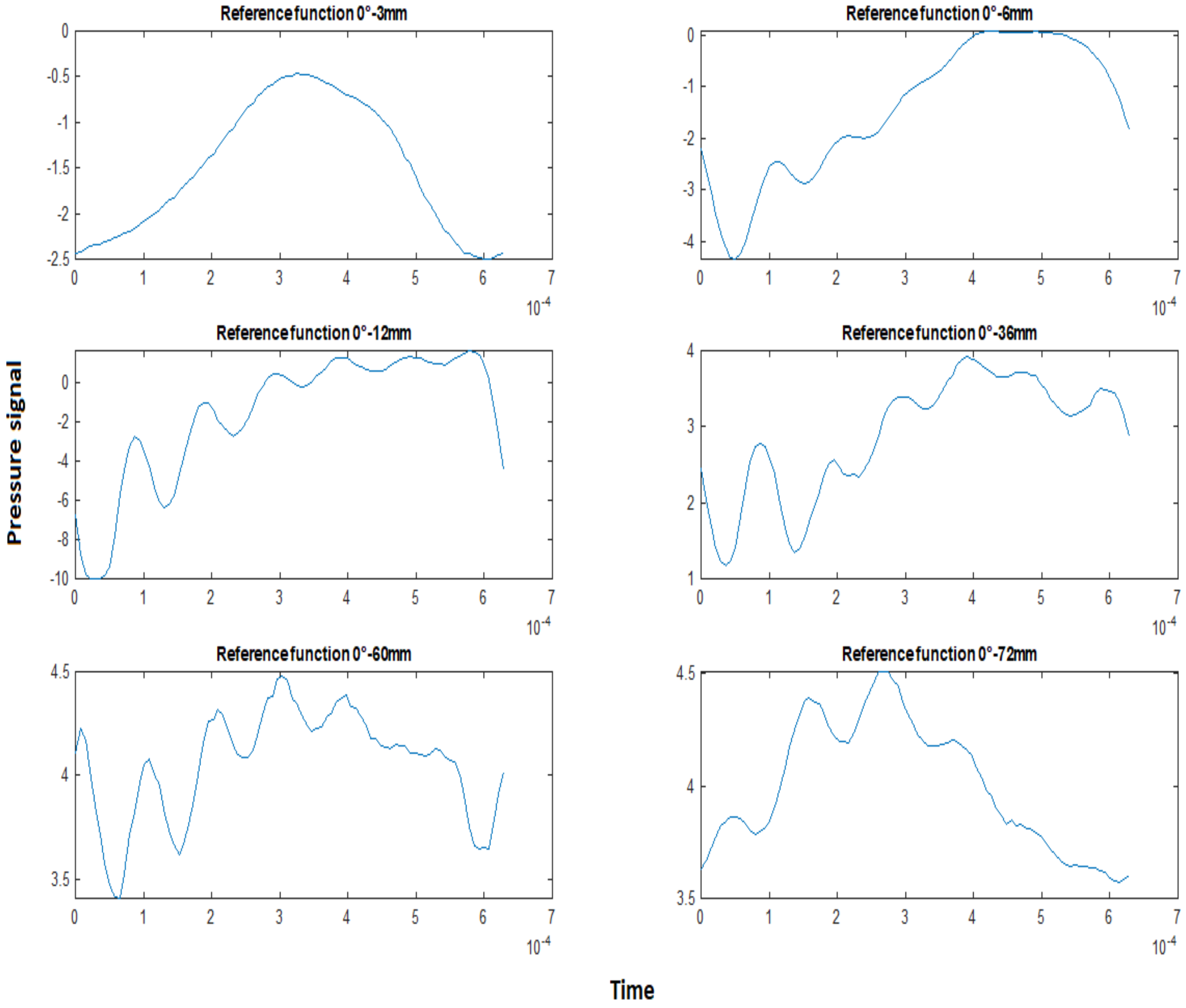

Figure 4-40 Sketches of the reference functions obtained for the described slots

5. IMPLEMENTATION TO STALL TRANSIENT

5.1 INTRODUCTION

The final part of this study is carried out using a series of data collected starting from the characteristic point Qc and decreasing the mass flow rate at constant speed until stall inception. Once obtained what we called reference curve for each slot of the probes, the successive question is how to make use of it. The main idea was to see the trend of the differences between the reference curve, calculated in Qc, and pressure curves generated toward stall. A lot effort had been made matching these two without any noticeable result. The reason for this is attributed to the heavy fluctuation experienced in the compressor even if the stall phenomenon is not yet arisen. Figure 5.1 shows the difference between the reference curve and blade passages before stall for a probe in position 0°-6mm. In the picture is clear that a certain trend in the difference between the two curves but it is also veiled under fluctuation that are of the same order of magnitude of the trend increment.

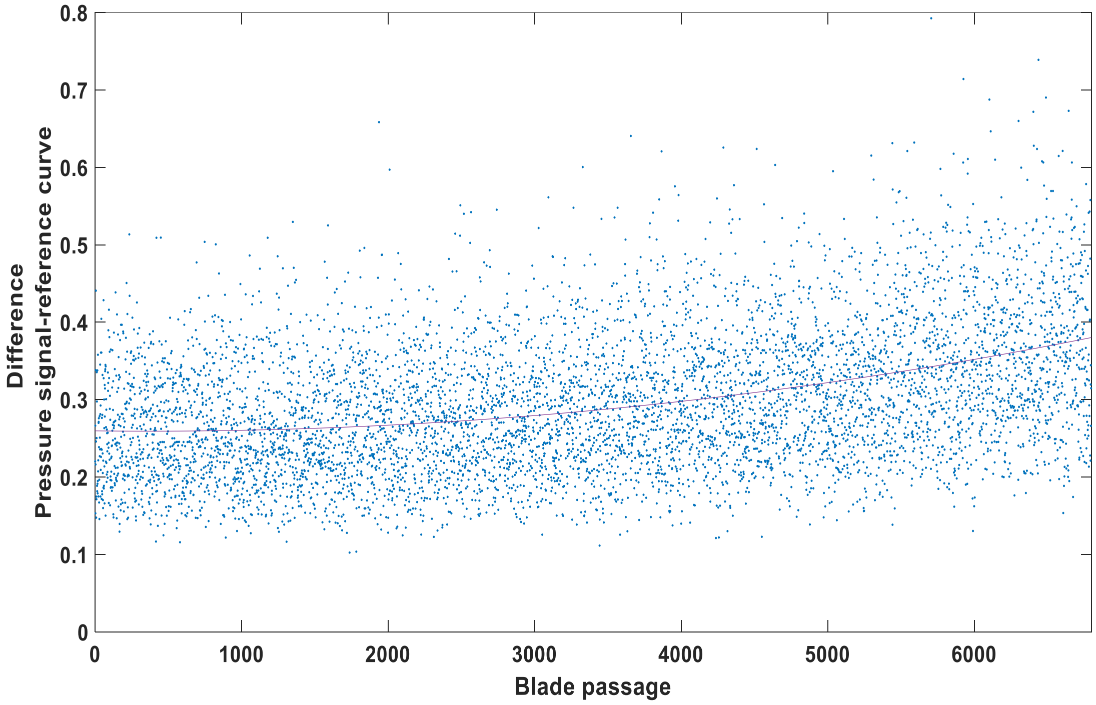

Figure 5-1 Blade passage-reference curve difference trend

Moreover, stall inception, as the literature provides, is something that happens with always the same features, like a spike, but it’s not exactly the same every time; in fact, 100 samples were collected for each probe slot and, even if the starting mass flow rate point and the closing speed of the valve controlling the air flow were always the same, none of them happened in same time lapse, a very few of them have never happened. What we were looking for are parameters that remain constant or have the same feature in every stall inception and are also traceable some time before the phenomenon is experienced. Another area of investigation that was analysed but discarded is the control of periodicities before spikes. Despite having some results in terms of periodic changes in amplitude and frequency we were not able to find an overall rule that could have been helpful in stall forecasting when it is going to happen.

Leaving aside the single blade passage, more desirable results were found investigating a rotor revolution consisting in 30 blade passages. A series of parameters to be investigated were chosen in order to compare different warning options of stall inception.

The parameters are:

- Mean revolution difference: this parameter is just the mean value of a sequence of 30 consecutive blade differences and the reference curve. Figure 5.2 gives an example of calculation before spike for probe 0°-6mm.

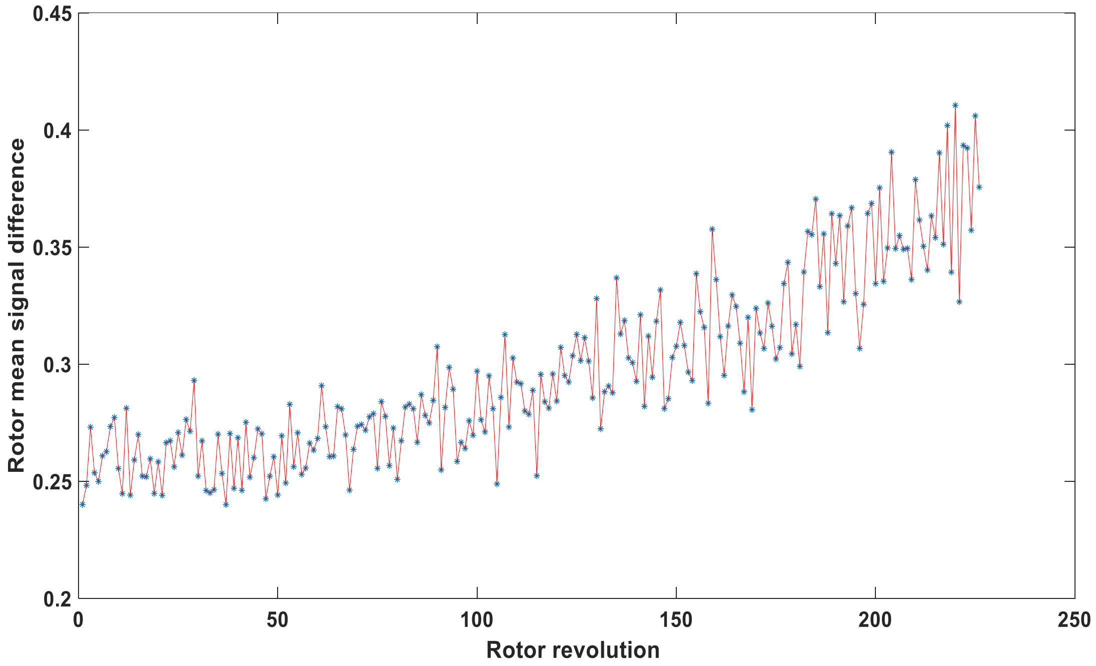

Figure 5-2 Rotor mean signal difference before spike

- Revolution peaks: this parameter indicates how many times in a revolution the difference between the blade passage and the reference function is above a certain threshold. Figure 5.3 gives an example for probe 0°-6mm with a set threshold of the signal of 0.4.

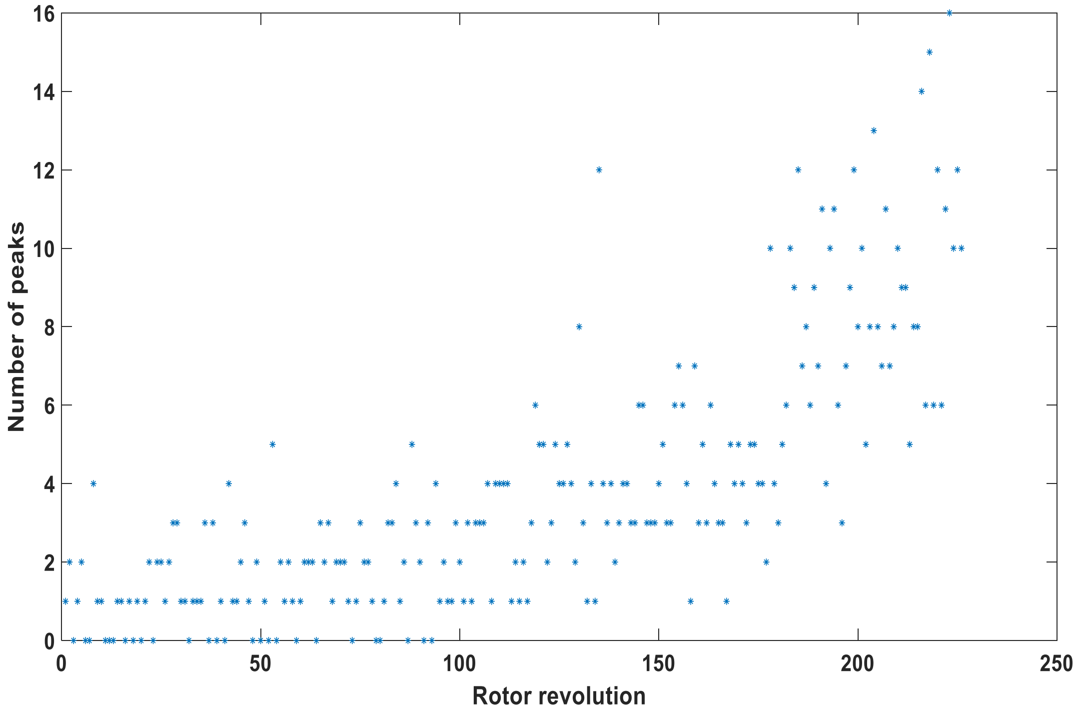

Figure 5-3 Number of peaks in every revolution before spike

- Slope of the mean revolution difference: after setting an arbitrary distance between two revolutions, the slope between these two mean revolution differences is calculated Indicating with N the distance in revolutions, the slope can be calculated as:

$$\alpha = \frac{Mean\ revolution\ difference(i) - Mean\ revolution\ difference(i-N)}{N}$$

Figure 5.4 sketches the slope calculated between two consecutive mean revolution differences with a set distance of 40 revolutions.

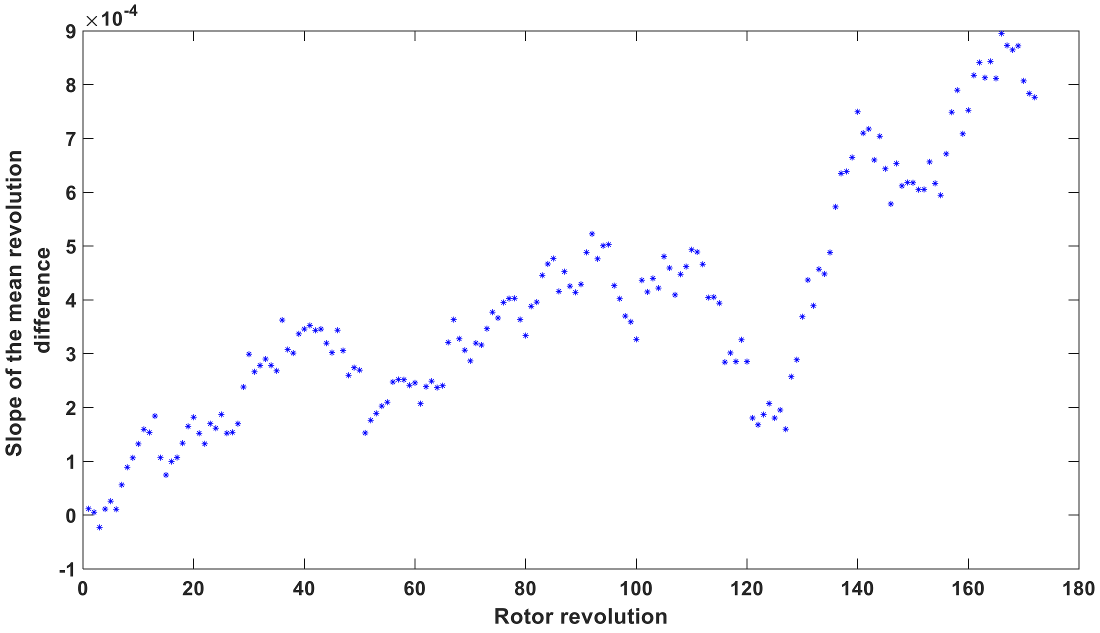

Figure 5-4 Slope of the mean revolution difference before stall

5.2 IMPLEMENTATION AND RESULTS

Without going in detail of how the algorithm works, it’s just important to say that, while the logic behind it is purely theoretical, the implementation is mostly by trials and errors until a good performance is found. Thus, the results that are showed in the next paragraph are not, by any mean, to be intended as an absolute indicator of the universal feasibility to the algorithm. In fact, every constant in the code has to be calibrate for each different case (depending on the machine type and installation position of the probe) in order to find the desirable results. However, it’s not assured that a good result can be found mostly due to the pressure waves shape and fluctuation between a stable point and an operational point beyond the sure line.

Only five of the six reference pressure waves found were finally investigated because probe in position 0°-12mm experienced a problem we didn’t realize during the acquisition and then the machine were not available any longer due to a failure.

The goal of this paragraph is to explain the logic behind the program just for giving an example of how it operates. It’s important to notice that this is not how a real control would act in a working machine but it’s like how the calibration process would be in order to set the right parameters to have the code working in a proper way.

1. SPIKE TRACKER

   In order to give computation limits, spike point has to be found. The tracker works on a smoothed version of the collected pressure points and intercepts the first value above all the peaks of the pressure waves but below the pressure values reached in the rotating stall regime as showed in Figure 5.2.1.

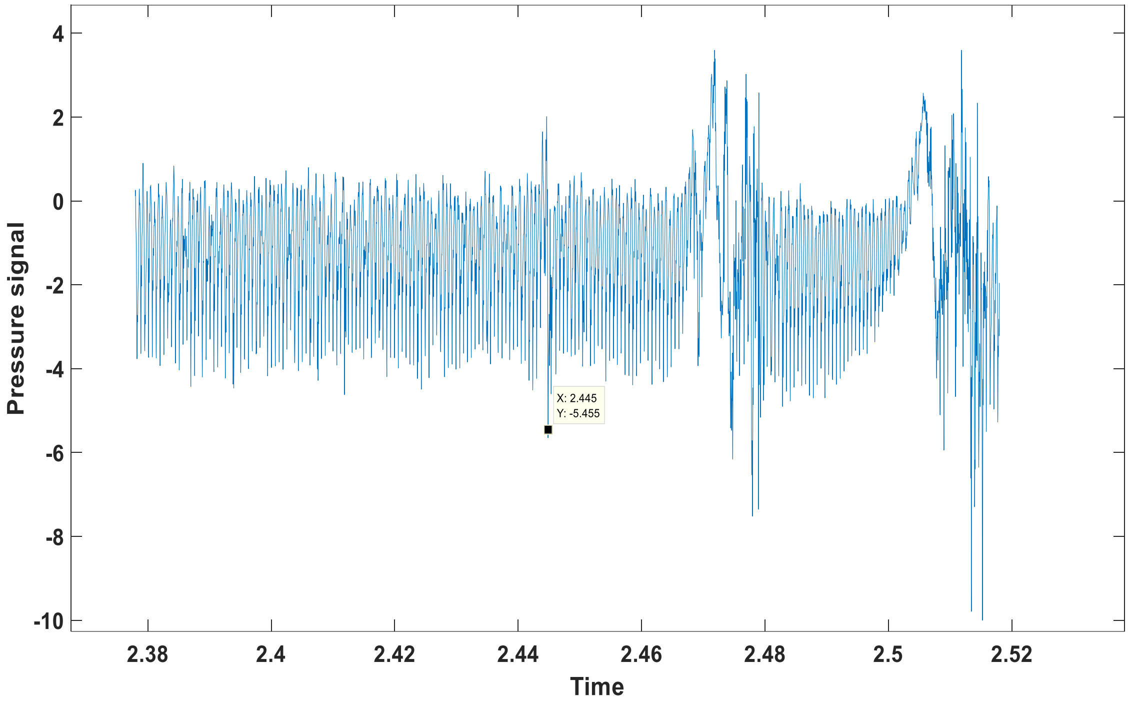

Figure 5-5 Spike point intercepted by a minima peak finder set at -5

2. PEAKS TRACKER

   Like the previous passage, the tracker intercepts all maxima above a certain threshold before a certain limit calculated in the first step. It's important to highlight that the tracker does not find all the point below a set threshold but only the minima values. Figure 5.6 shows an example of points found. In this case, where the shape is clearly distinct it's easy to find the right amount of position that are going to be used in the next step. However, not every pressure profile is like the one in Figure 5.6: it's very common to find waves with more than a minimum in a blade passage due to the natural shape of the pressure curve or high fluctuations especially in the clearance between two blades and approaching stall. To maintain a sturdy and reliable algorithm, an additional passage is required.

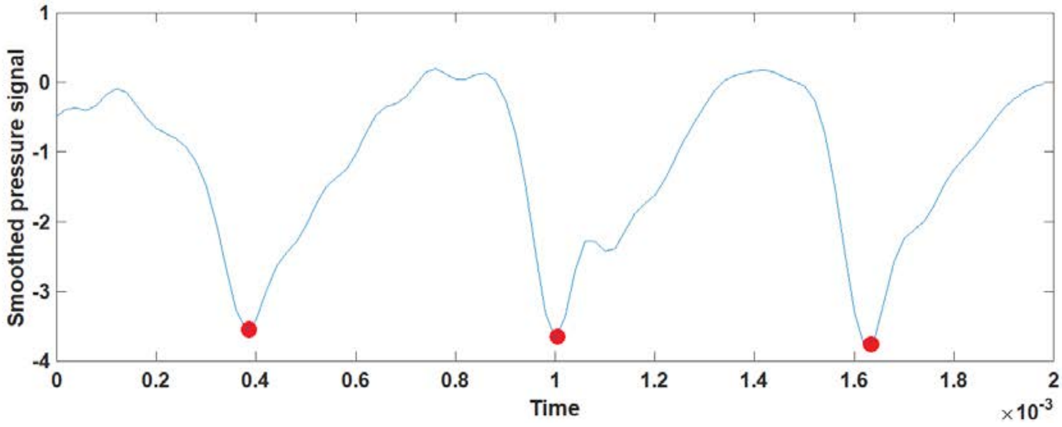

Figure 5-6 Minima points found by the tracker

The first passage is to convolve, as done in the chapter before, all points around the first minimum that all together form a blade passage signal (around 31 points: 50000 Hz * $6.21*10^{-4}$ = 31.05 points) with the reference curve. Once the maximum of the convolution is found and the time values of the reference curve is reassigned to adjust itself to the pressure signal as sketched in Figure 5.7, the code can skip to the next step.

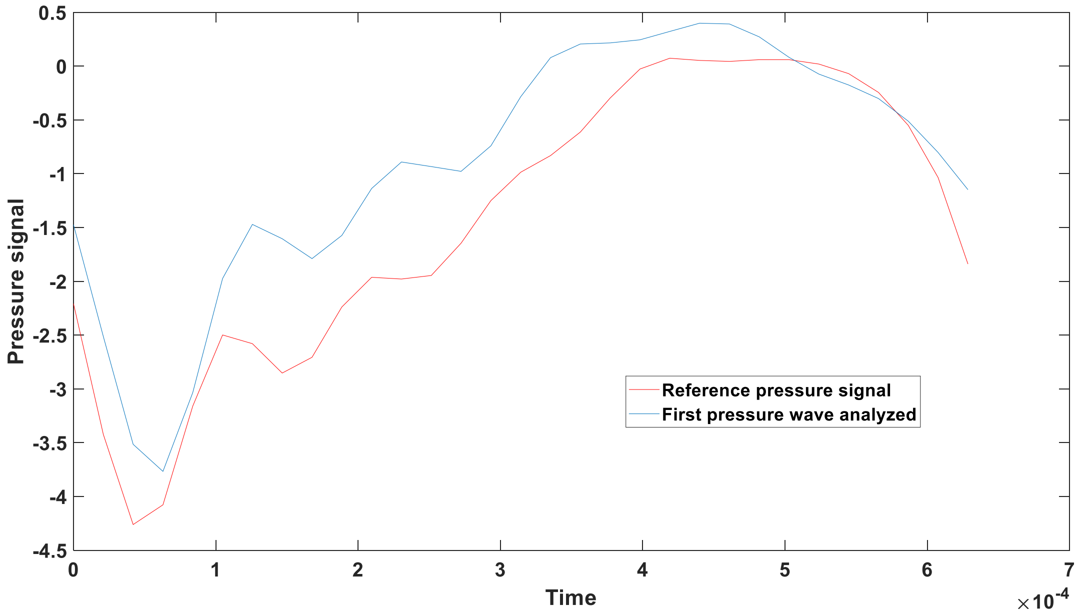

Figure 5-7 Convolution and adjustment between reference curve and pressure signa

3. DIFFERENCE CALCULATION

Before performing the difference, a further operation is required. In order to avoid more than a minimum value within a blade passage time lapse, a check on the position of the following minimum is required: if its location is found before 29-30 points the position of the previous one, then it is discarded. Finally, the code jumps from a minima position to another performing the difference between the reference curve and the current pressure signal obtaining something similar to Figure 5.1.

4. INDICATORS CALCULATION AND RESULTS

After all the differences between the blade passages and the reference curve are done the results can be analysed adopting the 3 meaningful parameters that have showed to be more useful in the stall forecasting:

- Mean rotation difference is a parameter that quantifies the slowly overall change in the pressure passage from the critical condition. It is the slowest among the 3 parameters selected but its changes can be appreciated early on and it is very reliable. Figure 5.2.
- Revolution Peak is a parameter that quantifies the fluctuation change every revolution. It is more responsive in approaching stall but it also has a plateau for several revolution (100-150) and it starts detecting stall with some delay. Figure 5.3
- Slope of the mean revolution difference is in the middle of the two above. It needs some time to build up due to how it is constructed (some revolutions are needed for the slope calculation) but it starts ramping pretty early. Figure 5.4

The following values are just an example of how the method performs. 100 samples are examined for each slot seen before and a measure of the revolution before stall and the standard deviation is performed. Here it is an example for slot 0°-3mm

	MEAN ROTATION DIFFERENCE 0°-3mm	
Threshold	Revolution before stall	Standard deviation
0.25	261.3	11
0.27	223.3	10.1
0.30	201	9.3
0.33	172.7	9.3
0.35	132.2	7.4

Table 5-1 Calculation results for mean rotation difference at slot 0°-3mm

	REVOLUTION PEAK (6peaks) 0°-3mm	
Threshold	Revolution before stall	Standard deviation
0.3	262.7	11.35
0.33	214	9.95
0.35	183.5	9.16
0.4	161.8	8.3
0.42	138.7	7.9

Table 5-2 Calculation results for revolution peak at slot 0°-3mm

	PRESSURE DIFFERENCE SLOPE 0°-3mm	
Threshold	Revolution before stall	Standard deviation
30°	243.6	13.5
33°	238.4	12.7
35°	2.18.6	10.2
37°	217.4	9.8
40°	2.13.1	9.7

Table 5-1 Table 5-2 Calculation results for pressure difference slope at slot 0°-3mm

It can be noticed that the results are really good for this particular case and the method is very handy: 200 revolution are approximately 4 seconds which is the time that the control has to collect data, perform calculation and operate the active control.

However, the description of the 3 parameters is just theoretical. All relies on how the parameters are set, hence, it is always possible to detect stall inception using any one of those warnings or a mix of them. Once the tests are performed and the variables have the desired assigned value, the program can be used in an active control that matches in every moment the pressure signal from the compressor with the reference curve calculated in the maintenance phase.

6. CONCLUSION

The thesis presents an algorithm able to forecast rotating stall inception in almost every condition when the threshold variables are set correctly. This is not an easy task considering how much variable and unpredictable the phenomenon is. Although the reliability and sturdiness of the method is basically all demanded to the human sensibility and experience. Moreover, once set to work, the method requires a periodic check in order to verify changes in the compressor activity, due to aging or other reasons. This shouldn't be a problem considering that if an operator has the instruments to verify and calculated rotating stall inception in functioning condition, he or she has also the instrument to verify and re-set the algorithm.

Moreover, the method is able to operate with a rotor rotating at different speeds with the only caveat of having all the needed reference functions previously uploaded into the controlling system. Another significant pro of the method is its cheapness. Ideally the only equipment required is one pressure probe, maybe two for redundance, and a not so high performing hardware acquiring and elaborating data. Probes are also going to be installed into the case which enhance the safety compared to other positions along the blade height that require a sort of attachment that is very unlike to be durable as time goes by.

In order to have a better insight of how the method performs in every condition it has to be tested on other machines and clearly on compressor experiencing true pressure cycle in operating condition. This could lead to a failure of the method depending on the application and fluctuation of the air flow and possible other noises which the pressure probes are affected by.

Finally, this remains just a first attempt to build the detecting part of a more complex active control for compressors that has to be followed, for example, by some air jets that are able to re-establish stable conditions for a while and push away the rotating stall vortex as the literature provides.

7. BIBLIOGRAPHY

Arnone, A. [. (1999). Numerical Prediction of Wake-Induced Transition in a Low Pressure Turbine. *14th ISABE.* Florence.

Binder, A, Schröder, T, and Hourmouziadis, J. (1989). Turbulence measurements in a multistage low-pressure turbine. *ASME vol. 111* , p. 153-161.

Callot, S. (2002). *Analyse de mécanismes maroscopiques produits par les interactions rotor/stator dans les turbomachines.* PhD Thesis, Ecole Centrale de Lyon, Laboratoire de Mécanique des Fluides et d'Acoustique, Lyon.

Camp T., D. I. (1998). A Study of Spike and Modal Stall Phenomena in a Low Speed Axial Compressor. *ASME J. Turbomachinery* , 393-401.

Day I. (1993). Stall Inception in Axial Flow Compressors. *ASME J. Turbomachinery* , 1-9.

Day I. (2016). Stall, Surge, and 75 Years of Research. *Journal of Turbomachinery* , Vol 138.

Day I., G. E. (1978). Prediction of Compressor Perfomance in Rotating Stall. *ASME Eng. Gas Turbines Power* , p. 1-12.

Day. I. J., e. C. (1978). The Measurement and Interpretation of Flow within Rotatin Stall Cells ina Axial Compressors. *Journal of Mechanical Engineering Sciences* , Vol. 20.

Deppe A., S. H. (2005). Spike-Type Flow Inception in Axial-Flow Compressors. *6th European Conference on Turbomachinery - Fluid Dynamics and Thermodynamics*, (p. 178-187). Lille, France.

Dixon l., H. A. (2010). *Fluid Mechanics, Thermodynamics of Turbomachinery.* Elsevier.

Dring R.P. [et al.]. (1982). Turbine Rotor-Stator Interactions [Revue]. *Journal of Engineering for Power* , Vol. 104(3). - pp. 729-742.

Eulitz F., E. K. (1996, June 10). Numerical investigation of the clocking effects in a multistage turbine. *ASME* , p. 69-GT-28.

Giles M.B. (1988). Calculation of Unsteady Wake Rotor Interaction. *Journal of Propulsion and Power* .

Gravdahl, J. T. (1999). *Compressor Surge and Rotating Stall.* Springer.

Greitzer E. (1976). Surge and Rotating Stall in Axial compressors - Part I: Theoretical compression System Model. *ASME Eng. Ga. Turbines Power* , p. 190-198.

Greitzer E. (1976). Surge and Rotating Stall in Axial compressors - Part II: Experimental Results and Comparison With Theory. *ASME Eng. Gas Turbines Power* , p. 199-211.

Greitzer E.M. (1985). Flow instabilities in turbomachines. In *Thermodynamics and Fluid Dynamics of Turbomachinery* (p. Vol 2). The Hague.

Hodson P. et al. (2000). *Unsteady flow: it's role in low pressure turbines.*

Hongyan Huang, H. Y. (2004, February). Clocking Effect in a Two-Stage Compressor with Different Inter-Blade-Row. *Journal of Thermal Science* , p. Vol. 13 Pag 8-15.

Inoue M., K. M. (2000). Propagation of Multiple Short-Lenght-Scale Stall Cells in an Axial Compressor Rotor. *ASME J. Turbomachinery* .

Korakianitis T. (1992). On the Prediction of Unsteady Forces on Gas-Turbine Blades. *Journal of turbomachinery* .

Lampart, P. (2006). *Tip leakage flows in turbines.* Polish Academy of Sciences.

McDougall N., C. N. (1990). Stall Inception in Axial Compressors. *ASME J. Turbomachinery* , 723-732.

Moore J G, S. S. (1996). *ASME J. Turbomachinery 118* , 622.

Oliveira G. L. (1999). *Analyse numérique de l'effet du défilement des sillages liés aux interactions rotor-stator en turbomachines - PhD thesys.* Lyon: Ecole Centrale de Lyon.

Peng, W. W. (2007). *Foundamentals of Turbomachinery.*

Pullan G., Y. A. (2015). Origin and Structure of Spike-Type Rotating Stall. *ASME Journal of Turbomachinery* , Vol 137.

Sentker A. et Riess W. (2000). Experimental Investigation of Turbulent Wake-Blade Interaction in Axial. *Internation journal of heat and fluid flow* .

Smith, L H. (1966). Wake Dispersion in Turbomachines. *Journal of Basic Engineering* , 688–690.

Stein A., N. S. (2000). Computational Analysis of Stall and Separation Control in Centrifugal Compressor. *Workshop on Goals and Technologirs for Future Gas Turbine.* Georgia Institute of Technology.

Van de Wall, A G, Kadambi, J R, Adamczyk. (2000). A Transport Model For The Deterministic Stresses Associated with Turbomachinery Blade Row Interactions. *ASME* .

Veglio M. (2015). *Etude expérimentale des écoulements dans un étage de compresseur axial basse vitesse en règime de fonctionnement instable.* Ecole Nationale Supérieure d'Arts et Mètiers.

Vo H. (2001). *Role of Tip Clearance Flow on Axial Compressor Stability.* Massachusetts Institute of Technology, Cambridge, MA: Ph.D. thesis,.

Vo H., T. C. (2008). Criteria for Spike Initiated Rotating Stall. *ASME J. Turbomachinery* , Vol. 130.

Yasunori Sakuma et al. (2014). Numerical analysis of flow in a transonic compressor with a single circumferential casing groove: influence of groove location and depth on flow instability. *ASME J. Turbomachinery 136* , 31017.

Young A., D. I. (2013). Stall Warning by Blade Pressure Signature Analysis. *ASME Journal of Turbomachinery* .

8. RIASSUNTO

La tesi è strutturata in cinque capitoli. Nel primo si dà un inquadramento generale sulla teoria delle macchine a fluido comprimibile per riprendere i parametri che verranno usati in seguito in tutto l'elaborato. Si fa riferimento a come sono strutturati i triangoli di velocità di uno stadio di compressione alla teoria dimensionale. Quest'ultima permette di esprimere le caratteristiche operative di una macchina, a diversi numeri di giri e geometria fissata, tramite l'espressione di alcuni parametri caratteristici.

Nel secondo si fa una carrellata piuttosto rapida dei maggiori maccanismi che generano instabilità, soffermandosi però in modo particolare sulla letteratura più recente sullo stallo rotante e cercando di spiegare il fenomeno nel modo migliore possibile.

Nel terzo capitolo si descrive il banco di lavoro sul quale il compressore soggetto a prova è stato montato, di quali attrezzature è stato dotato al fine di permettere le misure e quali sono gli strumenti di misura usati.

Nel quarto capitolo si spiega come il compressore abbia una velocità nominale di 6330 giri al minuto, diminuita a 3200 per effettuare le misure. Si accenna inoltre a come ritrovare le portate di design e critica nel nuovo caso. Successivamente si fa un elenco dei dati disponibili che sono stati acquisiti: Acquisizione in condizioni di design e critiche mantenute costanti per 60 secondi a 35kHz e acquisizioni che portano la macchina dal punto critico allo stallo rotante, diminuendo la velocità in modo costante, con un tempo di raccolta dati di 10 secondi a 50 kHz. Tutti i dati sono stati raccolti per ogni posizione disponibile del supporto per i sensori di pressione anche se solo quelli di una fila assiale sono stati usati per il lavoro di tesi. Successivamente si è calcolato lo spettro delle frequenze per ogni posizione assiale in condizioni di stabilità. (in realtà si sono calcolati anche per le altre acquisizioni ma, poiché non hanno prodotto risultati, non sono stati presentati). Infine si definiscono i passaggi che portano alla costruzione della "reference curve" che consistono in: uso dell'analisi delle frequenze per il calcolo di una funzione di primo tentativo, interpolazione lineare della stessa e dei dati acquisiti, applicazione del filtro, prodotto di convoluzione atto a assegnare in modo corretto tutti i valori di pressione acquisiti nel tempo in una finestra temporale di un passaggio di pala, iterazione dei passaggi precedentemente espressi al fine di arrivare a una convergenza, divisione dei punti riallocati per fasce temporali con calcolo del valore medio e della deviazione standard.

Nel capitolo cinque si esprimono le difficoltà incontrare nella ricerca di parametri che fossero in grado di monitorare lo stato di avanzamento dell'arrivo dello stallo rotante, di come si sia scelto di fare virtualmente uno zoom out piuttosto che concentrarsi nel fenomeno in dettaglio e di quali passaggi si eseguano per monitorare questi parametri. Questi ultimi sono: differenza tra le onde di pressione di una rivoluzione del rotore e di quelle della curva di riferimento, numero di volte che la differenza tra le curve di pressione in una rivoluzione del rotore e quella della curva di riferimento supera un certo valore di soglia e, infine, pendenza della retta calcolata tra la differenza tra le onde di pressione di una di una rivoluzione del rotore e di quelle della curva di riferimento a una certa distanza di rivoluzioni l'una dall'altra.

I passaggi per il calcolo sono i seguenti: calcolo del momento in cui avviene lo spike nell'acquisizione considerata, calcolo dei picchi che determinano la posizione delle onde di pressione, convoluzione per riallocare i valori temporali di pressione e poter compiere una differenza tra le curve in fase, calcolo dei parametri dopo aver deciso le soglie alla quale si vuole che un ipotetico controllo inizi la procedura di uscita dalle condizioni critiche di avvicinamento dello stallo. Si propone infine un esempio dell'applicazione del metodo, per una certa posizione del sensore di pressione, evidenziando come riesca a prevedere lo stallo fino a 4 secondi prima che avvenga.